2013

Silver Nanoparticles As Drug Delivery Systems

Ammar Tahseen Qureshi
Louisiana State University and Agricultural and Mechanical College

SILVER NANOPARTICLES AS DRUG DELIVERY SYSTEM

A Dissertation

Submitted to the Graduate Faculty of the
Louisiana State University and
Agricultural and Mechanical
College in partial fulfillment of the
requirements for the degree of
Doctor of Philosophy

in

The Donald W. Clayton Graduate Program
in Engineering Science

by
Ammar T Qureshi
B.S., Louisiana State University, 2008
M.S., Louisiana State University, 2010
December 2013

To the People Who Got Me Here

My Amazing Wife,

My Parents, sisters and brother, Uncle and Auntie

Acknowledgments

First, I want to thank Allah for giving me the health, patience and determination to complete this milestone in my life. This important academic accomplishment of my life would not have been possible without the support and guidance of a lot of people. Then, I would really like to thank my major professor, Dr Daniel Hayes for mentoring me for the last five years. I value and cherish his vast experience and expertise in the biotechnology sector. His interest in the next generation clinically relevant biotech products allowed me to work on many great projects over this time period. The experience to work on industry and clinically relevant projects really increased my knowledge base and motivated me to work effectively. I will always be indebt to him for his great insights, knowledge, and inspiration/motivation on every stage of every project and value his belief and confidence in me to complete the projects on time. He allowed me to lead my own projects and mentor/train undergraduates and graduates to establish my management skills. He was always available to discuss and give his valuable advice on any research and career related issues. His weekly planning meetings and efforts to gel the graduate students together really created a friendly atmosphere to work. I learned a lot from him on a daily basis and nothing I say here will do justice to his continuous encouragement, uninterrupted support and great research and life lessons. I would also like to thank Dr William T Monroe for also being a great mentor and I really appreciate his guidance on multiple projects. I value his expertise in cell biology and oligonucleotide chemistry along with his vital inputs in lab meetings to steer the project in the right direction. He was always ready to assist in planning and interpreting experiments. I also want to thank Dr Jeffery Gimble for supplying us with hASCs and his expertise in stem cell biology. He provided me with great insights on stem cells. I also want to thanks Dr Jin-Woo Choi and Dr Steven Hall for allowing me to benefit from their

expertise by providing their input on different aspects of research. I want to thank Dr Terry Bricker for serving on my committee as a dean's representative. Really want to thank Dr Diana Coulon for assisting in planning my *in vivo* experiments and conducting the surgeries. Her surgical expertise and experience with IACUC allowed me to conduct my experiments in a timely manner.

I would also like to thank a number of people in the department and college for their various contributions: all BAE professors for their constant support, Ms Cheryl Crowder and Dr Del Piero Fabio for assisting with preparing and analyzing histology slides respectively, Ms. Marilyn Dietrich for running samples on the flow cytometer, Ms. Ying Xiao and Dr Mathew Brown from the Socolofsky Lab, Dr Rafael Cueto for the TGA analysis, Dr Robert Gambrell for the ICP-OES analysis, Dr Ted Gauthier and Ms Tamra for letting me use the LSU AgCenter Biotechnology Core and the BAE administrative staff, Mrs. Angela Singleton, Mrs. Rhonda Shepard and Mrs. Donna Elisar, who were always helpful and expedient with any requests.

I want to thank my good friends and colleagues, Chad Jarreau, Paige Brown, Alyson Moll, Andrew Doyle, Mark Hoppens, Cong Chen, Lekieth Terrell, Nick Totaro all the other lab mates for all their help and providing a friendly and enjoyable atmosphere in the lab.

I would like to thank my amazing parents for their support, prayers, teaching me good values and enabling me to become a good citizen of this world. They went beyond their means to provide the best of everything. My two amazing and great sisters and a brother always provided a loving and joyful environment. My uncle and aunt here in US provided tremendous support in every aspect and travelled miles to help me do well in everything. I truly enjoy their company and pray to Allah to bless all my family members.

Last but most importantly, I could have never completed this milestone without the support of my wife, Salwa Hashmi. Her support and encouragement is beyond words. I appreciate her efforts to put her life on hold and allowing me to pursue my dreams. Her

unconditional support and love, emotional support, great advices helped me to reach this goal. Her support and prayers have been exemplary and instrumental throughout my life and may Allah bless her for all her efforts.

Table of Contents

List of Tables

List of Figures

List of Abbreviations

SNP	silver nano particles
GNPs	gold nanoparticles
hASCs	human derived adipose stem cells
PLLA	poly (L-lactide)
PCL	Polycaprolactone
LSPR	surface plasmon resonance
LSP	Localized surface plasmons
SEM	scanning electron microscopy
AFM	atomic force microscopy
TEM	transmission electron microscopy
TGA	Thermogravimetric Analysis
ICPOES	Inductively coupled plasma optical emission spectrometry
DLS	Dynamic light scattering
HPC	Hydroxypropyl cellulose
NaOH	sodium hydroxide
PBS	phosphate buffered saline
FBS	Fetal Bovine Serum
EPS	exopolysaccharide
PMMA	poly (methyl methacrylate)
PFA	paraformaldehyde
$NaBH_4$	Sodium tetrahydridoborate
$AgNO_3$	silver nitrate
SFS	sulfoxylate
PVP	polyvinyl-pyrrolidone
SCFs	supercritical fluids
NPE	nitrophenylethyl
miRNA	microRNA
PEG	poly(ethylene)glycol
PC	photocleavable
siRNA	small interfering
MSC	mesenchymal stem cells
DEX	dexamethasone
BMP	bone morphogenic protein
HP	heterotopic ossification
CFU	colony forming unit
ALPL	alkaline phosophatase
OCN	osteocalcin
SM	stromal media
OM	osteogenic media
ELISA	enzyme-linked immunosorbent assay
CSD	critical size defects

Abstract

The goal of this project is to study the potential applications of silver nanoparticles (SNPs) in the medical device and pharmaceutical industries. Bone cements have been used in the orthopedic surgeries for many years to anchor prosthetics while filling up the spaces between the prostheses and bone. Antibiotics are an active component of bone cements but the increasing bacterial resistance to these antibiotics and difficulty of shaping and molding the bone cements increases the need for new antimicrobial biomaterials.

Adult stem cell based regenerative therapies have been one of the most widely researched areas of tissue engineering. This is due to the recent success of *in vitro* differentiation of stem cells and a high demand to replace damaged organs and tissues from autologous and allogenic source using regenerative methods. In bone regeneration, growth fact based surgeries have lead to the calcification bones outside the surgical site. Here, we test a SNP based osteogenic drug delivery system, both *in vitro* and *in vivo,* that will provide clinicians and health care providers control of the activation stem cell differentiation leading to the formation of bone.

We will evaluate the *in vitro* osteogenic differentiation of human adipose stem cells with light mediated miR-148b-Nanoparticle conjugates. We will functionalize SNPs with osteogenic miR-14b with a UV sensitive photocleavble group and a TAMRA 563 molecule. The SNP-miR-148b conjugates will be added to hASCs and activated with UV radiation that will release the miR-148 from the conjugate. The released miRNA will differentiation stem cells into osteoblast. The upregulation of early and late stage osteogenic differentiation markers like *ALPL*, *OCN* and Runx2 will be analyzed by qRT-PCR and histological stains (ALPL stain and Alizarin Red).

Also, we will evaluate the healing of critical size mouse calvarial defects with light activated miR-148b-Nanoparticle conjugates. After testing the *in vitro* differentiation of hASCs,

we will evaluate the healing of calvarial size defects with SNP-miR-148b. A 4 mm critical size defect (non-healing) will be drilled on the skull of mice and filled with non-osteogenic Polycaprolactone (PCL) scaffolds. Prior to implantation, the scaffolds will be seeded with hASCs, transfected with SNP-miR-148b conjugates and radiated with UV. The healing of the defect will be analyzed with micro-CT and histological staining after 4 and 12 weeks post implantation.

Chapter 1. Background and Introduction to Drug Delivery Systems

1.1 Noble Metal Nanoparticles: Properties & Applications

The use of nanostructures, notably colloidal nanoparticles, in molecular diagnostics and drug delivery has emerged and increased significantly within the last decade[1]. Nanostructures are amenable to molecular detection, intracellular diagnostics and therapeutic applications due to their sub-microscopic dimensions (<1 um) and the often unique properties which emerge at these dimensions, and which differ from those of the bulk materials. Due to corresponding size-scales, nanostructures easily interface with biological molecules, such as nucleic acids and proteins[1]. Among the nanostructures which are increasingly being used as biological sensors and delivery vehicles for therapeutic agents, nanoparticles are of particular interest. Beneficial characteristics of metallic nanoparticles include tunable size, shape, and functionality attributes; relative ease of fabrication via 'wet chemistry' techniques[2]; large surface area-to-volume ratio; simple surface functionalization (via sulfur-metal linkages on noble metal nanoparticles) [3, 4], and enhanced stability of attached macromolecules such as nucleic acids[4, 5].

Metal nanoparticles, typically in the range of 1-100nm in diameter, are attractive due to their unique electronic and photonic properties [2, 6, 7]. Noble metal (Au, Ag, Pt, and Cu) nanoparticles have accrued interest owing to a phenomenon unique to these nanomaterials, known as localized surface plasmon resonance (LSPR). LSPR occurs when a small spherical metal particle is subjected to an oscillating electric field, which causes the conduction electrons at the metal surface to oscillate collectively in response[7]. The local field enhancements attributed to surface plasmons have paved the way for many surface-enhanced spectroscopy techniques, including surface-enhanced absorption, fluorescence, photochemistry, and Raman scattering (SERS)[8]. These techniques have applications in chemistry, biology, and medicine.

Gold (Au) and silver (Ag) nanoparticles have been used extensively as biological sensors which take advantage of plasmon resonance to enhance detection of specific targets. Noble metal nanoparticle-based sensors benefit from the extreme sensitivity of LSPR spectra to environmental changes[9]. Application of metal nanoparticles is not limited to molecular detection: recently, gold nanoparticles (GNPs), and to a lesser extent silver nanoparticles (SNPs), have been harnessed as delivery vehicles for therapeutic agents, including antisense oligonucleotides[10-12] and other small molecules[4, 13, 14]. Small metal nanoparticles offer many advantages as drug carriers, including high-density surface ligand attachment, transmembrane delivery without harsh transfection agents[10], protection of the attached therapeutic from degradation[5, 11, 15], and potential for improved timed/controlled intracellular release[15]. The photophysical properties of noble metal nanoparticles[16] may potentially bring these materials to the forefront of drug delivery, enabling targeted delivery, spatiotemporally controlled (photo-)release, and delivery confirmation via imaging.

1.1.1 Localized Surface Plasmon Resonance (LSPR)

Localized surface plasmons (LSPs) are excitations of the conduction-band electrons of sub-wavelength conductive nanoparticles coupled to an incident electromagnetic field (i.e. light)[17]. The noble metals in bulk form have overlapping conduction and valence electron bands which do not allow electrons to move relatively freely based on their energy state. [16]
The metal nanoparticles have number of electrons large enough to be characterized by properties differing from those of single atoms, yet too few electrons to reflect the properties of the bulk metal which have close lying (not overlapping) conduction and valence bands (Figure 1.1). Surface plasmons are based mostly upon the oscillations of free electrons within the conduction band that occupy energy states immediately above the Fermi level[16, 18], where the Fermi level

is the outer boundary of electron energy states at absolute zero temperature. Electrons which exist in energy sates above the Fermi level are available for conduction. The optical properties of noble metal nanoparticles are mostly influenced by the electron oscillations, however, the movement of bound electrons can also contribute to the plasmon spectra of these resonant particles[7]. Localized surface plasmon resonance (LSPR) occurs when the charge-density oscillations of the conduction electrons on the surface of metal nanoparticles [6] attain resonance conditions. Resonance modes arise due to the fact that the curved surface of the nanoparticle exerts an effective restoring force on the oscillating electrons[17]. Under resonance conditions, the nanoparticle acts as an electric dipole, resonantly absorbing and scattering electromagnetic fields[17]. In 1908 Mie applied Maxwell's equations to sub-wavelength conductive spheres (Mie Theory[18]) in order to describe the optical properties of metallic nanoparticles. Mie theory describes and quantifies the extinction spectra (the combination of absorption and scattering) of spherical particles of arbitrary size in various dielectric media[7]. Since the advent of Mie theory, other models have been developed to further and more precisely describe the electronic properties of metal nanoparticles, especially non-spherical particles[19]. However, Mie theory remains an important model for describing the size-dependent optical properties of spherical particles in solution.

Localized surface plasmons (LSPs) have a strong affect on absorption and scattering of light and this attribute contributes to bright colors observed in solutions of colloidal noble-metal nanoparticles. The plasmon resonant absorption spectra of Gold (Au) and silver (Ag) nanoparticles lie within the visible region[16], AuNP and AgNP are characterized by a wine-red color, with a plasmon band centered around 520nm[20] and by a yellow/green color, with a plasmon band around 400-420nm dependent on particle size[21] respectively. Additionally, this

plasmon frequency of the NP also depend on particle size, shape, surface state, interparticle distance, and the surrounding dielectric environment[6] and is used to determine the hybridization-induced coupling of DNA-functionalized gold and silver particles[9, 22, 23].

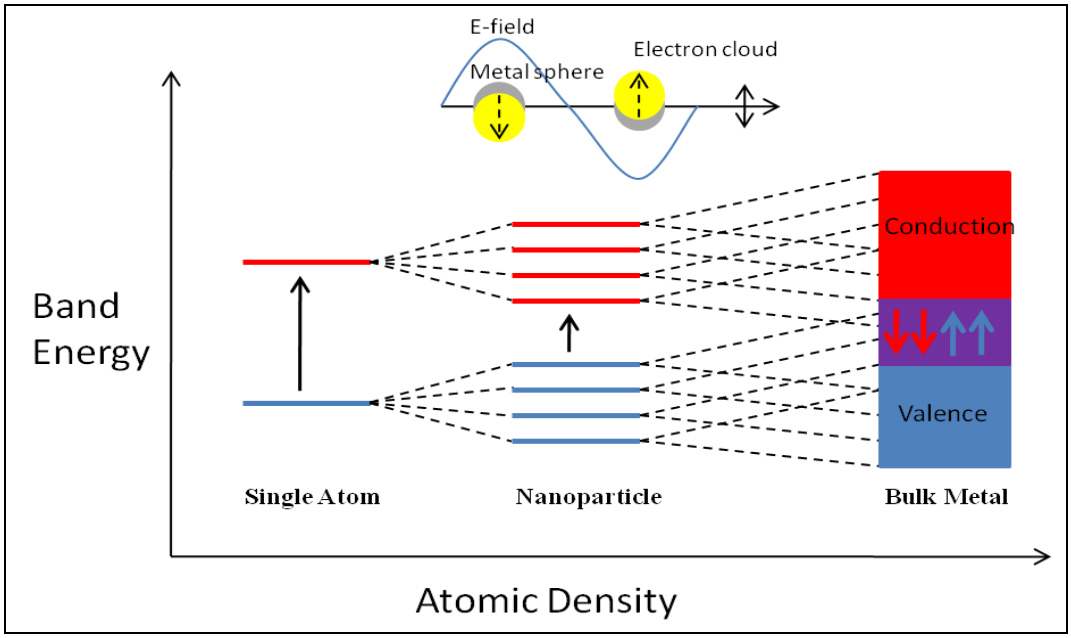

Figure 1.1 – Overlap of conduction and valence electron bands for metals: single atom, nanoparticles, and bulk metals.

The plasmon resonance frequency describes the location at which absorption and scattering (both components of extinction) of light by metal nanoparticles are at a peak value based upon maximum amplitude of electron oscillations and interactions. According to Mie Theory, the extinction cross-section (C_{ext}) of metal nanoparticles is comprised of both absorption (C_A) and scattering (C_S) components. Also the surface plasmon resonance frequency is largely dependent on particle size, and larger particles, dominated by multipole absorption and scattering, typically exhibit red-shifted (longer wavelength) extinction spectra[24]. For small metal particles ($\lambda >> 2R$ where R is the particle radius), the extinction cross-section is dominated by dipole oscillations at the particle surface[24, 25] while for larger particles (2R comparable to incident wavelength λ) the dipole oscillation mode is joined by higher multipole modes. For

small nanoparticles, the absorption part of extinction overtakes the scattering based on the nonradiative processes of plasmon decay[26] and as the nanoparticles increase in size, the scattering component contributes higher than absorption. As a result, the extinction spectra of metal nanoparticles, their absorption and scattering properties, can be tailored via control over particle size and shape.

The strong optical properties of silver nanoparicles can be appreciated with direct comparison of its extinction coefficient. The extinction cross section of a 60nm silver colloid has been reported as $1.4x10^{-10}$ cm^2 which is considerably higher than the cross-section of fluorescein which has a value of ~$2.0x10^{-15}$ cm^2[27]. These strong optical properties of metal nanoparticles are been increasing used advantageously in light scattering and surface-enhanced spectroscopy applications.

1.1.2 Optical Properties of Silver Nanoparticles

Gold (Au) and silver (Ag) nanoparticles in the diameter range of ~2-100nm exhibit SPR spectra in the visible region, which are tunable and dependent on particle shape, size, environment, and interparticle distance. While gold nanoparticles have been used extensively in many of the applications previously discussed, silver nanoparticles have unique properties which make them a desirable alternative particle type in many cases. Silver nanoparticles (SNPs) are the strongest light scatterers of the noble metal particles[21, 28] and it is reported that the light scattering cross section of a silver nanoparticle is ~10 times greater than that of a similarly sized gold nanoparticle[21]. A noted previously, the extinction (light absorption and scattering) band of silver nanoparticles is due to free conduction electron oscillations and bound electron movements also contribute to the optical spectra[21]. Thus enhancement of absorption/emission of light by molecules near the silver particle surface is dependent on particle size and proximity

or overlap of the resonance (SPR) spectra with the absorption/emission bands of the molecular species.

The light absorption and scattering properties for silver nanoparticles of different sizes have been calculated in accordance with Mie Theory[18, 21]. For larger particle sizes (~50-60nm), the scattering efficiency (Q_{sca}) is high (≈5). The silver particles in this size range scatter light at or above the physical metal surface but the scattering efficiency increases even higher to 5.8 for size 70-80nm while maintaining surface plasmon resonance in the UV to visible range. This characteristic is ideal for traditional and red-shifted photocleavable compounds typically used as photo-caging compounds.

The light-scattering and field-enhancement properties of silver nanoparticles have led to an increased interest in their use as sensors, biological labels, and substrates for surface-enhanced absorption, fluorescence, and photochemistry. Enhanced photochemistry has been predicted on silver surfaces, and silver nano-materials comprise the best enhancing substrate found to date[29]. Silver nanoparticles have high extinction coefficients[21, 30] along with low SPR frequencies (near-UV range) which make these particles particularly appropriate for studies of enhanced photochemistry of photoreactive moieties sensitive to UV irradiation.

1.2 Silver Nanoparticle Synthesis

A variety of methods are available for the production of nanoparticles within a specified size distribution[2]. These include reduction of metal ions via chemical capping agents to form metal nanoparticles in solution, vacuum deposition, electron-beam (EB) lithography, laser-ablation (photo- and radio-lytic reduction of metal ions), and electrodeposition (electrochemical deposition of nanoparticles)[6]. Spherical noble-metal nanoparticles for applications such as delineated herein are commonly prepared via ‘wet chemistry’ procedures, where ‘clusters of

metal atoms… are formed in the presence of a surface-capping ligand'[2]. The capping ligand[2], whether a hydrophobic ligand, a charged ligand, or a polymer stabilizing agent, serves to stabilize individual nanoparticles and prevent aggregation via particle-particle repulsion. The wet chemistry synthesis procedures are often simple and practical in the tunable synthesis of spherical particles of sufficiently narrow size distribution.

1.2.1 Reduction Methods

SNP can be produced by reducing agents such Sodium tetrahydridoborate $NaBH_4$[31], $HCHO/NaOH/Na_2CO_3$ [32] , a combined reduction by tri-sodium citrate and formaldehyde sulfoxylate (SFS) [33], tetrakis hydroxymethyl phosphonium chloride, citric acid hydrazine hydrate and solvents like DMF, Ethylene glycol.

In 1979, silver sols were prepared by reduction of silver nitrate ($AgNO_3$) in an excess solution of $NaBH_4$[34]. The solutions of silver salts were mixed rapidly and vigorously in order to aid monodispersity. Pyridine molecules adsorbed on the silver sol particles caused intense Raman scattering. The sols were yellow and displayed a single visible extinction band near 400 nm by Raman spectra. The silver particles were substantially smaller than the wavelength of light and as indicated by transmission electron microscopy, the size of the particle diameter was roughly in the range 1-50 nm [31]. The sols were stable and there was no precipitation or change in color on standing for several weeks.

Formaldehyde can also be used as a reducing agent for preparing nanoscale silver particles. In this synthesis, silver nitrate solution is used as the source of ion. The surfactant polyvinyl-pyrrolidone (PVP), a protective agent, is then added to $AgNO_3$ and the metal is reduced using a formaldehyde solution. To increase the rate of the reaction, pH is increased by the addition of an alkaline solution consisting of NaOH and/or Na_2CO_3 which results in a faster

reduction. This synthesis produces well-dispersed spherical shaped crystalline silver particle with 7–20 nm size [32].

The stoichiometric reaction of this process can be summarized as follows:

$$2Ag^{+} + HCHO + 3OH^{-} \longrightarrow 2Ag + HCOO^{-} + 2H_2O \quad (1)$$

$$2Ag^{+} + HCHO + OH^{-} \longrightarrow Ag + HCOOH + 1/2H_2 \quad (2)$$

Direct large-scale synthesis of SNP is conducted by various reduction chemical methods but using mild reducing agent, such as formaldehyde SFS provides good particle morphology and results in fine silver powder [33].

In this method for the synthesis of SNP, an aqueous solution of tri-sodium citrate was added to an aqueous solution of silver nitrate. The drop-wise addition of aqueous sodium formaldehyde sulphoxylate and continuous stirring at room temperature formed a dark gray precipitate, which can be filtered off, washed with methanol and dried. Scanning Electron Microscopy (SEM) images indicate 30-50 nm spherical and agglomerated SNP due to the presence of surfactants/capping agents.

1.2.2 Sol-gel Process

The sol-gel technique is low temperature method for synthesizing organic or inorganic amorphous materials. It is based on hydrolysis and condensation reactions of organometallic compounds in alcohol solutions [35]. Many metal particles including gold [35, 36], copper [37], platinum, palladium [38] and silver [39] have been prepared in glassy matrices by the sol-gel method.

For the creation of stable silver metal nanoparticles, $AgNO_3$ is dissolved in the precursor sol that contains TetraEthoxy OrthoSilane (TEOS) and Methyl- TriEthoxy OrthoSilane (MeTEOS). Soda lime glass slides can be added in the precursor sol and AgCl containing sol gel

glasses are prepared. When these films are heated to 600^0C, stable silver metal nanoparticles are created that are 2-21 nm in size as calculated from X-ray diffraction [34]. This method produces large clusters of SNP of inconsistent size.

1.2.3 Chemical Vapor Synthesis (CVS)

Recently, CVS has become popular tool for producing highly pure, ultrafine and un-agglomerated nano-crystalline powders. Many chemical vapor methods have been developed which take advantage of various conditions to prepare SNP. Some of the various CV methods include sonic-jet corona discharge [40, 41], electrospray-assisted CVD process [42] and supersonic nozzle expansion method [43].

In sonic-jet corona discharger method, sonic-jet corona ionizer is heated by an infrared furnace and an electric field is applied. Charged nanoparticles are deposited on the substrate electrode in the CVD nanoparticle generator by the help of an electric field after ionized molecules are introduced in the furnace.

The electrospray-assisted CVD reactors consist of an electrospray source, a tube-type CVD furnace and an electrostatic sampler. Liquids are supplied into the capillary by a high resolution syringe pump and a high voltage is applied to the capillary through a high DC voltage source. Electric current carried by electrospray and the stability of the spray is monitored visually, in this process changes in the voltage could result in multiple jets of the liquid. NPs were produced by the thermal decomposition of the precursor vapors in the reactor.

Recently, supersonic nozzle expansion method (rapid decrease in temperature and density) with corona discharge ions was used for synthesizing SNP. In the particle formation step, the high cooling rate of condensable vapor results in a large supersaturation for the nucleation rate. The nucleation and growth of the SNP occurs after the expansion region in the

supersonic nozzle, where corona discharge ions are applied, as the nuclei for nanoparticles, to impart charge and modulate agglomeration.

Overall, CV methods produce NP from the vapor phase in a well controlled temperature zone of a hot wall reaction tube. These processes typically produce agglomerated NP due to their Brownian coagulation in the CVD reactor. Although latest CVD methods have produced nonagglomerated, smaller sized and charged nanoparticles [43].

1.2.4 Biological Approach

With an increased demand to develop clean, nontoxic and environmentally friendly NP synthesis methods, many researchers have started looking at biological systems for inspirations [44]. There are many examples both in the plant and animal kingdom of unicellular and multicellular organisms that produce inorganic materials either intra- or extracellularly [45, 46]. Some of them include magnetotactic bacteria (synthesize magnetite nanoparticles)[47, 48], diatoms (synthesize siliceous materials) [49, 50], S-layer bacteria (produce gypsum and calcium carbonate layers) [51, 52] and fungus *Verticillium* (synthesize aqueous Ag+ ions) [53].

The biological synthesis of silver-based 200 nm crystals in the periplasmic space of *Pseudomonas stutzeri* AG259 was reported in 1999 [54, 55]. This bacterium strain was originally isolated from silver mine[55]. In this method, the cells are cultured in the presence of high concentrations of silver salts. They are then harvested, fixed, distilled and polymerized. Ultrathin sections are stained and visualized under microscope.

There are many other methods of synthesizing SNP including genetically engineered human L subunit ferritin [56], high pressure spurting[57], plasma spray methods [58], supercritical fluids (SCFs) [59] and etc. Although many of these methods have succeeded in

synthesizing nonagglomerated, pure, small size and stable SNP, there still exists a room for improvement in the design of polymer based SNP synthesis.

1.2.5 Biomass Mediated SNP Synthesis

Our choice of SNP synthesis method is related to the design requirements for chronic indwelling medical device coatings, effective antimicrobials and use as drug delivery vehicles. Based on design requirements we have selected one of the chemical reduction methods using formaldehyde as a reducing agent, in an alkaline NaOH solution to reduce $AgNO_3$. This is a cost-effective and industry applicable reduction that occurs at room temperature. The addition of hydroxypropyl cellulose (HPC), a hydrophilic polymer derived from biomass, acts as a template, [60] stabilizes the particle and provides a mechanism for concentration and purification. HPC is a thermo-responsive compound and flocculates at elevated temperatures which facilitate synthesizing concentrated, highly pure and polymer compatible SNPs with increased permeability [61]. The thermally mediated flocculation and concentration step allows the bulk residual reaction by-products to be removed by serial pelleting, washing and resuspension (Figure 1.2).

1.3 Characterization of Nanoparticles

Many analytical methods have been published to characterize and confirm the presence of nanoparticles in the polymers. These methods outline the chemical composition and physical characteristics of the nanomaterials [62].

1.3.1 Atomic Force Microscopy (AFM)

Initially, AFM was introduced as imaging tool [63] as it provides high resolution, three-dimensional images and helps in detailing surface topography. Recently it has been widely used for the investigation of nanoparticle-doped materials and surface biofouling. It has also been

used to examine nanoparticle deposition on silicon substrates, and the morphology of these nanoparticles was studied [64]. Several publications have also used AFM to confirm the morphology and size distribution of silver nanoparticles [65]. It has several advantages terms of resolution, speed and ease of sample preparation when compared to other when compared to cryo-electron microscopy and X-ray crystallography techniques [66]. For our synthesis AFM has been used to determine the organization, shape and size of SNP.

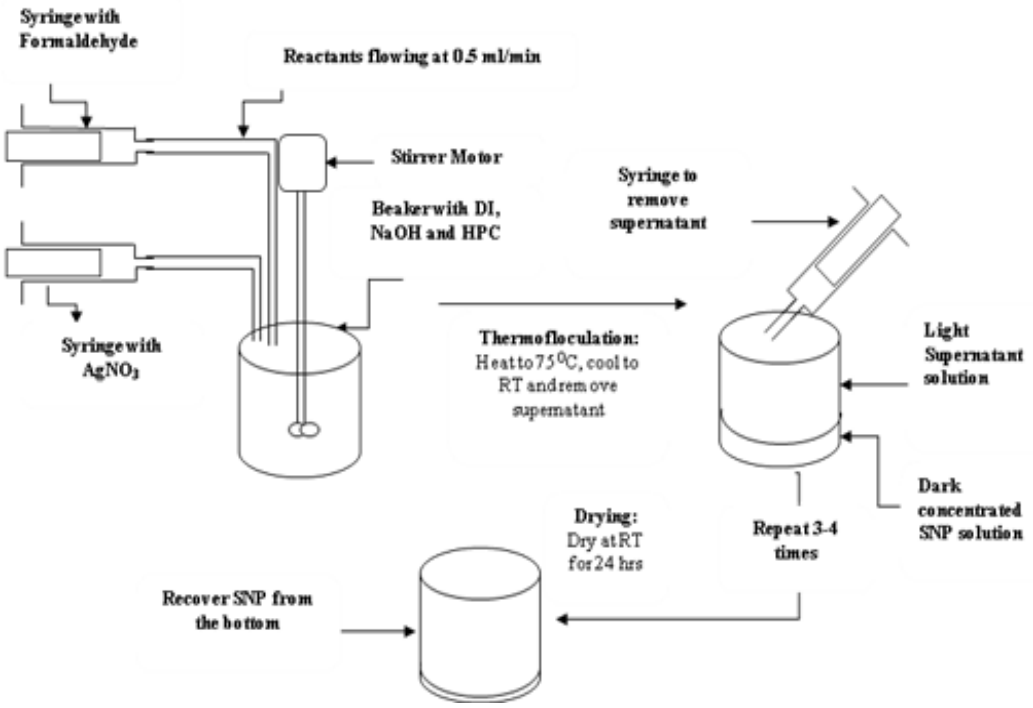

Figure 1.2. Process flow diagram of the biomass mediated reduction and purification process.

1.3.2 Transmission Electron Microscopy (TEM)

TEM is also an analytical tool for determining the morphology and arrangement of nanoparticles comprised materials. Several studies have utilized TEM as a characterization method for different nanoparticles including SNP [67]. SNP will be visualized by TEM [68] and serves as one of our major characterization tools. It enables us to visualize and characterize the morphology and distribution of SNP embedded in the biocompatible polymer-based coatings.

1.3.3 Scanning Electron Microscopy (SEM)

SEM is also an analytical tool that uses a focused beam of high-energy electrons to generate a variety of signals at the surface of solid specimens. Unlike TEM, it allows the surface structure of the sample to be studied at high resolutions, enabling characterization of external morphology (texture), chemical composition, and crystalline structure and orientation of solid materials.

1.3.4 UV-Visible Spectroscopy

UV-visible spectroscopy is a very simple and quick method for characterizing noble metal nanoparticles and is mostly used to confirm the presence of nanoparticles in a liquid. It is not capable of providing detailed information regarding NP size distribution when compared to microscopy based analysis techniques but is a semi-quantitative method for determining the presence and size distribution of NP. UV-Vis can also serve as an indicator of material deterioration and is a qualitative method for indicating the presence of nanoparticles in the polymer.

The breadth of the UV-visible chromatogram peak, obtained from SNP, will indicate the size distribution of SNP but morphology has to be confirmed using different imaging methods. The sample preparation for this method is very simple and will enable us to monitor the effectiveness of the silver nanomaterial and adhesion of SNP to the biocompatible polymer.

1.3.5 Dynamic Light Scattering (DLS)

Dynamic light scattering (DLS) is a technique by which the size distribution of small particles in solution (a colloid) may be quantified from changes in a light field (frequency shifts, polarization changes) due to its interaction with the colloidal system[69]. The information gathered by DLS is related to the light scattering properties of suspended solutes. Dynamic light

scattering may be used to measure the diffusion coefficient for solute molecules/particles, which is related to the radius of a spherical molecule/particle (Stokes Einstein equation):

$$D = \frac{kbT}{6\pi\eta r} \quad (3)$$

where k_b is the Boltzmann constant (in J K^{-1}), D is the diffusion coefficient (in m^2s^{-1}) and T is the temperature in Kelvin, and *r* is the hydrodynamic (or Stokes) radius. The hydrodynamic radius is the apparent radius of a molecule/particle in solution, based on their measured rates of diffusion. Dynamic light scattering analysis of a colloid also provides a measure of the polydispersity (size distribution) of the particle solution.

Dynamic light scattering instruments may also be used to measure zeta potential (electrokinetic potential at the effective shear plane between the moveable and non-moveable part of the double layer[70]) of colloids. Zeta potential of solutes may be determined from the light scattering properties of molecules/particles moving within an applied electric field (electrophoretic light scattering)[70]. Zeta potential is an important indication of colloid stability and biomolecule adhesion onto the particle surfaces. DLS will been performed herein using a Malvern ZetaSizer Nano ZS (Malvern, Worcestershire, UK).

1.3.6 Silver Content Analysis

Determining the silver content in these NP composites is critical to the design of effective antimicrobial scaffolds and drug delivery vehicles. The silver content of scaffolds and the oligonulceotide-SNP targeting drug will assist in tuning the silver concentration to achieve maximum efficacy for scaffolds and optimum/noncytotoxic drug dosage respectively. Some of the methods that comply with our needs and are available to use are Thermogravimetric Analysis (TGA) and Inductively Coupled Plasma-Optical Emission Spectrometer (ICPOES).

1.3.6.1 Thermogravimetric Analysis (TGA)

TGA is commonly used in research and testing to determine the mass of inorganic and organic components in materials by measuring the characteristic of weight change of a material in relation to changes in temperature. Synthesized copper, silver and alumina nanocomposites have been characterized by thermo gravimetric analysis to study the composition of the metal nanoparticles' percentage contained in the polymer/composite [71]. The weight loss curve, after curve smoothing and other operations, can be used to find the point of deflection.

For our SNPs, TGA serves as one of our major characterization tools to determine the percent of silver particles in the scaffolds. Additionally, TGA can also provide information related to the spatial conformation of the silver content and the chemical state of the Ag atoms in the SNP solution [72].

1.3.6.2 Inductively Coupled Plasma Optical Emission Spectrometer (ICPOES)

ICP-OES (Inductively Coupled Plasma-Optical Emission Spectrometer) is one of the most common analytical methods for determining silver content as it has high sensitivity, high precision, and capable of determining range of metals and several non metals at concentrations range from a several percent to ppb levels [73].

In this study, ICPOES analysis is used to monitor the release of SNP particles and ions from the scaffolds after being treated with bacteria. The analysis enables us to quantify the release of SNP from the coatings in a time-based study and plot the release profile of SNP.

1.3.6.3 Oligonucleotide Coverage Quantification

miRNA coverage on functionalized SNP-conjugates was quantified via fluorescence-based measurements of particle-released oligonucleotide samples while the silver content of

HPC-SNP pellet was quantified via inductively coupled plasma optical emission spectrometry (ICP-OES). The particle ratiometric coverage was calculated by:

$$Coverage = \frac{\left(\frac{Mass of Snp by ICP - OES}{\left(\frac{Volume of SNP}{Volume of 1 SNP atom} \right) x MW of Silver} \right) \times NA}{Concetration of miRNA \times NA} \quad (4)$$

1.4 Applications of Silver Nanoparticles:

1.4.1 Silver as an Antimicrobial Agent

Silver is an oligodynamic antimicrobial compound, meaning that exposure to relatively low concentrations of the metal can result in substantial reduction of viable microbial organisms. The ionic form of the compound, Ag^+, has been identified as the primary active agent [74], although some recent research indicates that the nanoscale metal form of the compound may have some unique antimicrobial attributes [75]. Various silver compounds have been used as antimicrobial agents in many healthcare related applications including; pathogen control, prophylaxis and therapeutic treatments. Salts [76-79], zeolites [80-82] and thin film metal coatings [83] have demonstrated some utility as silver ion sources for medical devices, but concerns regarding cost, performance and safety have limited the broader adoption of these delivery vehicles in indwelling device applications.

1.4.1.1 Silver Bearing Salts

Silver bearing salts, specifically, silver nitrate, silver halides and silver sulfadiazine (SSD) have been used as an antimicrobial agent in applications ranging from burn treatment to catheter systems. The exact mechanism of silver and its salts on the microbes is still not known but the possible mechanism of metallic silver, silver ions and silver nanoparticles have been

suggested after looking at the morphological and structural changes in the bacterial cells [84]. The silver interacts with thiol group compounds found in the respiratory enzymes of bacterial cells and binds to the bacterial cell wall and cell membrane, inhibiting the respiration process[85]. In the case of *E. coli*, it acts by inhibiting the uptake of phosphate and releasing phosphate, mannitol, succinate, proline and glutamine from *E. coli* cells [55, 86-89]. The replication of DNA is effectively conducted when the DNA molecules are in relaxed state and loses its replication ability when in condensed form. When the silver ions penetrate inside the bacterial cells, DNA molecule condenses reducing the rate bacterial replication. It has also been reported that heavy metals react with proteins by interacting with the thiol group deactivating proteins[84].

Silver nitrate is a highly water soluble compound that has been used historically in the treatment of burns and as a prophylactic to reduce the transmission of gonorrhea to new born infants during birth[90]. Silver nitrate has not been used extensively as a device delivered antimicrobial, as its high water solubility and low chemical and thermal stability result in relatively short duration of release and challenges in device design and incorporation. Additionally, studies comparing wounds treated with silver based antimicrobials have demonstrated that silver nitrate, compared to other silver forms, significantly retards the re-epithialization and neovascularzation of wound beds [77, 91]. Two halide forms of silver; silver chloride and silver bromide, have been explored as sources of Ag ion for medical device coatings but poor solubility and poor thermal stabili**y,** compared to other ionic forms**,** have limited their broader use in medical device applications [77, 92, 93].

In the 1970's silver sulfadiazine (SSD), a salt derivative of a sulfa drug compound, was characterized and formulated for use in topical creams and ointments to provide a more

efficacious and stable ionic silver delivery option for the treatment of burns and other chronic wounds[94]. More recently, the use of SSD as an active agent has been expanded beyond topical applications including incorporation in devices such as central line catheters and professional wound care dressings and packings [79, 95]. The mechanism of action of SSD is distinct from silver nitrate and silver halide compounds as it acts by disrupting the organism's cell wall and releasing ionic silver through interaction with physiological solutions[94]. The compound's poor solubility in aqueous environments and chemical instability has prevented its broader use in device based delivery systems. While SSD is less cytotoxic than silver nitrate, it is still significantly more toxic than many other commonly used antiseptics and antibiotic compounds, it can prolong wound healing and has been implicated in cases of renal failure [96-98].

1.4.1.2 Silver Zeolites and Glasses

Silver bearing zeolites and glasses, which entrap Ag ion in ceramic crystal or amorphous glass carriers, are the second most common source of Ag ion used in the manufacture of medical devices. Both the zeolites and glass compounds are relatively large, ~2-200μm hydrophilic particles, but each compound has distinctly different mechanisms for silver ion release. Silver zeolites are typically composed of mesoporous aluminosilicate or zirconium phosphate which entrap Ag ion within the nanoscale pores in the crystal structure. Zeolites release Ag^+ into solution through a kinetically favorable ion exchange process with Na^+ or K^+, ions which are ubiquitous in physiological environments. Exposure of high salinity physiological solutions typically results in an initial bolus of Ag ion release and rapid exhaustion of the bioavailable silver ion within the device. The micron scale ceramic carrier is largely inert and not biodegradable, end of life cycle analysis indicates that substantial amounts of silver in zeolites are not bioavailable and remain sequestered within the crystal structure. [82]

Unlike zeolites, silver glass particles are amorphous and are typically composed of unstable, silver doped silica and phosphate compounds [99, 100]. Silver doped glass or "bioglass", as it is often referred, releases silver ion through a surface mediated corrosion process. The relatively large size of the particles and the chemical stability of the silver oxide form in glass tend to reduce the bioavailability of silver ion. Thus requiring high concentrations of bioglass, in the parts-per-thousand range, to achieve reasonable microbial kill rates[100]. The large size and slow corrosion rate of the bioglasses limit their use in bioresorbable thin film coatings. Zeolites and bioglasses share some common features; the silver in both classes of compounds tend to photo-reduce on exposure to light, reducing the amount of bioavailable silver[101]. Also, the hydrophilic nature of the particle surface reduces the solubility of both types of materials in hydrophobic polymer and solvent systems.

1.4.1.3 Other Silver Sources

Bulk metal silver coatings have been used to impart antimicrobial properties to several types of medical devices including; catheters, endotracheal tubes and heart valves. The silver coated heart valve device produced by St. Jude Medical, is notable in that the device's bulk silver coating promoted the onset of endocarditis in tissue immediately in contact with the valve material leading to device rejection[102, 103]. This unexpected cytotoxicity associated with long term exposure to bulk silver coated implants has limited its use to device designed for acute applications.

The recent commercial availability of metallic, nanoparticle silver polymer additives has created a renewed interest in silver based antimicrobials [95, 104, 105]. Advances in synthetic techniques used for particle production have greatly reduced cost, improved yields, and diversified the available particle chemistries and morphologies [44, 106-110]. Shapes such as

rods, spheres, pyramids and other polygons can be combined with a myriad of chemical functionalities to create a wide window of particle solubility and reactivity. This highly flexible nanoscale form of metallic silver potentially addresses many of the limitations of ionic silver delivery systems that have restricted their use as an antimicrobial in the design and manufacture of chronic indwelling device**s.** SNP provides a thermally, chemically and photostable reservoir of metal atoms that are uniquely suited to polymer composite formation while remaining available for conversion to the active ionic compound upon exposure to physiological solutions. SNP show efficient antimicrobial property compared to other salts due to their extremely large surface area, which leads to better contact with microorganisms [84].

Our novel biomass medicated synthesis and concentration/purification method allows for the synthesis of high purity, biocompatible, nanomaterial powders and colloidal solutions with tunable chemical properties. This SNP synthesis method produces metal nanoparticles with a size distribution from 25-75 nm. By careful choice of capping surfactants and bioresorbable/biocompatible stabilizing agents the silver ion release profile and particle dissolution rate can be predictably modified, allowing fine control of the antimicrobial efficacy and particle lifetime in a physiological environment.

1.4.2 Nanoparticle as Drug Delivery Vehicles

Functionalized metal nanoparticles have accrued significant interest as drug delivery vehicles and potential substrates for targeted and controlled release of therapeutic agents *in vivo*. Protein-based and, of interest herein, nucleic acid-based drugs are in need of novel delivery technologies which can enhance delivery, prolong lifetime, enable precise targeting, improve efficacy, and minimize side effects[15]. Nanoparticles provide a promising and exciting solution, bringing to the table improved delivery and stability characteristics, as well as the potential for

external control (thermal, photo-thermal[4], light-activated[111]) over drug release and activity *in vivo*[15]. Various nanoparticle formulations have been used for delivery of biomolecules such as small molecule therapeutics[13, 15, 112, 113], proteins[15, 113], nucleic acids[3, 10-12, 14, 15, 114, 115], antisense oligonucleotides [10, 12], and siRNAs [11, 116, 117].

Nanoparticles have been shown to protect immobilized biomolecules from degradation (notably nucleic acids[5]), thus prolonging their active lifetime[15]. Protection of nanoparticle-immobilized nucleic acids from degradation by nucleases has been partially attributed to the high local salt concentration which accompanies dense nucleic acid packing on the particle surface. High salt concentration is known to deactivate the enzymatic activity of DNase II[118], a principal agent of nucleic acid degradation *in vitro*. Other explanations for the stability of nucleic acids when attached to nanoparticles include steric hindrance of nucleases, protection of a surface-attached 3' oligonucleotide end from 3' exonucleases[119], and possible protective layers of positively-charged serum proteins which absorb to the highly-charged nucleic acid-nanoparticle surface[10].

Biomolecule surface-functionalized nanoparticles not only possess characteristics of enhanced stability, but provide a means to deliver greater amounts of target therapeutic via high density surface coverage, often without requiring additional transfection agents for passage through the cell membrane[10]. Nanoscale delivery vehicles have been shown to enhance cellular uptake via facile endocytosis of small functionalized nanoparticles[113] mediated by scavenger receptors[120], intracellular trafficking of delivered therapeutics, and nuclear access[121], the later being an important process in gene expression based therapies. Beyond the their enhanced cellular uptake and their delivery of high drug concentrations, metallic nanoparticles are also attractive due to the possibility of controlling the release of the bound

therapeutic molecules from the particle surface. The ability to attach ligands via specific interactions to the metal nanoparticle surface offers a high degree of engineering precision[15] with the potential for ligand/receptor targeted delivery[14] and controlled release of the particle payload.

The potential benefits of noble metal nanoparticles (NP) in delivery applications include readily tunable morphology, ease of bulk synthesis, large surface area-to-volume ratios and robust functionalization chemistries[2]. Additionally, metal nanoparticles fulfill the core requirements as drug delivery vehicles by offering high-density surface ligand attachment, facile transmembrane delivery [10], reduced degradation of therapeutic payload nucleic acids [4, 5, 11, 15, 122, 123], and potentially controlled intracellular release [15]. Controlled release mechanisms of drugs from nanomaterial surfaces have included thermal, pH, chemical, and ionic strength stimuli based processes. The optical and photophysical properties of metal nanoparticles further provide unique prospects for photo-controlled release and characterization of delivery and release based on SPR-enhanced imaging signals.

1.4.2.1 Silver Nanoparticles as Drug Delivery Vehicles

Silver has not traditionally been applied in NP-based drug delivery applications, where gold[10-12] and other materials[114] have been popular, likely due to difficultly of SNP synthesis, reduced stability when functionalized according to popular salt-aging techniques, and former concerns about silver toxicity. However, clinical use of SNPs as effective antimicrobial solutions in wound care, as well as recent *in vivo* studies providing positive safety assessments for systemic exposure, have encouraged biomedical research with SNPs. A 2008 animal study revealed minimal induction of secondary markers of liver damage even in the presence of chronic oral SNP doses greater than 300 mg/kg/day for 28 days[124]. Reported safety and lack

of side-effects for SNPs administered at ‘moderate’ doses[125] may lend greater confidence in the suitability of SNPs for *in vivo* solutions studies that seek to lower the threshold of ‘effective’ SNP doses by harnessing their large drug payload capabilities and electromagnetic field amplifying characteristics. Recent improvements in SNP biocompatibility via surface modification, as well as exceptional optical properties [21, 28], have also improved suitability of SNPs for drug delivery.

The unique field enhancement properties of SNPs, where the light scattering cross section of a silver nanoparticle is ~10 times greater than that of a similarly sized gold nanoparticle[21], have led to increased interest in their use as sensors[126, 127], biological labels[21], and substrates for surface-enhanced absorption, fluorescence[128], and photochemistry[16, 129]. Additionally, SNPs offer higher extinction coefficients and blue-shifted plasmon resonant peaks over other metallic nanomaterials[21, 28], making them an appropriate alternative for photo-controlled drug delivery applications and potential surface-enhanced photochemistry of caged compounds such as nitrobenzyl derivatives.

The optical properties and biocompatibility of SNPs are well described in the prior art and importantly they have distinct plasmon-related absorption spectra with maxima at ~420nm [14, 128, 130-132]. This difference is critical to determining the role of plasmons in photoconversion of the nitrophenylethyl (NPE) photocleavable linker incorporated into our microRNA (miRNA) –SNP complexes (abs. max ~365nm). Previous studies have described both thermal and non-thermal components of plasmon mediated catalysis which can increase reaction rates by 2-3 orders of magnitude [133, 134]. The non-thermal component is likely related to intense electrical fields in the oscillating surface plasmon region interacting with ions and molecules thus reducing the activation energy of reaction.[133, 135] Metal enhanced fluorescence has been described

with silver nanostructures, wherein a resonance state or coupled photon is shared between a photoactive molecule and the metal nanomaterial resulting in more efficient photoconversion.[136]

In the case of the miRNA-SNP, these quantum mechanical surface plasmon events could result in significantly lower required photon flux for cleavage and red-shifting the activation spectra, providing better tissue penetration and reduced photo-damage by transiting photons. Our SNP platform for antisense drug delivery and spatiotemporal release takes advantage of silver's unique photophysical properties for fluorescence confirmation of surface functionalization, cell uptake, and activation via nitrophenylethyl (NPE) nucleic acid linker photocleavage.

1.4.2.2 Cytotoxicity Pathways of Silver Nanoparticles

In order for silver nanoparticles to be used in therapeutic delivery applications, the effects of SNPs on cell health must be studied, and shown to have no adverse affects at therapeutically applicable concentrations. Recently, studies on the use of SNPs in therapeutic applications, for example drug delivery, have met with concerns about the toxicity and negative effects of silver nanomaterials.

Concerns of the impact of silver nanoparticles on cell health include decrease of mitochondrial function and induction of apoptosis, the mitochondria being a sensitive target of cytotoxicity of SNPs[137]. While the mechanisms of silver nanoparticle toxicity are not well characterized, they may involve surface binding (depletion) of thiol-containing proteins, including glutathione and key component enzymes of the cell's antioxidant defense mechanism, which leads to increased reactive oxygen species (ROS) generation, oxidative damage[137], and apoptosis, a complex programmed cell death pathway (Figure 1-3).

Particle surface electrostatic interactions with charged biomolecules might also attribute to the toxic properties often observed for 'naked' silver nanoparticles at high concentrations[138]. Recent studies have also shown that primary cells have much higher SNP tolerance than concentrations often used for antimicrobial effectiveness[139]. Mechanism to improve the biocompatibility include functionalizing the metal nanoparticles with poly(ethylene)glycol (PEG) groups, lipids, polymers and small peptides.

The surface modification of silver nanoparticles with thiol-modified biomolecules has been shown to improve silver biocompatibility and intracellular uptake[138]. The phospholipid-protected silver nanoparticles were delivered into 3T3 fibroblast cells and platelet cells with minimal toxic effects.

1.5 Metal Nanoparticle with Biomolecules

Recently the advancements in the field of functionalizing the metal nanoparticles, notable noble metals, with various organic compounds, including proteins, nucleic acids, long-chain hydrocarbons have gained increasing importance in the nanomedicine. These nano-hybrids incorporate the bioactive properties (catalytic functions, recognition and binding properties) of macromolecules with the unique optical and photochemical properties of noble metal nanoparticles[2]. This increasing importance stems from the ease of noble metal nanoparticle functionalization with biomolecules. The functionalizing chemistries can be broadly classified under electrostatic interactions as well as covalent binding [2]. Metal nanoparticles that are synthesized by salt reduction are in most cases stabilized by anionic ligands such as carboxylic acid derivatives[2], which give the metal particles a net negative surface to stabilize the particles and prevent particle-particle interactions (aggregation). This negative charge allows the positively charged ligands/functional groups (positively charged amino acid side chains of

proteins) to interact with the metal surfaces through electrostatic interactions [2]. On the other hand, the metal nanoparticles can also be functionalized with ligands and biomolecules by covalent coupling. Primarily, the binding of thiols to the metal surface (via covalent sulfur-metal bond), is a predominant method of nanoparticle functionalization[2]. Amine and carbonyl functional groups may also interact with the metal surface[140] and serve to tether biomolecules to the nanoparticle surface using standard conjugation chemistries.

1.5.1 Silver Nanoparticles with Nucleic Acids

Nucleic acid-nanoparticle hybrids have been used for a variety of applications, including DNA detection based on LSPR absorbance changes[6, 126], particle assembly based on hybridization[9, 20, 22, 23], DNA intracellular delivery[3, 4, 10, 14, 114], and gene therapy[11, 12]. Nucleic acids are typically immobilized on metal nanoparticles via covalent coupling (thiol end-modified nucleic acids). The nucleotide bases of single-stranded DNA (ssDNA) are also available for binding to the metal surface via amine and carbonyl functional groups[140, 141].

Metal-biomolecule complexes are assembled by single molecule monolayers, or mixed monolayers (assembling a monolayer of one type of biomolecule and backfilling with another), on the nanoparticle surface via functional groups which interact with metal, such as thiols, amines, carbonyls, etc[142]. For thiol linkage of nucleic acids on metal surfaces to overpower other base interactions, techniques must be employed to create an environment where sulfur-metal bonds are favored over other interactions. One of the method include custom-modifying the nucleic acids with thiol functional groups. This can assist in assembling a tightly-packed monolayer of nucleic acid on a nanoparticle surface. The nucleic acids also have reactive functional groups (significantly amines) which can associate with metal surfaces and assist in stabilizing SNP-nucleic acid conjugates in the early stages of functionalization[143]

Typically nanoparticle-nucleic acid conjugates must be slowly adjusted to physiological salt concentrations (≈ 150 mM), conditions which serve to minimize the electrostatic repulsion between individual oligonucleotides ('screening effect')[144] that arises due to the negatively charged state of the phosphate backbone. This screening will enhance surface coverage[9, 143, 145, 146], as well as create an environment at the particle surface most favorable to ligand attachment via thiol bonding vs. amine, carbonyl, or other functional group interactions. Thus the required level of salt (typically NaCl) must be added gradually, and a fine balance must be struck in order to maximize surface coverage as well as colloid stability. Nanoparticle size (curvature)[147], oligonucleotide length and sequence[140], presence of 'linkers' or spacers molecules, presence of low levels of surfactant[146], and final salt concentration have all been found to affect surface coverage and stability of SNP-oligo conjugates.

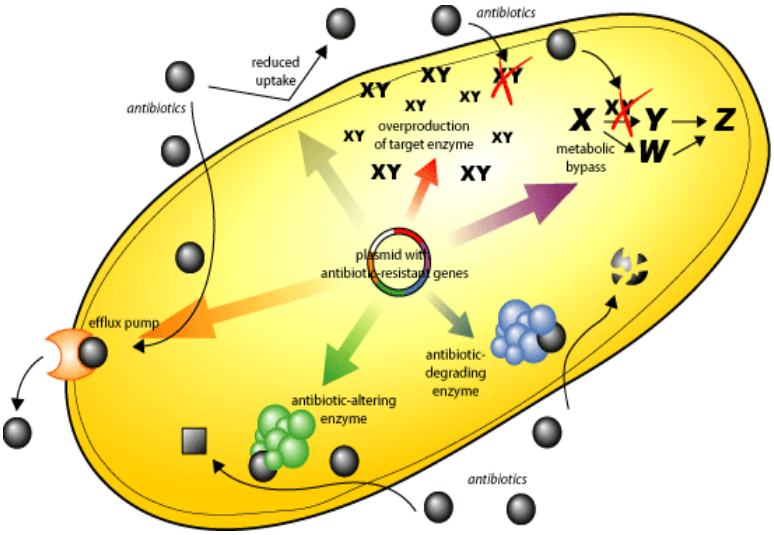

Figure 1.3. Different pathways that silver nanoparticles take to attack the cells.

1.6 Photo-controlled Release

Light-responsive systems are of great interest in the field of drug delivery and gene therapy, owing to the capability of external, spatiotemporal control over the delivery and

activation of therapeutics coupled with such systems. Light-responsive drug delivery systems are triggered by electromagnetic radiation, typically in the UV, visible, and near infrared (NIR) range[148]. These systems are based upon photosensitive compounds which can be incorporated into a drug delivery vehicle, or coupled to the drug itself ('caging' compounds), and may switch to an active or inactive state upon electromagnetic irradiation within a specific frequency range. Caged compounds are powerful tools for spatiotemporal control over drug activity in living systems[149]. Photocleavable groups have been used to cage, or inactivate, various biomolecules, including nucleotides, proteins, and nucleic acids[149-151], for the purpose of controlled, on-site photo-activation. Uncaging via light irradiation allows rapid, spatially and temporally defined release of a biomolecule at intended tissues or even within a specific intracellular compartment[149].

1.6.1 Photocleavage Reaction Scheme

Photolabile ligands have been reviewed [152] giving a wide selection of available compound most for a specific caging application. An ideal caging compound should possess high extinction coefficient and quantum yield properties at wavelengths which are not detrimental to biological systems. The quantum yield ( ) of a photochemical reaction is defined as the efficiency with which absorbed light (incident photons) produces photolysis while the absorptivity of a compound at a particular wavelength of incident light is quantified in the compound's extinction coefficient (ε, units: M^{-1} cm^{-1}).

The most widely used photocleavable compound, 2-nitrobenzyl derivatives[149], has been used in the caging of adenosine 5'-triphosphate (ATP) by Kaplan et al[153], with a reported maximum quantum yield of 0.63. The phosphate esters form of 1-(2-nitrophenyl)ethyl have been used to cage nucleotides[154, 155] with a reported quantum yields of 0.49-0.63. Commercially

available 1-(2-nitrophenyl)ethyl (NPE)-based photocleavable (PC) linker has been used for immobilization onto solid surfaces, purification, and characterization of nucleic acids[156]. This PC linker demonstrates high photocleavage efficiency under UV-irradiation (300-350nm)[157], and has been chosen as the photo-labile group herein for immobilization and release of oligonucleotides from a metal nanoparticle surface.

Upon photo-irradiation, the phosphodiester bond between the photocleavable group and the phosphate is cleaved, resulting in the formation of a 5'-monophosphate on the released moiety (oligonucleotide)[156]. The 1-(2-nitrophenyl)ethyl moiety is converted to a 2-nitrosoacetophenone derivative[154, 156]. The general photochemical reaction scheme of an o-nitrobenzyl compound is shown in Figure 4.

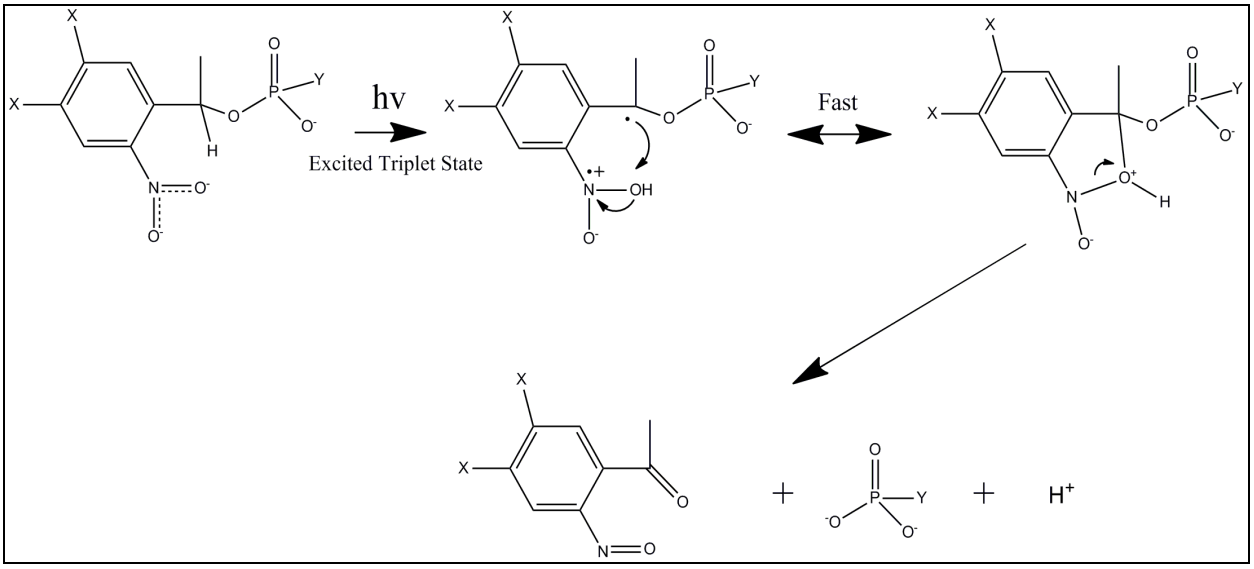

Figure 1.4 - O-Nitrobenzyl photochemistry[152, 158]

1.6.2 Light Sources

Typical light sources for uncaging emit UV radiation to excite photolysis of photocleavable compounds. Flash lamps, lasers, transilluminators, and laser microscopes with UV emissions in the range of 300-360nm are often used for uncaging. Lasers with narrow

excitations lines or broad bandwidth light sources equipped with filters to select for desired UV-range wavelengths are appropriate sources. The electronic properties of SNPs may offer the potential of uncaging at higher wavelengths (visible to IR) due to SPR-enhanced excitation[159], which is of interest due to increased tissue penetration of longer wavelength light, and decreased probability of damage to biological components caused by high frequency (ultraviolet) electromagnetic energy.

1.7 Two Main Antisense Modes of Action

The underlying concept of antisense technology is basic Watson-Crick base pairing[160] between a delivered nucleic-acid and its complementary target. The antisense oligonucleotide (either DNA/RNA or small interfering (siRNA) either affect the transcription or translation pathways through two main methods: 1) enzymatic degradation of target mRNAs via RNase H 2) steric hindrance of translation, transcription, or splicing. The antisense technology results in the inhibition of a protein. The RNase H pathway has been a gold standard in antisense technology, due to the fact that the antisense oligonucleotides involved are left intact and functional following target mRNA degradation, and are thus able to effect the degradation of many target mRNAs[161]. Conversely, the main limitation of this RNAase H antisense pathway was the lifetime of the antisense oligonucleotide. Non-specific side effects of the therapeutic molecule as well as its intracellular localization may also limit the effectiveness of any particular antisense oligonucleotide once delivered to a cellular target.

1.7.1 Antisense Oligonucleotides

Antisense oligonucleotides are short nucleic acids (10-30 base pairs long)[162] which interact with complementary mRNAs to prevent production of a specific protein. This inhibition of protein product production at the transcription or translation level is the hallmark of antisense

technology. This is in sharp contrast to other therapeutic drug that works on preventing the function of protein. Antisense oligonucleotides prevent transcription or translation of substrate nucleic acids in a sequence-specific manner, and are often directed to the 5' initiation sequences or 5' UTRs (untranslated regions) when the mode of action is steric hindrance[119], or almost any available binding site on an mRNA when the mode of action is degradation. It is interesting to note that initiation sequences and UTRs are often available for binding due to the fact that these sites are generally accessible to proteins such as transcription factors and ribosomes[119].

A major problem with phosphodiester antisense oligonucleotides is their susceptibility to degradation in the physiological environment[163]. The half-life of phosphodiester oligos, i.e. the time before half the molecules are inactivated by degradation, is only on the order of minutes when suspended in serum, or blood plasma. Serum contains 3'→5' exonuclease proteins, which are the primary agents of degradation for traditional, i.e. phosphodiester, antisense oligos[164]. Endonuclease enzymes are also responsible, to a somewhat lesser extent, for oligonucleotide degradation in the intracellular environment. Therefore, these phosphodiester oligonucleotides have very limited use in antisense therapy in natural form without chemically modification listed, in Figure 1-5[160], to inhibit degradation in a physiological environments.

Chemically modified oligonucleotides are now available with longer half-lives in serum and resist nuclease degradation within the intracellular development. Phosphorothioate oligos, which have a modified phosphate backbone wherein a sulfur replaces the non-bridging oxygen, have a half-life in serum on the order of hours[165]. Phosphorothioate oligos, which are among the most extensively studied and practically applied antisense oligonucleotides[166], prevent mRNA translation via the RNase H degradation pathway. The use of this pathway for degradation of target nucleic acids, as well as the enhanced stability of phosphorothioates,

creates the appeal of this particular antisense molecule. Other chemically altered oligonucleotides with modifications to the phosphate backbone, sugar moieties, or nucleotide bases [160, 166] have been employed to minimize degradation or off-target effects of antisense drugs while preserving their specific hybridization to target DNAs/RNAs. Most of these modifications[166] produce antisense molecules which function via steric inhibition of translation, splicing, or transcription of target nucleic acids. Antisense RNAs have also been chemically modified, via replacement of the ribose sugar 2' oxygen with a 2' O-methyl group or a 2'-florine, to resist enzymatic degradation and thus to have longer functional lifetimes in physiological environments.

The criteria of an 'efficient' antisense oligonucleotide have been enumerated as follows[162]: sequence-specific target recognition, high affinity for target DNA or RNA substrates, resistance to nuclease activity, sufficient plasma half-life, minimal 'off-target' or non-sequence-specific effects, and in ideal cases activation of RNase H, which effects degradation of target RNAs. Also, an important alternative to further chemical modifications is the discovery and synthesis of novel nanoparticulate carriers[119, 167] that will both protect and efficiently 'shuttle' drugs such as antisense oligonucleotides into cells[165].

1.7.2 RNAi

RNA interference, or RNAi, is an emerging technology which involves the delivery of double-stranded siRNAs (small interfering RNAs) which activate intrinsic pathways leading to the enzymatic degradation of targeted (complementary) mRNAs[163, 168]. These pathways traditionally involve the enzyme complexes known as DICER and RISC, the latter of which functions in the unwinding of small double-stranded RNAs and in the cleavage of complementary RNAs[162]. RNAi, which is mediated by ssRNAs or small dsRNAs delivered to

targeted cells, is related to endogenous microRNA pathways[162], which serve to naturally regulate gene expression in higher organisms including humans.

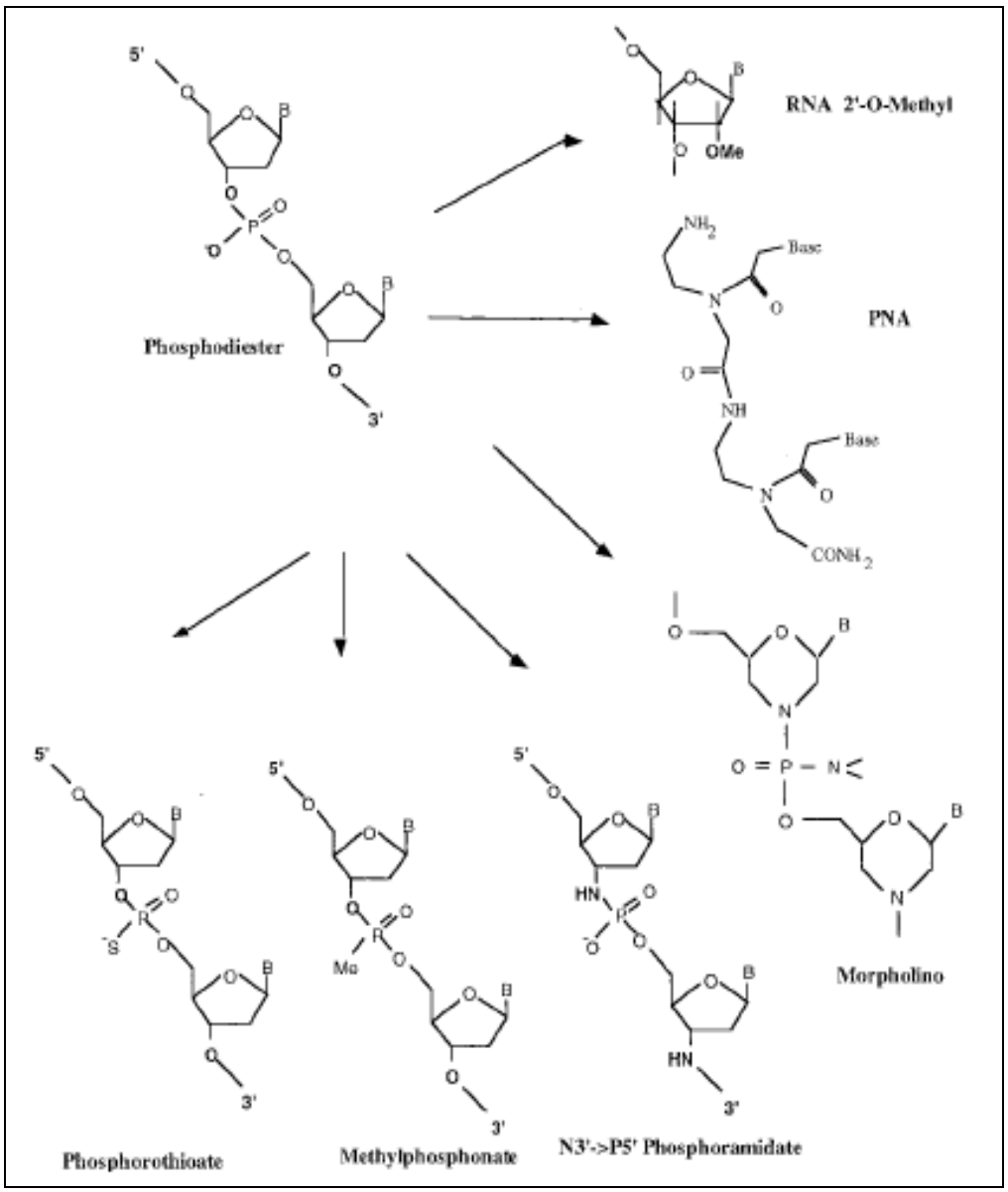

Figure 1.5 - Chemically modified antisense oligonucleotides (Dias & Stein 2002)[160]

1.8 Single vs Double Stranded RNA for Gene Delivery

Although the role of duplex RNA is critical in the early stages of RNAi and PTGS technology, there are multiple reports of single-stranded RNA (ssRNA) initiating the mRNA

knockdown. Martinez et al [170] reported that although ssRNA were involved in the RISC complex gene knockdown system, they required 10-100 fold higher concentrations of ssRNA compared to dsRNA to achieve the same effects. The knockdown was optimal for ssRNA that were >17 nt and improved by the addition of a 5' phosphate. Similar results were reinforced by Schwarz et al [171] when they evaluated both miRNA and siRNA and demonstrated that ssRNA for let-7 and luciferase mRNA required 5' phosphate. ssRNA mediated knock down is dosage dependant and is ~8-fold less effective than the corresponding duplex. Another study found that ssRNA, for human blood clotting initiator tissue factor (TF), was effective as the dsRNA at higher (100-200 nM) concentration[172].

More importantly, the core components of RISC have been shown to bind to ssRNAs. *In vitro* binding studies have shown that ssRNA have almost 70-100 fold higher affinity than dsRNA. Also, 21 nt long ssRNA with 5'phosphate bind to the recombinant Dicer with preferential affinity [173, 174]. The ease of functionalizing SNPs with ssRNA and their affinity for RISC complexes allowed us to select ssRNA over dsRNA for gene knockdown and differentiation of hASCs. dsRNA may be more potent than ssRNA but present the difficulty of attaching photo-cleavable group of the strand.

1.9 Stem Cells and Differentiation

1.9.1 Development of Germ Layers

After the initial three days of fertilization, through mitotic division, the zygote changes to a mast of cells which then changes to blastocyst comprised of an outer layer, trophoblast, and an inner layer, the inner cell mast (ICM). The blastocysts are filled with uterine fluid and undergo implantation. Initially the ICM has two layers; hypoblast and epiblast. The epiblast later forms a new layer called endoderm and after pushing out the hypoblast, it forms the next two layers,

mesoderm and ectoderm.[169] Every germ layer gives rise to progenitor cells which are then differentiated to terminally differentiated cells. Some examples of terminally differentiated cells include central nervous, head connective tissues and mammary glands from ectoderm layer, stomach, colon, liver, pancreas and bladder from endoderm and skeleton, heart, kidney and spleen from mesoderm (Figure 1-6).

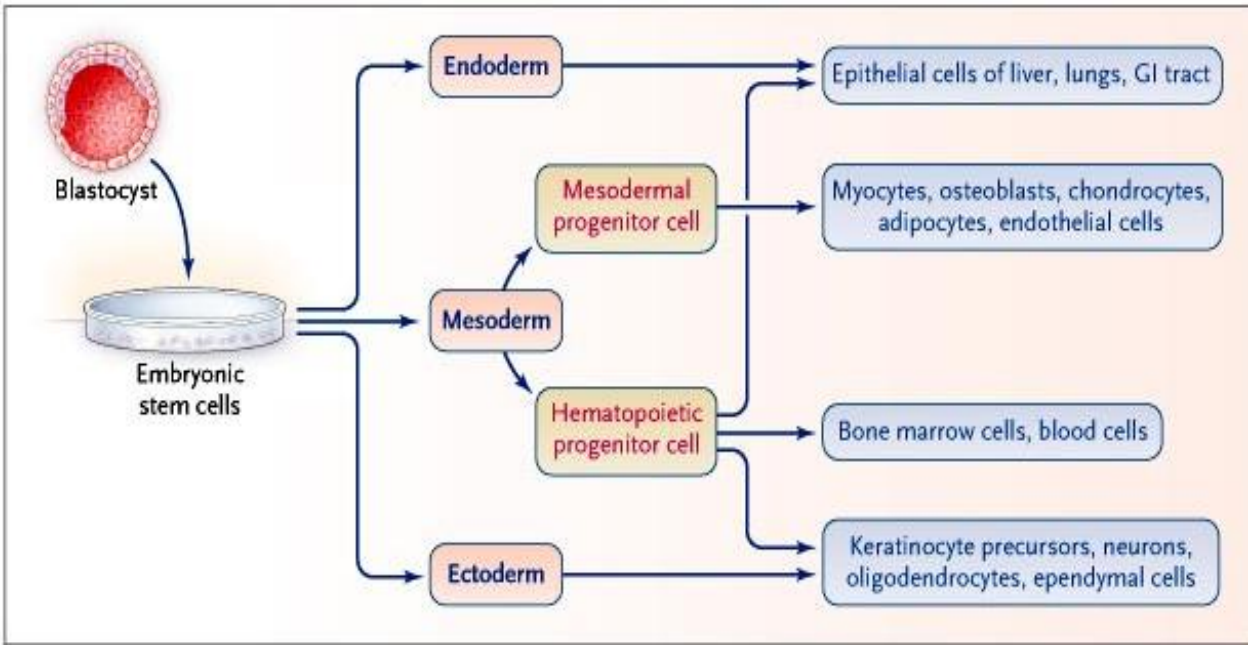

Figure 1.6 – Germ Layer development and their differentiation lineages[170].

1.9.2 Adult Stem Cells

Highly regulated processes of cell proliferation, migration, differentiation, and maturation, multiple cell lineages result in adult organisms from the earliest cell type in the chain called stem cells. The human adult stem cells are self-renewing and are capable of differentiating into multiple cell lineages (often multipotential). Upon physiologic cell turnover, tissue damage due to injury or againg, these cells are capable of maintaining, generating, and replacing terminally differentiated cells within their own specific tissue.[171, 172]. Some examples of differentiated cells from their parent progenitor cells are listed in Figure 1-7.

Cell Type	Tissue-Specific Location	Cells or Tissues Produced
Hematopoietic stem cells	Bone marrow, peripheral blood	Bone marrow and blood lymphohematopoietic cells
Mesenchymal stem cells	Bone marrow, peripheral blood	Bone, cartilage, tendon, adipose tissue, muscle, marrow stroma, neural cells
Neural stem cells	Ependymal cells, astrocytes (subventricular zone) of the central nervous system	Neurons, astrocytes, oligodendrocytes
Hepatic stem cells	In or near the terminal bile ductules (canals of Hering)	Oval cells that subsequently generate hepatocytes and ductular cells
Pancreatic stem cells	Intraislet, nestin-positive cells, oval cells, duct cells	Beta cells
Skeletal-muscle stem cells or satellite cells	Muscle fibers	Skeletal muscle fibers
Stem cells of the skin (keratinocytes)	Basal layer of the epidermis, bulge zone of the hair follicles	Epidermis, hair follicles
Epithelial stem cells of the lung	Tracheal basal and mucus-secreting cells, bronchiolar Clara cells, alveolar type II pneumocyte	Mucous and ciliated cells, type I and II pneumocytes
Stem cells of the intestinal epithelium	Epithelial cells located around the base of each crypt	Paneth's cells, brush-border enterocytes, mucus-secreting goblet cells, enteroendocrine cells of the villi

Figure 1.7: Adult human stem cells and their primary direction of differentiation

1.9.3 Mesenchymal Progenitor Cells

The bone marrow not only contains hematopoietic stem cells, but also the stem cells that can be defined as mesenchymatic. Traditionally mesenchymal stem cells (MSC) are found in the bone marrow but mesenchymal progenitor cells have been derived from multiple sources such as bone marrow[173], skeletal muscle[174], cartilage[175], tendon[176], adipose[177] and vascular smooth muscle cells[178]. These multiple studies have reported and indentified that MSC are great for self-renewal while maintaining their multipotency. They have also shown to

differentiate into osteoblasts, adipocytes, and chondrocytes as well as myocytes and neurons (Figure 1.8)

The mesoderm layer differentiates into hematopoietic and connective tissue and mesenchyme is one of the embryonic connective tissue. On the other hand, stromal cells are connective tissue cells that form the supportive structure in which the functional cells of the tissue reside. With recent advancements in the isolation of MSC from non marrow sources, a better alternate suggested name can be termed as Multipotent Stromal cells. Various beneficial aspects of mesenchymal stem cells (MSC) including their ease of isolation and culture, high *ex vivo* expansion potential and their multipotency draws great attraction in terms of clinical applications.

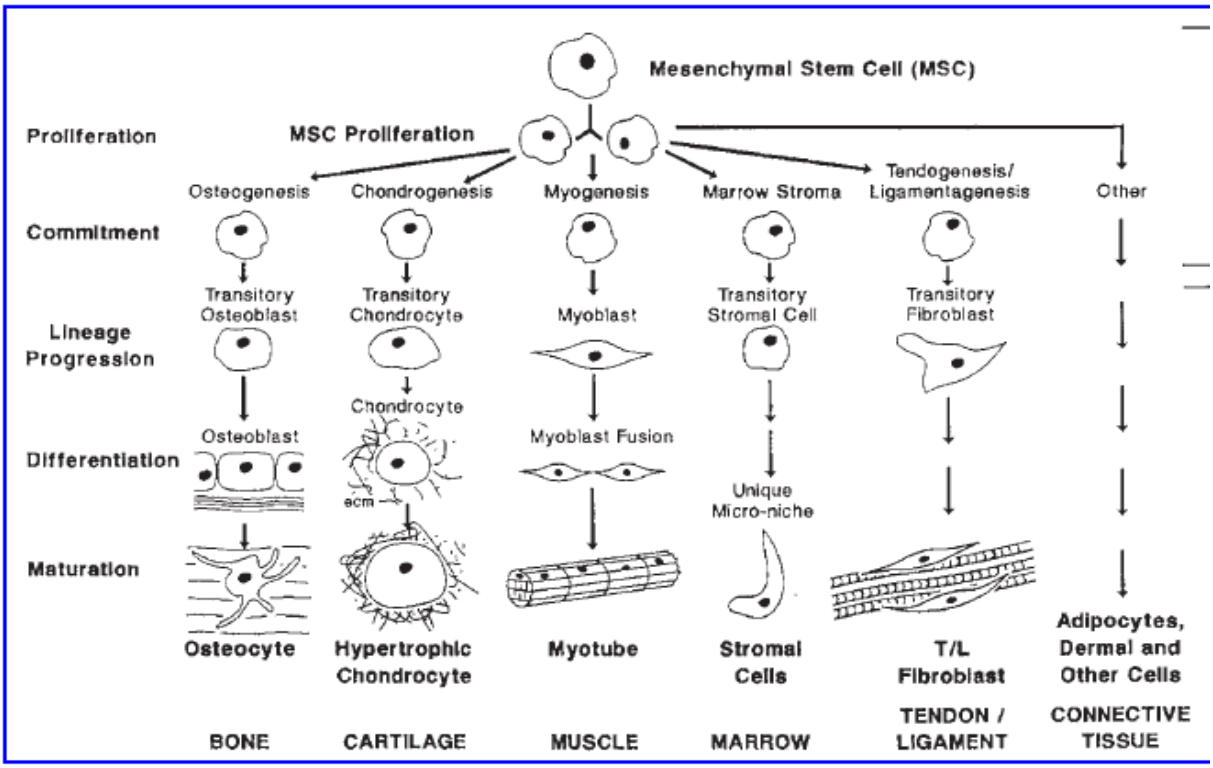

Figure 1.8**:** MSCs have the capacity to differentiate into multiple tissues. [179]

1.9.4 Osteogenic Differentiation of MSCs

Mesenchymal stem cells are multipotent and can either replicate as undifferentiated cells or differentiate into lineages including including bone, cartilage, fat, tendon, muscle, and marrow stroma. Researchers have demonstrated that MSCs are capable of differentiating into bone and cartilage when placed into an appropriate environment in vivo [180]. Currently, MSC derived from adipose tissue are differentiated towards osteogenic lineages using culture medium supplemented with L-ascorbic acid 2-phosphate (AsA2-P), dexamethasone (Dex) and beta-glycerophosphate (beta-GP)[181]

1.10 Therapeutic Approach

The genetically inherited skeletal tissue defects were cured by "cell replacement therapy," in which the host stem cells were replaced by healthy donor cells. Clinically the MCS based therapies can be implemented in three different ways; 1) tissue-engineering strategies in which MSCs are incorporated into 3-D synthetic and biocompatible scaffolds, 2) replacement of mutant host cells with normal allogeneic donor cells and 3) MSCs provide growth factor that stimulate reparative events or to inhibit degenerative events. Herein, we will use a combination (miRNA) with MSCs derived from adipose tissue and incorporate them into biomaterial based scaffolds for *in vivo* regeneration of skeletal bone

1.10.1 MicroRNA as Therapeutic Differentiation Agent

Modulation of gene expression with microRNA (miRNA) is a promising technique for improving control of wound healing and tissue repair processes.[182] These short, non-coding RNA's are involved in post-transcriptional regulation pathways and in their mature form are found as single strands often associated with RNA silencing complexes.[183] MicroRNA's utilized in autologous, adipose derived mesenchymal stem cells (ASC) are an attractive

therapeutic modality for regenerative medicine. Directing the osteogenic and angiogenic differentiation of ASC is of particular interest in the design of therapies for critical size bone defects, spinal fusion and skeletal reconstruction. A summary of relevant osteogenic and angiogenic miRNA sequences can be found in Table 1. Four miRNAs, miR-26a, -148b, -27a and -489, have shown to regulate osteogenesis in mesenchymal stem cells (MSC). Of these compounds, miR-148b has been shown to induce *de novo* osteogenesis as indicated by increases in total alkaline phosphatase activity and early specific biomarker expression [184]. Several miRNAs, miR-126, 132, antagomiR-92a and let-7f, play a role in the regulation of angiogenesis and tumorigenesis (Table 1). While the expression of all six of these miRNA's modulate angiogenesis, none have demonstrated *de novo* angiogenic activity and only miR-126 has been explored in stem cells [185, 186].

Table 1.1: Relevant osteogenic miRNAs. miRNAs in bold will be evaluated.

	miRNA	**Relevant Targets**	**Function**	**Reference**
Osteogenic	miR-26a	hASC	targets SMAD1 transcription factor	[187]
	miR-125b	Mouse MSC	inhibits osteogenesis	[188]
	miR-148b	hMSC	*de novo* osteogenesis	[184]
	miR-27a	hMSC	osteogenic	[184]
	miR-489	hMSC	osteogenic	[184]
Adipogenic	miR-21	hMSC	adipogenic (control)	(49)

1.11 Clinical Relevance

1.11.1 Bioscaffolds as Bone Cement Replacements

Reducing or preventing the antibiotic resistance of microorganisms is one of the prime objectives of researchers in trauma surgery, to avoid infection and delayed wound healing. In

Chapter 2 we describe the synthesize of SNPs containing PLLA–PEG polymer scaffolds formed via a directional cryoprecipitation process, and the release of entrapped SNPs to onsite bacteria, while concomitantly supporting the growth of hASCs. Either of these individual functionalities has significant biomedical applications, whereas their combination has implications for surgery, where all are desired. The bioscaffolds in this formulation had lower ultimate compressive stress compared to other commercially available antibiotic-injected polymers, but the improved antimicrobial efficacy makes them a promising candidate to be used as bone cements for bone or soft tissue defects.

1.11.2 Preventing Heterotopic Ossification in Bone Repair Therapies

While the technology described in Chapters 3 and 4 has the potential to impact the treatment of many clinical conditions as it addresses the control of osteogenesis in stem cell mediated bone repair. Providing clinicians with improved spatial and temporal control of osteogenesis could address conditions such as heterotopic ossification (HO) which occurs frequently during surgical skeletal repair. Heterotopic ossification, the mineralization of soft tissue also known as osseous metaplasia, is often associated with diffusible therapies such as bone morphogenic protein (BMP) used in repair of bone defects.[189] Maintenance of appropriate osteogenic concentrations with such short half-life diffusible factors at the site of bone repair requires high doses, resulting in a gradient of the bioactive compound in the surrounding soft tissue that can result in ectopic bone formation.[190-193] In cases where it is associated with joint or spinal tissue, the clinical complications of HO can be serious and costly for health care providers to correct.[194-199] Attempts to mediate the delivery of diffusible factors through localized injection and controlled release substrates have met with only limited success as control and localization of the dose remain problematic.[200-202]

Several other studies have examined gene delivery, using viral vectors or infected/transfected stem cells as an alternative to improve localization of osteogenic factors.[203-206] Direct viral vector delivery as a means of driving osteogenesis remains hampered by imprecise control over which cells are infected and levels of protein expression post infection. Injection of infected/transfected cells provides an effective means of localization but safety concerns related to levels of osteogenic protein expression and temporal control (i.e. when expression is turned on/off) limits enthusiasm for this technique.

The miRNA-SNP system may serve as a potential solution to HO and related complications by providing greater temporal and spatial control over the activation of differentiation (Figure 1.9). While the miRNA-SNP conjugate or cells transfected with miRNA-SNP may diffuse *in vivo,* they remain inert until activated with light, which can easily be pinpointed. Additionally, since miRNA are short lived and only transiently modulate mRNA expression, it is expected that there is little chance of permanent activity once an activated cell has begun differentiation. The miRNA associated with inactivated conjugate are expected to degrade slowly intracellularly or in the intercellular space through enzymatic action or hydrolysis.

This represents a paradigm shift from current methods of delivering osteogenic compounds such as diffusible BMP or gene delivery for BMP where there is little spatial or temporal control of expression respectively. The miRNA-SNP platform addresses both of these issues as: 1) miRNA payload can be activated with focused laser precision allowing activity only in the area of the bone defect, and 2) because miRNA are labile, activity is transient resulting in pathway regulation only in the critical early stages of cell differentiation. Additionally, as the

miRNA will only be transfected efficiently when bound to the particle, miRNA from conjugate activated in the intercellular space will have little impact on surrounding tissue.

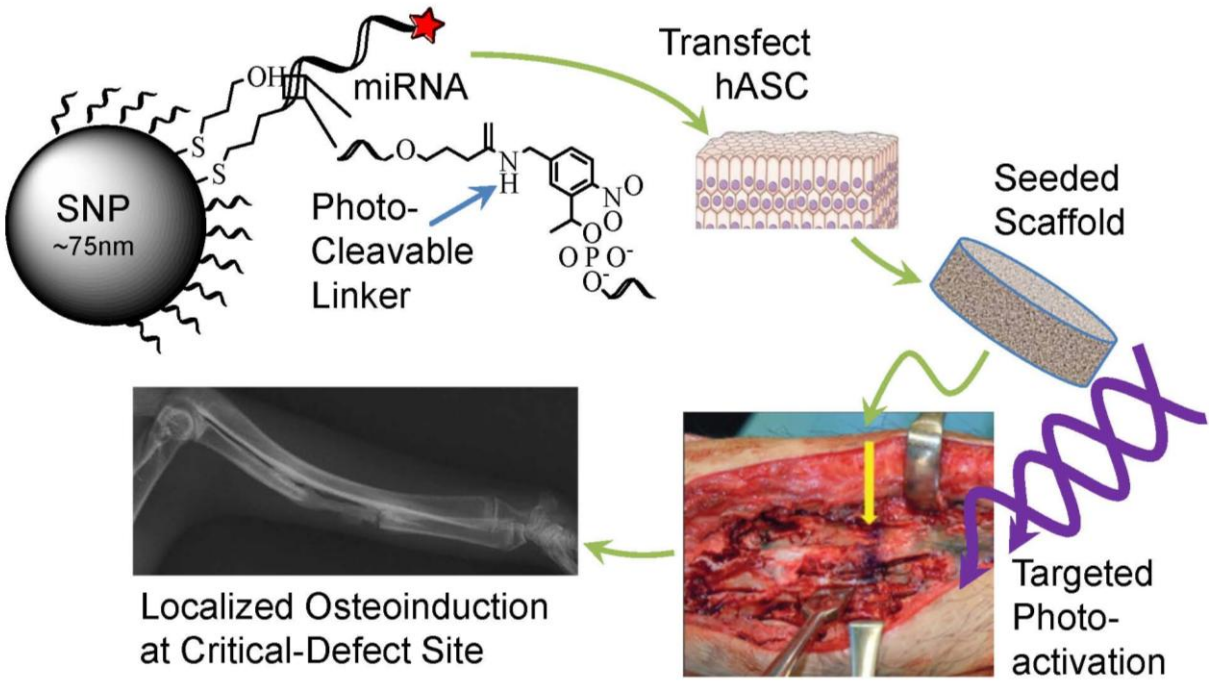

Figure 1.9. Overview of potential clinical implementation of Light Activated, miRNA Delivery system. Injection of LAMD near critical bone defects, (or in seeded scaffolds,) followed by targeted photoactivation induces differentiation at select sites, with minimal side effects such as heterotopic ossification (HO).

1.12 References

1. *Tissue, Cell and Organ Engineering*. Nanotechnologies for the Life Sciences, ed. C. Kumar. Vol. 9. 2006, Weinheim: WILEY-VCH Verlag GmbH & Co. KGaA.

2. Katz, E. and I. Willner, *Integrated nanoparticle-biomolecule hybrid systems: Synthesis, properties, and applications.* Angewandte Chemie-International Edition, 2004. **43**(45): p. 6042-6108.

3. Han, G., P. Ghosh, and V.M. Rotello, *Functionalized gold nanoparticles for drug delivery.* Nanomedicine, 2007. **2**(1): p. 113-123.

4. Ghosh, P., et al., *Gold nanoparticles in delivery applications.* Advanced Drug Delivery Reviews, 2008. **60**(11): p. 1307-1315.

5. Seferos, D.S., et al., *Polyvalent DNA Nanoparticle Conjugates Stabilize Nucleic Acids.* Nano Letters, 2009. **9**(1): p. 308-311.

6. Hutter, E. and J.H. Fendler, *Exploitation of localized surface plasmon resonance.* Advanced Materials, 2004. **16**(19): p. 1685-1706.

7. Kelly, K.L., et al., *The optical properties of metal nanoparticles: The influence of size, shape, and dielectric environment.* Journal of Physical Chemistry B, 2003. **107**(3): p. 668-677.

8. Moskovits, M., *SURFACE-ENHANCED SPECTROSCOPY.* Reviews of Modern Physics, 1985. **57**(3): p. 783-826.

9. Tokareva, I. and E. Hutter, *Hybridization of oligonucleotide-modified silver and gold nanoparticles in aqueous dispersions and on gold films.* Journal of the American Chemical Society, 2004. **126**(48): p. 15784-15789.

10. Giljohann, D.A., et al., *Oligonucleotide loading determines cellular uptake of DNA-modified gold nanoparticles.* Nano Letters, 2007. **7**(12): p. 3818-3821.

11. Giljohann, D.A., et al., *Gene Regulation with Polyvalent siRNA-Nanoparticle Conjugates.* Journal of the American Chemical Society, 2009. **131**(6): p. 2072-+.

12. Rosi, N.L., et al., *Oligonucleotide-modified gold nanoparticles for intracellular gene regulation.* Science, 2006. **312**(5776): p. 1027-1030.

13. Agasti, S.S., et al., *Photoregulated Release of Caged Anticancer Drugs from Gold Nanoparticles.* Journal of the American Chemical Society, 2009. **131**(16): p. 5728-+.

14. Boisselier, E. and D. Astruc, *Gold nanoparticles in nanomedicine: preparations, imaging, diagnostics, therapies and toxicity.* Chemical Society Reviews, 2009. **38**(6): p. 1759-1782.

15. Emerich, D.F. and C.G. Thanos, *The pinpoint promise of nanoparticle-based drug delivery and molecular diagnosis.* Biomolecular Engineering, 2006. **23**(4): p. 171-184.

16. Kamat, P.V., *Photophysical, photochemical and photocatalytic aspects of metal nanoparticles.* Journal of Physical Chemistry B, 2002. **106**(32): p. 7729-7744.

17. Maier, S.A., *Plasmonics: Fundamentals and Applications* 2007, New York: Springer.

18. Mie, G., *Articles on the optical characteristics of turbid tubes, especially colloidal metal solutions.* Annalen Der Physik, 1908. **25**(3): p. 377-445.

19. Schatz, G.C., *Using theory and computation to model nanoscale properties.* Proceedings of the National Academy of Sciences of the United States of America, 2007. **104**(17): p. 6885-6892.

20. Storhoff, J.J., et al., *What controls the optical properties of DNA-linked gold nanoparticle assemblies?* Journal of the American Chemical Society, 2000. **122**(19): p. 4640-4650.

21. Yguerabide, J. and E.E. Yguerabide, *Light-scattering submicroscopic particles as highly fluorescent analogs and their use as tracer labels in clinical and biological applications - I. Theory.* Analytical Biochemistry, 1998. **262**(2): p. 137-156.

22. Vidal, B.C., et al., *Stability and hybridization-driven aggregation of silver nanoparticle-oligonucleotide conjugates.* New Journal of Chemistry, 2005. **29**(6): p. 812-816.

23. Steinbruck, A., et al., *Gold-silver and silver-silver nanoparticle constructs based on DNA hybridization of thiol- and amino-functionalized oligonucleotides.* Journal of Biophotonics, 2008. **1**(2): p. 104-113.

24. Link, S. and M.A. El-Sayed, *Size and temperature dependence of the plasmon absorption of colloidal gold nanoparticles.* Journal of Physical Chemistry B, 1999. **103**(21): p. 4212-4217.

25. Uwe Kriebig, M.V., *Optical Properties of Metal Clusters*. Springer Series in Materials Science, ed. U. Gonser. Vol. 25. 1995, Heidelberg, Germany: Springer.

26. Jain, P.K., et al., *Review of some interesting surface plasmon resonance-enhanced properties of noble metal nanoparticles and their applications to biosystems.* Plasmonics, 2007. **2**(3): p. 107-118.

27. Lakowicz, J.R., *Principles of Fluorescence Spectroscopy*. Third ed2006, Singapore: Springer.

28. Yguerabide, J. and E.E. Yguerabide, *Light-scattering submicroscopic particles as highly fluorescent analogs and their use as tracer labels in clinical and biological applications - II. Experimental characterization.* Analytical Biochemistry, 1998. **262**(2): p. 157-176.

29. Nitzan, A. and L.E. Brus, *THEORETICAL-MODEL FOR ENHANCED PHOTOCHEMISTRY ON ROUGH SURFACES.* Journal of Chemical Physics, 1981. **75**(5): p. 2205-2214.

30. Myli, K.B., S.R. Coon, and V.H. Grassian, *PHOTON-INDUCED REACTIONS OF AROMATICS ADSORBED ON ROUGH AND SMOOTH SILVER SURFACES.* Journal of Physical Chemistry, 1995. **99**(44): p. 16407-16415.

31. Heard, S.M., et al., *THE CHARACTERIZATION OF AG SOLS BY ELECTRON-MICROSCOPY, OPTICAL-ABSORPTION, AND ELECTROPHORESIS.* Journal of Colloid and Interface Science, 1983. **93**(2): p. 545-555.

32. Chou, K.S. and C.Y. Ren. *Synthesis of nanosized silver particles by chemical reduction method*. Elsevier Science Sa.

33. Khanna, P.K., et al., *Water based simple synthesis of re-dispersible silver nano-particles.* Materials Letters, 2007. **61**(16): p. 3366-3370.

34. Zayat, M., D. Einot, and R. Reisfeld, *In-situ formation of AgCl nanocrystallites in films prepared by the sol-gel and silver nanoparticles in silica glass films.* Journal of Sol-Gel Science and Technology, 1997. **10**(1): p. 67-74.

35. Katayama, Y., M. Sasaki, and E. Ando. *THERMAL AND PHOTOCHEMICAL FORMATION OF SMALL GOLD COLLOIDS IN SOL-GEL FILMS*. 1994. Elsevier Science Bv.

36. Gacoin, T., et al., *COMPLEXED METAL-CLUSTERS IN ORGANICALLY MODIFIED OXIDE MATRICES.* Chemistry of Materials, 1993. **5**(8): p. 1150-1156.

37. Mennig, M., M. Schmitt, and H. Schmidt. *Synthesis of Ag-colloids in sol-gel derived SiO2-coatings on glass*. Kluwer Academic Publ.

38. Kozuka, H. and S. Sakka. *FORMATION OF SILICA-GELS COMPOSED OF MICROMETER-SIZED PARTICLES BY THE SOL-GEL METHOD*. 1994. Amer Chemical Soc.

39. Hinsch, A. and A. Zastrow. *THE PRODUCTION OF SMALL COLLOIDAL SILVER PARTICLES IN THIN SIO2 SOL-GEL GLASS LAYERS*. 1992. Elsevier Science Bv.

40. Adachi, M., S. Tsukui, and K. Okuyama, *Nanoparticle formation mechanism in CVD reactor with ionization of source vapor.* Journal of Nanoparticle Research, 2003. **5**(1-2): p. 31-37.

41. Adachi, M., M. Kusumi, and S. Tsukui, *Ion-induced nucleation in nanoparticle synthesis by ionization chemical vapor deposition.* Aerosol Science and Technology, 2004. **38**(5): p. 496-505.

42. Nakaso, K., et al., *Synthesis of non-agglomerated nanoparticles by an electrospray assisted chemical vapor deposition (ES-CVD) method.* Journal of Aerosol Science, 2003. **34**(7): p. 869-881.

43. Jung, J.H., H.H. Park, and S.S. Kim, *Effects of corona discharge ions on the synthesis of silver nanoparticles by a supersonic nozzle expansion method.* Journal of Vacuum Science & Technology B, 2007. **25**(1): p. 169-174.

44. Mukherjee, P., et al., *Fungus-mediated synthesis of silver nanoparticles and their immobilization in the mycelial matrix: A novel biological approach to nanoparticle synthesis.* Nano Letters, 2001. **1**(10): p. 515-519.

45. Simkiss, K.a.W., K.M., *Biomineralization; Cell Biology and Mineral Deposition*1989: Academic Press. 337.

46. Mann, S., *Biomimetic Materials Chemistry*1996, New York: Cambridge: VCH Publishers.

47. Spring, S., K.L. Scheifer, *Diversity of Magnetotactic Bacteria.* System. Appl. Microbiol, 1995. **18**: p. 147-153.

48. Dickson, D.P.E. *Nanostructured magnetism in living systems*. 1999. Elsevier Science Bv.

49. Mann, S., *MOLECULAR TECTONICS IN BIOMINERALIZATION AND BIOMIMETIC MATERIALS CHEMISTRY*. Nature, 1993. **365**(6446): p. 499-505.

50. Oliver, S., et al., *LAMELLAR ALUMINOPHOSPHATES WITH SURFACE PATTERNS THAT MIMIC DIATOM AND RADIOLARIAN MICROSKELETONS.* Nature, 1995. **378**(6552): p. 47-50.

51. Pum, D. and U.B. Sleytr, *The application of bacterial S-layers in molecular nanotechnology.* Trends in Biotechnology, 1999. **17**(1): p. 8-12.

52. Sleytr, U.B., et al., *Crystalline bacterial cell surface layers (S layers): From supramolecular cell structure to biomimetics and nanotechnology.* Angewandte Chemie-International Edition, 1999. **38**(8): p. 1035-1054.

53. Mandal, D., et al., *The use of microorganisms for the formation of metal nanoparticles and their application.* Applied microbiology and biotechnology, 2006. **69**(5): p. 485-492.

54. Klaus, T., et al., *Silver-based crystalline nanoparticles, microbially fabricated.* Proceedings of the National Academy of Sciences of the United States of America, 1999. **96**(24): p. 13611-13614.

55. Haefeli, C., C. Franklin, and K. Hardy, *PLASMID-DETERMINED SILVER RESISTANCE IN PSEUDOMONAS-STUTZERI ISOLATED FROM A SILVER MINE.* Journal of Bacteriology, 1984. **158**(1): p. 389-392.

56. Kramer, R.M., et al., *Engineered protein cages for nanomaterial synthesis.* Journal of the American Chemical Society, 2004. **126**(41): p. 13282-13286.

57. Chandra, R., et al., *Synthesis and TEM study of nanoparticles and nanocrystalline thin films of silver by high pressure sputtering.* Nanostructured Materials, 1999. **11**(8): p. 1171-1179.

58. Karthikeyan, J., et al., *Plasma spray synthesis of nanomaterial powders and deposits.* Materials Science and Engineering a-Structural Materials Properties Microstructure and Processing, 1997. **238**(2): p. 275-286.

59. Chih, Y.W. and W.T. Cheng, *Supercritical carbon dioxide-assisted synthesis of silver nano-particles in polyol process.* Materials Science and Engineering B-Solid State Materials for Advanced Technology, 2007. **145**(1-3): p. 67-75.

60. Clasen, C. and W.M. Kulicke, *Determination of viscoelastic and rheo-optical material functions of water-soluble cellulose derivatives.* Progress in Polymer Science, 2001. **26**(9): p. 1839-1919.

61. Wong, D. and R. Bodmeier, *Flocculation of an aqueous colloidal ethyl cellulose dispersion (Aquacoat(R)) with a water-soluble polymer, hydroxypropyl methylcellulose.* European Journal of Pharmaceutics and Biopharmaceutics, 1996. **42**(1): p. 12-15.

62. Weir, E., et al., *The use of nanoparticles in anti-microbial materials and their characterization.* Analyst, 2008. **133**(7): p. 835-845.

63. Gaboriaud, F. and Y.F. Dufrene, *Atomic force microscopy of microbial cells: Application to nanomechanical properties, surface forces and molecular recognition forces.* Colloids and Surfaces B-Biointerfaces, 2007. **54**(1): p. 10-19.

64. Qi, L.F., et al., *Preparation and antibacterial activity of chitosan nanoparticles.* Carbohydrate Research, 2004. **339**(16): p. 2693-2700.

65. Xu, J., et al., *Synthesis and optical properties of silver nanoparticles stabilized by gemini surfactant.* Colloids and Surfaces a-Physicochemical and Engineering Aspects, 2006. **273**(1-3): p. 179-183.

66. Davies, E., et al., *Ultra-high resolution imaging of DNA and nucleosomes using non-contact atomic force microscopy.* Febs Letters, 2005. **579**(7): p. 1702-1706.

67. Kim, J.H., et al., *Effect of the polymer matrix on the formation of silver nanoparticles in polymer-silver salt complex membranes.* Journal of Polymer Science Part B-Polymer Physics, 2006. **44**(8): p. 1168-1178.

68. Sambhy, V., et al., *Silver bromide nanoparticle/polymer composites: Dual action tunable antimicrobial materials.* Journal of the American Chemical Society, 2006. **128**(30): p. 9798-9808.

69. Bruce J. Berne, R.P., *Dynamic Light Scattering with Applications to Chemistry, Biology, and Physics*2000, N.Y.: Dover Publications. Inc.

70. Joachim Koetz, S.K., *Polyelectrolytes and Nanoparticles*2007, New York: Springer.

71. Gao, Y., et al., *Evidence for the monolayer assembly of poly(vinylpyrrolidone) on the surfaces of silver nanowires.* Journal of Physical Chemistry B, 2004. **108**(34): p. 12877-12881.

72. Andic, Z., et al., *The synthesis of ultrafine and nanocomposite powders based on copper, silver anal alumina.* Kovove Materialy-Metallic Materials, 2006. **44**(3): p. 145-150.

73. Wagatsuma, K., *Application of modulation techniques to atomic emission spectrometry with inductively-coupled radio-frequency plasma and radio-frequency glow discharge plasma.* Applied Spectroscopy Reviews, 2002. **37**(2): p. 223-245.

74. Lansdown, A., *Silver I: its antibacterial properties and mechanism of action.* JOURNAL OF WOUND CARE, 2002. **11**(4): p. 125-131.

75. Sondi, I. and B. Salopek-Sondi, *Silver nanoparticles as antimicrobial agent: a case study on E. coli as a model for Gram-negative bacteria.* Journal of Colloid and Interface Science, 2004. **275**(1): p. 177-182.

76. Stobie, N., et al., *Prevention of Staphylococcus epidermidis biofilm formation using a low-temperature processed silver-doped phenyltriethoxysilane sol-gel coating.* Biomaterials, 2008. **29**(8): p. 963-969.

77. Sambhy, V., et al., *Silver Bromide Nanoparticle/Polymer Composites: Dual Action Tunable Antimicrobial Materials.* Journal of the American Chemical Society, 2006. **128**(30): p. 9798-9808.

78. Darouiche, R., et al., *A comparison of two antimicrobial-impregnated central venous catheters. Catheter Study Group.* New England Journal of Medicine, 1999. **340**(1): p. 1-8.

79. Greenfeld, J., et al., *Decreased bacterial adherence and biofilm formation on chlorhexidine and silver sulfadiazine-impregnated central venous catheters implanted in swine.* Critical Care Medicine, 1995. **23**(5): p. 894.

80. Tan, S., et al., *Study on the structure and antibacterial activity of silver-carried zirconium phosphate.* Materials Letters, 2008. **62**(14): p. 2122-2124.

81. Khare, M.D., et al., *Reduction of catheter-related colonisation by the use of a silver zeolite-impregnated central vascular catheter in adult critical care.* Journal of Infection, 2007. **54**(2): p. 146-150.

82. Cowan, M.M., et al., *Antimicrobial efficacy of a silver-zeolite matrix coating on stainless steel.* Journal of Industrial Microbiology and Biotechnology, 2003. **30**(2): p. 102-106.

83. DRITCH, E., et al., *Silver Nylon Cloth: In vitro and in vivo Evaluation of Antimicrobial Activity.* The Journal of Trauma: Injury, Infection, and Critical Care, 1987. **27**(3): p. 301.

84. Rai, M., A. Yadav, and A. Gade, *Silver nanoparticles as a new generation of antimicrobials.* Biotechnology Advances, 2009. **27**(1): p. 76-83.

85. Klasen H, *A historical review of the use of silver in the treatment of burns. Part I early uses.* Burns, 2000. **30**: p. 1-9.

86. Rosenkra.Hs and H.S. Carr, *SILVER SULFADIAZINE - EFFECT ON GROWTH AND METABOLISM OF BACTERIA.* Antimicrobial Agents and Chemotherapy, 1972. **22**(5): p. 367-&.

87. Bragg, P.D. and D.J. Rainnie, *EFFECT OF SILVER IONS ON RESPIRATORY-CHAIN OF ESCHERICHIA-COLI.* Canadian Journal of Microbiology, 1974. **20**(6): p. 883-889.

88. Schreurs, W.J.A. and H. Rosenberg, *EFFECT OF SILVER IONS ON TRANSPORT AND RETENTION OF PHOSPHATE BY ESCHERICHIA-COLI.* Journal of Bacteriology, 1982. **152**(1): p. 7-13.

89. Yamanaka, M., K. Hara, and J. Kudo, *Bactericidal actions of a silver ion solution on Escherichia coli, studied by energy-filtering transmission electron microscopy and proteomic analysis.* Applied and Environmental Microbiology, 2005. **71**(11): p. 7589-7593.

90. Richards, R.M.E., *ANTIMICROBIAL ACTION OF SILVER-NITRATE.* Microbios, 1981. **31**(124): p. 83-91.

91. Kjolseth, D., et al., *COMPARISON OF THE EFFECTS OF COMMONLY USED WOUND AGENTS ON EPITHELIALIZATION AND NEOVASCULARIZATION.* Journal of the American College of Surgeons, 1994. **179**(3): p. 305-312.

92. Sambhy, V., B.R. Peterson, and A. Sen, *Multifunctional Silane Polymers for Persistent Surface Derivatization and Their Antimicrobial Properties.* Langmuir, 2008. **24**(14): p. 7549-7558.

93. Adams, A.P., E.M. Santschi, and M.A. Mellencamp, *Antibacterial properties of a silver chloride-coated nylon wound dressing.* Veterinary Surgery, 1999. **28**(4): p. 219-225.

94. Carr, H.S., Wlodkows.Tj, and Rosenkra.Hs, *SILVER SULFADIAZINE - IN-VITRO ANTIBACTERIAL ACTIVITY.* Antimicrobial Agents and Chemotherapy, 1973. **4**(5): p. 585-587.

95. Gallant-Behm, C.L., et al., *Comparison of in vitro disc diffusion and time kill-kinetic assays for the evaluation of antimicrobial wound dressing efficacy.* Wound Repair & Regeneration, 2005. **13**(4): p. 412-421.

96. Muller, G. and A. Kramer, *Biocompatibility index of antiseptic agents by parallel assessment of antimicrobial activity and cellular cytotoxicity.* J. Antimicrob. Chemother., 2008. **61**(6): p. 1281-1287.

97. Chaby, G., et al., *Insuffisance rÈnale aiguÎ aprËs application topique de sulfadiazine argentique.* Annales de Dermatologie et de VÈnÈrÈologie, 2005. **132**(11, Part 1): p. 891-893.

98. Muller, M.J., et al., *Retardation of wound healing by silver sulfadiazine is reversed by Aloe vera and nystatin.* Burns, 2003. **29**(8): p. 834-836.

99. Simon, V., C. Albon, and S. Simon, *Silver release from hydroxyapatite self-assembling calcium-phosphate glasses.* Journal of Non-Crystalline Solids, 2008. **354**(15-16): p. 1751-1755.

100. Balamurugan, A., et al., *An in vitro biological and anti-bacterial study on a sol-gel derived silver-incorporated bioglass system.* Dental Materials, 2008. **24**(10): p. 1343-1351.

101. Dai, J.M., et al., *Study on the color change resistant property of silver and zinc-loading zeolite 4A antibacterial agent.* Journal of Inorganic Materials, 2008. **23**(5): p. 1011-1015.

102. Carrel, T., et al., *Definitive cure of recurrent prosthetic endocarditis using silver-coated St. Jude Medical heart valves: a preliminary case report.* J Heart Valve Dis, 1998. **7**(5): p. 531-3.

103. Kjaergard, H., et al., *Recurrent endocarditis in silver-coated heart valve prosthesis.* J Heart Valve Dis, 1999. **8**(2): p. 140-2.

104. Benn, T.M. and P. Westerhoff, *Nanoparticle Silver Released into Water from Commercially Available Sock Fabrics.* Environmental Science & Technology, 2008. **42**(11): p. 4133-4139.

105. Roe, D., et al., *Antimicrobial surface functionalization of plastic catheters by silver nanoparticles.* Journal of Antimicrobial Chemotherapy, 2008. **61**(4): p. 869-876.

106. Wang, H., et al., *Preparation of silver nanoparticles by chemical reduction method.* Colloids and Surfaces A: Physicochemical and Engineering Aspects, 2005. **256**(2-3): p. 111-115.

107. Sun, Y. and Y. Xia, *Shape-Controlled Synthesis of Gold and Silver Nanoparticles*, in *Science*2002. p. 2176-2179.

108. Wu, R.-T. and S.L.-C. Hsu, *Preparation of highly concentrated and stable suspensions of silver nanoparticles by an organic base catalyzed reduction reaction.* Materials Research Bulletin, 2008. **43**(5): p. 1276-1281.

109. Raffi, M., et al., *Studies of the growth parameters for silver nanoparticle synthesis by inert gas condensation.* Journal of Materials Research, 2007. **22**: p. 3378-3384.

110. Vigneshwaran, N., et al., *Silver-protein (core-shell) nanoparticle production using spent mushroom substrate.* Langmuir, 2007. **23**(13): p. 7113-7117.

111. Han, G., et al., *Light-regulated release of DNA and its delivery to nuclei by means of photolabile gold nanoparticles.* Angewandte Chemie-International Edition, 2006. **45**(19): p. 3165-3169.

112. Vivero-Escoto, J.L., et al., *Photoinduced Intracellular Controlled Release Drug Delivery in Human Cells by Gold-Capped Mesoporous Silica Nanosphere.* Journal of the American Chemical Society, 2009. **131**(10): p. 3462-+.

113. Niemeyer, C.M., *Nanoparticles, proteins, and nucleic acids: Biotechnology meets materials science.* Angewandte Chemie-International Edition, 2001. **40**(22): p. 4128-4158.

114. Sokolova, V. and M. Epple, *Inorganic nanoparticles as carriers of nucleic acids into cells.* Angewandte Chemie-International Edition, 2008. **47**(8): p. 1382-1395.

115. Mintzer, M.A. and E.E. Simanek, *Nonviral Vectors for Gene Delivery.* Chemical Reviews, 2009. **109**(2): p. 259-302.

116. Oishi, M., et al., *Smart PEGylated gold nanoparticles for the cytoplasmic delivery of siRNA to induce enhanced gene silencing.* Chemistry Letters, 2006. **35**(9): p. 1046-1047.

117. Song, W.J., et al., *Gold Nanoparticles Capped with Polyethyleneimine for Enhanced siRNA Delivery.* Small, 2010. **6**(2): p. 239-246.

118. Shack, J., *INFLUENCE OF SODIUM AND MAGNESIUM IONS ON THE ACTION OF DEOXYRIBONUCLEASE-II.* Journal of Biological Chemistry, 1959. **234**(11): p. 3003-3006.

119. Toub, N., et al., *Innovative nanotechnologies for the delivery of oligonucleotides and siRNA.* Biomedicine & Pharmacotherapy, 2006. **60**(9): p. 607-620.

120. Patel, P.C., et al., *Scavenger Receptors Mediate Cellular Uptake of Polyvalent Oligonucleotide-Functionalized Gold Nanoparticles.* Bioconjugate Chemistry, 2010. **21**(12): p. 2250-2256.

121. Ragusa, A., I. Garcia, and S. Penades, *Nanoparticles as nonviral gene delivery vectors.* Ieee Transactions on Nanobioscience, 2007. **6**(4): p. 319-330.

122. Poliseno, L., et al., *MicroRNAs modulate the angiogenic properties of HUVECs.* Blood, 2006. **108**(13976096728479933779related:U6WLD-0R9cEJ): p. 3068.

123. Davis, B.N., et al., *Induction of microRNA-221 by platelet-derived growth factor signaling is critical for modulation of vascular smooth muscle phenotype.* Journal of Biological Chemistry, 2009. **284**(6): p. 3728.

124. Kim, Y.S., et al., *Twenty-eight-day oral toxicity, genotoxicity, and gender-related tissue distribution of silver nanoparticles in Sprague-Dawley rats.* Inhalation Toxicology, 2008. **20**(6): p. 575-583.

125. Tiwari, D.K., T. Jin, and J. Behari, *Dose-dependent in-vivo toxicity assessment of silver nanoparticle in Wistar rats.* Toxicology Mechanisms and Methods, 2011. **21**(1): p. 13-24.

126. Thompson, D.G., et al., *Ultrasensitive DNA detection using oligonucleotide-silver nanoparticle conjugates.* Analytical Chemistry, 2008. **80**(8): p. 2805-2810.

127. Graham, D., et al., *Functionalized nanoparticles for bioanalysis by SERRS.* Biochemical Society Transactions, 2009. **37**: p. 697-701.

128. Fu, Y., J. Zhang, and J.R. Lakowicz, *Plasmonic enhancement of single-molecule fluorescence near a silver nanoparticle.* Journal of Fluorescence, 2007. **17**(6): p. 811-816.

129. Wolkow, R.A. and M. Moskovits, *ENHANCED PHOTOCHEMISTRY ON SILVER SURFACES.* Journal of Chemical Physics, 1987. **87**(10): p. 5858-5869.

130. AshaRani, P.V., et al., *Cytotoxicity and Genotoxicity of Silver Nanoparticles in Human Cells.* ACS Nano, 2009. **3**(2): p. 279-290.

131. Link, S. and M. El-Sayed, *Size and temperature dependence of the plasmon absorption of colloidal gold nanoparticles.* J. Phys. Chem. B, 1999. **103**(21): p. 4212-4217.

132. Zhang, L., et al., *Reducing Stress on Cells with Apoferritin-Encapsulated Platinum Nanoparticles.* Nano Letters, 2009. **10**(1): p. 219-223.

133. Hung, W.H., et al., *Plasmon Resonant Enhancement of Carbon Monoxide Catalysis.* Nano Letters, 2010. **10**(4): p. 1314-1318.

134. Adleman, J.R., et al., *Heterogenous catalysis mediated by plasmon heating.* Nano Letters, 2009. **9**(12): p. 4417-4423.

135. Ung, T., L.M. Liz-Marzan, and P. Mulvaney, *Redox catalysis using Ag@ SiO2 colloids.* The Journal of Physical Chemistry B, 1999. **103**(32): p. 6770-6773.

136. Chowdhury, M.H., et al., *Metal-enhanced chemiluminescence: Radiating plasmons generated from chemically induced electronic excited states.* APPLIED PHYSICS LETTERS, 2006. **88**: p. 173104.

137. A. El-Ansary, S.A.-D., *On the Toxicity of Therapeutically Used Nanoparticles: An Overview.* Journal of Toxicology, 2009.

138. Chung, Y.C., I.H. Chen, and C.J. Chen, *The surface modification of silver nanoparticles by phosphoryl disulfides for improved biocompatibility and intracellular uptake.* Biomaterials, 2008. **29**(12): p. 1807-1816.

139. Arora, S., et al., *Interactions of silver nanoparticles with primary mouse fibroblasts and liver cells.* Toxicology and Applied Pharmacology, 2009. **236**(3): p. 310-318.

140. Storhofff, J.J., et al., *Sequence-dependent stability of DNA-modified gold nanoparticles.* Langmuir, 2002. **18**(17): p. 6666-6670.

141. Li, H.X. and L. Rothberg, *Colorimetric detection of DNA sequences based on electrostatic interactions with unmodified gold nanoparticles.* Proceedings of the National Academy of Sciences of the United States of America, 2004. **101**(39): p. 14036-14039.

142. Thomas, K.G. and P.V. Kamat, *Chromophore-functionalized gold nanoparticles.* Accounts of Chemical Research, 2003. **36**(12): p. 888-898.

143. Herne, T.M. and M.J. Tarlov, *Characterization of DNA probes immobilized on gold surfaces.* Journal of the American Chemical Society, 1997. **119**(38): p. 8916-8920.

144. Sun, Y., N.C. Harris, and C.H. Kiang, *Phase transition and optical properties of DNA-gold nanoparticle assemblies.* Plasmonics, 2007. **2**(4): p. 193-199.

145. Demers, L.M., et al., *A fluorescence-based method for determining the surface coverage and hybridization efficiency of thiol-capped oligonucleotides bound to gold thin films and nanoparticles.* Analytical Chemistry, 2000. **72**(22): p. 5535-5541.

146. Hurst, S.J., A.K.R. Lytton-Jean, and C.A. Mirkin, *Maximizing DNA loading on a range of gold nanoparticle sizes.* Analytical Chemistry, 2006. **78**(24): p. 8313-8318.

147. Hill, H.D., et al., *The Role Radius of Curvature Plays in Thiolated Oligonucleotide Loading on Gold Nanoparticles.* Acs Nano, 2009. **3**(2): p. 418-424.

148. Alvarez-Lorenzo, C., L. Bromberg, and A. Concheiro, *Light-sensitive Intelligent Drug Delivery Systems.* Photochemistry and Photobiology, 2009. **85**(4): p. 848-860.

149. Ellis-Davies, G.C.R., *Caged compounds: photorelease technology for control of cellular chemistry and physiology.* Nature Methods, 2007. **4**(8): p. 619-628.

150. Monroe, W.T., et al., *Targeting expression with light using caged DNA.* Journal of Biological Chemistry, 1999. **274**(30): p. 20895-20900.

151. Buff, M., T. Mack, and A. Heckel, *Light-Activatable Nucleic Acids 'Caged' at the Nucleobases.* Chimia, 2009. **63**(5): p. 261-264.

152. Pelliccioli, A.P. and J. Wirz, *Photoremovable protecting groups: reaction mechanisms and applications.* Photochemical & Photobiological Sciences, 2002. **1**(7): p. 441-458.

153. Kaplan, J.H., B. Forbush, and J.F. Hoffman, *RAPID PHOTOLYTIC RELEASE OF ADENOSINE 5'-TRIPHOSPHATE FROM A PROTECTED ANALOG - UTILIZATION BY NA-K PUMP OF HUMAN RED BLOOD-CELL GHOSTS.* Biochemistry, 1978. **17**(10): p. 1929-1935.

154. Walker, J.W., et al., *PHOTOLABILE 1-(2-NITROPHENYL)ETHYL PHOSPHATE-ESTERS OF ADENINE-NUCLEOTIDE ANALOGS - SYNTHESIS AND MECHANISM OF PHOTOLYSIS.* Journal of the American Chemical Society, 1988. **110**(21): p. 7170-7177.

155. Bai, X.P., et al., *Photocleavage of a 2-nitrobenzyl linker bridging a fluorophore to the 5' end of DNA.* Proceedings of the National Academy of Sciences of the United States of America, 2003. **100**(2): p. 409-413.

156. Olejnik, J., E. KrzymanskaOlejnik, and K.J. Rothschild, *Photocleavable biotin phosphoramidite for 5'-end-labeling, affinity purification and phosphorylation of synthetic oligonucleotides.* Nucleic Acids Research, 1996. **24**(2): p. 361-366.

157. Li, Z.M., et al., *A photocleavable fluorescent nucleotide for DNA sequencing and analysis.* Proceedings of the National Academy of Sciences of the United States of America, 2003. **100**(2): p. 414-419.

158. Dorman, G. and G.D. Prestwich, *Using photolabile ligands in drug discovery and development.* Trends in Biotechnology, 2000. **18**(2): p. 64-77.

159. Lakowicz, J.R., et al., *Enhanced and localized multiphoton excited fluorescence near metallic silver islands: Metallic islands can increase probe photostability.* Journal of Fluorescence, 2002. **12**(3-4): p. 299-302.

160. Dias, N. and C.A. Stein, *Antisense oligonucleotides: Basic concepts and mechanisms.* Molecular Cancer Therapeutics, 2002. **1**(5): p. 347-355.

161. Wu, H.J., et al., *Determination of the role of the human RNase H1 in the pharmacology of DNA-like antisense drugs.* Journal of Biological Chemistry, 2004. **279**(17): p. 17181-17189.

162. Sahu, N.K., et al., *Antisense technology: A selective tool for gene expression regulation and gene targeting.* Current Pharmaceutical Biotechnology, 2007. **8**(5): p. 291-304.

163. Pan, W.H. and G.A. Clawson, *Antisense applications for biological control.* Journal of Cellular Biochemistry, 2006. **98**(1): p. 14-35.

164. Eder PS, D.R., Dagle JM, Walder JA,, *Substrate specificity and kinetics of degradation of antisense oligonucleotides by a 3' exonuclease in plasma.* Antisense Research and Development, 1991. **1**(2): p. 141-151.

165. Roth, C.M., *Molecular and cellular barriers limiting the effectiveness of antisense oligonucleotides.* Biophysical Journal, 2005. **89**(4): p. 2286-2295.

166. Crooke, S.T., *Antisense Drug Technology: Principles, Strategies, and Applications*. 2nd ed2008, Boca Ranton: CRC Press Taylor & Francis Group.

167. Lambert, G., E. Fattal, and P. Couvreur, *Nanoparticulate systems for the delivery of antisense oligonucleotides.* Advanced Drug Delivery Reviews, 2001. **47**(1): p. 99-112.

168. Fire, A., et al., *Potent and specific genetic interference by double-stranded RNA in Caenorhabditis elegans.* Nature, 1998. **391**(6669): p. 806-811.

169. Gilbert, S.F., *Developmental Biology*. Vol. Part 2. 2000, Sunderland (MA): Swarthmoe College.

170. Korbling, M. and Z. Estrov, *Adult stem cells for tissue repair - A new therapeutic concept?* New England Journal of Medicine, 2003. **349**(6): p. 570-582.

171. Slack, J.M.W., *Stem cells in epithelial tissues.* Science, 2000. **287**(5457): p. 1431-1433.

172. Weissman, I.L., *Stem cells: Units of development, units of regeneration, and units in evolution.* Cell, 2000. **100**(1): p. 157-168.

173. Caplan, A.I., *THE MESENGENIC PROCESS.* Clinics in Plastic Surgery, 1994. **21**(3): p. 429-435.

174. Williams, J.T., et al., *Cells isolated from adult human skeletal muscle capable of differentiating into multiple mesodermal phenotypes.* American Surgeon, 1999. **65**(1): p. 22-26.

175. Caplan, A.I., et al., *Principles of cartilage repair and regeneration.* Clinical Orthopaedics and Related Research, 1997(342): p. 254-269.

176. BernardBeaubois, K., et al., *Culture and characterization of juvenile rabbit tenocytes.* Cell Biology and Toxicology, 1997. **13**(2): p. 103-113.

177. Bukowiecki, L.J., A. Geloen, and A.J. Collet, *PROLIFERATION AND DIFFERENTIATION OF BROWN ADIPOCYTES FROM INTERSTITIAL-CELLS DURING COLD-ACCLIMATION.* American Journal of Physiology, 1986. **250**(6): p. C880-C887.

178. Hellstrom, M., et al., *Role of PDGF-B and PDGFR-beta in recruitment of vascular smooth muscle cells and pericytes during embryonic blood vessel formation in the mouse.* Development, 1999. **126**(14): p. 3047-3055.

179. Caplan, A.I., *Review: mesenchymal stem cells: cell-based reconstructive therapy in orthopedics.* Tissue Engineering, 2005. **11**(7-8): p. 1198-1211.

180. Jaiswal, N., et al., *Osteogenic differentiation of purified, culture-expanded human mesenchymal stem cells in vitro.* Journal of Cellular Biochemistry, 1997. **64**(2): p. 295-312.

181. Kyllonen, L., et al., *Effects of different serum conditions on osteogenic differentiation of human adipose stem cells in vitro.* Stem Cell Research & Therapy, 2013. **4**(1): p. 17.

182. Rhim, C., et al., *Effect of MicroRNA Modulation on Bioartificial Muscle Function.* Tissue Engineering Part A, 2010: p. 3589-3597.

183. Ambros, V., *The functions of animal microRNAs.* Nature, 2004. **431**(7006): p. 350-355.

184. Schoolmeesters, A., et al., *Functional Profiling Reveals Critical Role for miRNA in Differentiation of Human Mesenchymal Stem Cells.* Plos One, 2009. **4**(5): p. 9.

185. Fish, J.E., et al., *miR-126 regulates angiogenic signaling and vascular integrity.* Developmental cell, 2008. **15**(2): p. 272-284.

186. Wang, S., et al., *The endothelial-specific microRNA miR-126 governs vascular integrity and angiogenesis.* Developmental cell, 2008. **15**(2): p. 261-271.

187. Luzi, E., et al., *Osteogenic differentiation of human adipose tissue-derived stem cells is modulated by the miR-26a targeting of the SMAD1 transcription factor.* Journal of Bone and Mineral Research, 2008. **23**(2): p. 287-295.

188. Mizuno, Y., et al., *miR-125b inhibits osteoblastic differentiation by down-regulation of cell proliferation.* Biochemical and Biophysical Research Communications, 2008. **368**(2): p. 267-272.

189. McCarthy, E. and M. Sundaram, *Heterotopic ossification: a review.* Skeletal radiology, 2005. **34**(10): p. 609-619.

190. Harel, D., *High-dose bone morphogenetic protein, induced ectopic abdomen bone growth.* The Spine Journal, 2010. **10**(2): p. e1-e4.

191. Benglis, D., M.Y. Wang, and A.D. Levi, *A comprehensive review of the safety profile of bone morphogenetic protein in spine surgery.* Neurosurgery, 2008. **62**(5): p. ONS423.

192. Vaidya, R., et al., *Complications in the use of rhBMP-2 in PEEK cages for interbody spinal fusions.* Journal of spinal disorders & techniques, 2008. **21**(8): p. 557.

193. Wong, D.A., et al., *Neurologic impairment from ectopic bone in the lumbar canal: a potential complication of off-label PLIF/TLIF use of bone morphogenetic protein-2 (BMP-2).* The Spine Journal, 2008. **8**(6): p. 1011-1018.

194. Riegler, H.F. and C.M. Harris, *Heterotopic bone formation after total hip arthroplasty.* Clinical Orthopaedics and Related Research, 1976. **117**: p. 209.

195. Thomas, B., *Heterotopic bone formation after total hip arthroplasty.* The Orthopedic clinics of North America, 1992. **23**(2): p. 347.

196. Joseph, V. and Y.R. Rampersaud, *Heterotopic bone formation with the use of rhBMP2 in posterior minimal access interbody fusion: a CT analysis.* Spine, 2007. **32**(25): p. 2885.

197. Boraiah, S., et al., *Complications of recombinant human BMP-2 for treating complex tibial plateau fractures: a preliminary report.* Clinical Orthopaedics and Related Research¬Æ, 2009. **467**(12): p. 3257-3262.

198. Crawford III, C.H., et al., *Perioperative complications of recombinant human bone morphogenetic protein-2 on an absorbable collagen sponge versus iliac crest bone graft for posterior cervical arthrodesis.* Spine, 2009. **34**(13): p. 1390.

199. Brower, R.S. and N.M. Vickroy, *A case of psoas ossification from the use of BMP-2 for posterolateral fusion at L4,L5.* Spine, 2008. **33**(18): p. E653.

200. Shields, L.B.E., et al., *Adverse effects associated with high-dose recombinant human bone morphogenetic protein-2 use in anterior cervical spine fusion.* Spine, 2006. **31**(5): p. 542.

201. Poynton, A.R. and J.M. Lane, *Safety profile for the clinical use of bone morphogenetic proteins in the spine.* Spine, 2002. **27**(16S): p. S40.

202. Patel, V.V., et al., *An in vitro and in vivo analysis of fibrin glue use to control bone morphogenetic protein diffusion and bone morphogenetic protein,Äìstimulated bone growth.* The Spine Journal, 2006. **6**(4): p. 397-403.

203. Kirker-Head, C.A., *Potential applications and delivery strategies for bone morphogenetic proteins.* Advanced Drug Delivery Reviews, 2000. **43**(1): p. 65-92.

204. Lieberman, J.R., et al., *Regional gene therapy with a BMP-2 producing murine stromal cell line induces heterotopic and orthotopic bone formation in rodents.* Journal of Orthopaedic Research, 1998. **16**(3): p. 330-339.

205. Gonda, K., et al., *Heterotopic Ossification of Degenerating Rat Skeletal Muscle Induced by Adenovirus-Mediated Transfer of Bone Morphogenetic Protein-2 Gene.* Journal of Bone and Mineral Research, 2000. **15**(6): p. 1056-1065.

206. Laurencin, C., et al., *Poly (lactide-co-glycolide)/hydroxyapatite delivery of BMP-2-producing cells: a regional gene therapy approach to bone regeneration.* Biomaterials, 2001. **22**(11): p. 1271-1277.

Chapter 2. Antimicrobial Biocompatible Bioscaffolds for Orthopedic Implants[1]

2.1 Project Summary

Nationally, nearly 1.5 million patients in U.S. suffer from ailments requiring bone grafts, hip and other joint replacements. Infections following internal fixation in orthopedic trauma can cause osteomyelitis in 22% to 66% of cases and if uncontrolled, the mortality rate can be as high as 2%. We characterize a procedure for synthesis of antimicrobial and biocompatible poly-L-lactic acid (PLLA) and poly ethyleneglycol (PEG) bioscaffolds designed to degrade and absorb at a controlled rate. The bioscaffold architecture aims to provide a suitable substrate for the controlled release of silver nanoparticles (SNP) to reduce bacterial growth as well as aid the proliferation of human adipose derived stem cells (h-ASCs) for tissue engineering applications. The fabricated bioscaffolds were characterized with scanning transmission microscope (SEM) and it shows the addition of increasing concentrations of SNP results in formation of dendritic porous channels perpendicular to the axis of precipitation. The antimicrobial properties of these porous bioscaffolds were tested according to a modified ISO 22196 standard across varying concentrations of biomass mediated SNPs to determine an efficacious antimicrobial concentration. The bioscaffolds reduced the *Staphylococcus aureus* and *Escherichia coli* viable colony forming units by 98.85% and 99.9%, respectively, at an antimicrobial SNP concentration of 2000 ppm. Human ASC were seeded on bioscaffolds and *in vitro* cultured for 20 days to study the effect of SNP concentration on the viability of cells. SEM analysis and metabolic activity based fluorescent dye, alamarBlue®, demonstrated the growth of cells on the antimicrobial efficacious bioscaffolds. The biocompatibility of *in vitro* leached silver, quantified by

[1] Reprinted with the permission of Journal of Tissue Engineering and Regenerative Medicine (Appendix A)

inductively coupled plasma optical emission spectroscopy (ICPOES), proved non-cytotoxic when tested against h-ASCs, evaluated by MTT assay.

2.2 Introduction

Infections following internal fixation in orthopedic trauma can cause significant setbacks to healing and have devastating long-term consequences. Traumatic injuries can involve significant soft tissue defects with exposed fractures in which there is a 22% to 66% rate of osteomyelitis, respectively, in civilian and military populations [1, 2]. Treatment for significant bony or soft tissue injuries usually require temporary stabilization (within 6 hr), prophylactic antibiotic therapy, irrigation/debridement, and subsequent definitive stabilization[2]. If uncontrolled, the mortality rates from osteomyelitis can be as high as 2 % [3]. Antibiotic-loaded bone cements, titanium cages, induced membranes, bone transport [4-6] have also been explored as prophylactic and therapeutic treatments for filling bone defects and treating osteomyelitis but their use has had limited clinical success. Despite these early and aggressive efforts, many patients (1-2%), predominantly young men with a median age of 24.5 and no co-morbidities, develop chronic osteomyelitis [7]. These patients would potentially benefit from engineered tissue repair solutions which reduce infection rates while improving regeneration of native tissue

Synthetic scaffolds are being increasingly explored as a potential therapeutic modality to address limitations of autologus tissue grafting and alloplastic tissue repair. These constructs are designed to deliver bioactive materials such as drugs, cells, genes, peptides and/or proteins concomitantly with a degradable scaffold. The materials and porous architecture common in most scaffold designs perform a critical function in tissue regeneration by maintaining tissue volume, providing temporary mechanical stability, and delivering bioactive compounds [8-13].

A variety of "natural" (occurring in nature) and synthetic materials have been identified or developed which broadly meet the criteria to be considered bioresorbable or bioerodible and thus serve as good candidates for scaffold synthesis. Some of the broad categories include aliphatic esters, chitosan, aliginates, polyhydroxy acids and poly(tyrosine-carbonates) [14]. Of these compounds the material and chemical properties of aliphatic esters such as poly-L-lactic acid (PLLA) and poly-L-glycolic acid (PLGA) make them of interest for many indwelling applications including wound care and orthopedic device applications. The *in vivo* degradation processes of these compounds have been well described and while there are some reports of the onset of late stage inflammation, these have been attributed to high molecular weight particles released from highly crystalline substrates [15, 16]. Most studies have found the implants with PLLA, PLGA or copolymers to result in very few rejection-related complications [17, 18].

Nanocomposite compounds provide a novel and flexible platform for incorporating drugs and other bioactive components into scaffolds. The large surface area and higher reactivity of nanoparticles when compared to bulk solids allow the particles to exhibit extraordinary chemical, physical and biological properties while the fundamentally small size minimizes the deleterious impacts traditionally associated with the formation of polymer composites containing a high volume fraction of solids [19]. Also, particles are means of achieving higher control of porosity, pore size, surface area and mechanical properties of scaffolds [20].

Herein we report on the development of a unidirectional cryoprecipitation process for forming monolithic, antimicrobial, multi-scalar nanocomposite scaffolds. This process, which makes use of a novel synthesis and purification methodology for silver nanoparticles (SNP) addresses the critical attributes of solubility, yield and purity, which to-date have prevented nanomaterials from widespread use in medical device applications. By varying the scaffold

composition and precipitation conditions, the fine micro- and nanostructure of this material can be controlled influencing the biocompatibility and reincorporation of materials into native bone structure. This manuscript describes the use of these two processes to develop proof of concept data supporting the use of antimicrobial nanocomposite scaffold composed of PLLA: polyethylene glycol and SNP to repair critical sized tissue defects. Scaffold microstructure, viscoelastic mechanical properties, and its potential to serve as a substrate for hASC growth is demonstrated. The SNP concentrations and *in vitro* contact times required for the elimination of known titers of two model organisms, *Staphylococcus aureus* and *Escherichia coli* are evaluated. Additionally, the cytotoxicity of the released SNP and hydrolyzed product of PLLA-PEG bioscaffolds is tested against hASC to determine the suitability for use in stem cell based regenerative therapies. The values obtained provide baseline data to assess how SNP can best be implemented in nanocomposite bioscaffolds to create engineered, active antimicrobial tissue scaffolds.

2.3 Materials and Methods

2.3.1 Microbiology Test Organisms

Escherichia coli (ATCC 29522) and *Staphylococcus aureus* (ATCC 6538) were inoculated and grown in sterile 15-ml centrifuge tubes (BD Falcon, Franklin Lakes, NJ) containing Nutrient Agar and BHI broth respectively and incubated at 37ºC.

2.3.2 Cell Culture

Human ASC were isolated according to the method described by Yu et al.[21] by the Stem Cell Biology Laboratory under a protocol reviewed and approved by the Institutional Review Board at Pennington Biomedical Research Center. The ASC were isolated from lipoaspirates obtained from consenting patients undergoing elective plastic surgery. Human ASC

were maintained in 25-cm^2 flasks (BD Falcon, Franklin Lakes, NJ) in stromal culture media at 37 °C and 5% CO_2 in a humidified atmosphere. Stromal culture media is composed of DMEM/Ham's F- 12 (1:1), 2.5 mm L-glutamine, 15mm HEPES supplemented with 10% Fetal Bovine Serum (FBS) and 1% Antibiotic Solution (100X with penicillin, streptomycin, fungizone) until 80-90% confluent. The third passage (P3) cells were used in the extraction and metabolism studies.

2.3.3 Biomass Mediated SNP Synthesis and Characterization

The hydroxypropyl cellulose (HPC) stabilized SNP were synthesized by reducing silver nitrate with formaldehyde and characterized by transmission electron microscopy (TEM) and UV-Vis spectroscopy as previously published [22]

2.3.4 Synthesis of Nanocomposite Scaffolds

PLLA and PEG (3.5% wt each) were co-dissolved in dehydrated 1, 4-dioxane, Sigma Aldrich, at 50^oC until transparent. Then 280 ul of deionized water (DI) water containing varying concentrations of colloidal SNP were mixed into the PLLA/PEG (M_w= 150,000 and 2200 respectively) solution. After cooling to room temperature (RT), the solution was poured into a closed 4 cm long glass vial and the bioscaffolds were synthesized using a uni-directional freezing method similar to that previously described to form three–dimensional polymer structures by thermal precipitation [23]. Briefly, the vials are lowered into a liquid nitrogen bath at a constant rate of 2 cm/hr by a KDS230P syringe pump (KD Scientific, Holliston, MA). The insulated liquid nitrogen bath was designed with three orifices, each only slightly larger than the glass vial, milled into the insulted lid through which the glass vials were lowered. This process minimized evaporation of the liquid nitrogen and allowed the freezing liquid nitrogen vapor to access only the portion of the vial that had transited the orifice. The vial caps were closed to prevent

absorption of moisture. After freezing the samples completely for two hours, the solidified PLLA:PEG sample was freeze-dried in Labconco FreeZone Plus (Kansas City, MO) at -85^{o}C for 4 days.

2.3.5 Characterization of Bioscaffolds

The solidified 2 cm long monolithic porous bioscaffolds were characterized with Joel JSM-6610LV (JEOL USA, Inc., Peabody, MA) scanning electron microscope (SEM) at 10 kV and inductively coupled plasma optical emission spectrometry (ICP-OES).

The middle section of the bioscaffold was cut with a sharp razor blade both parallel and perpendicular to the direction of freezing to get hemi-cylindrical shaped samples. These samples were mounted on aluminum stubs with either Tubecote or colloidal graphite and sputter coated with platinum in Edwards S-150 sputter coater (Edwards High Vacuum Co. International, Wilmington, Massachusetts, USA).

The amount of silver in the bioscaffolds was quantified by ICO-OES after digesting the contents with nitric acid. The acidified solution was transferred to weighed ICP vials, agitated for 2.5 hrs and diluted to a final volume of 10 ml with acidified water. The final vials are weighed and the diluted samples were run on Varian Vista MPX (Palo Alto, CA). A no-SNP containing control sample was also compared.

2.3.6 Antimicrobial Activity

Quantitative antimicrobial testing with S.*aureus* and *E. coli* were conducted according to a modified ISO 22196 test methods which has a detection limit of 30-300 bacterial colonies. Briefly, 300 ul of the inoculated bacterial cultures were exposed to three cylindrical sections (d=12 mm and h= 1mm), cut from the middle section of the bioscaffold, containing varying concentration of SNP for 24 hrs. The bioscaffolds were then washed with PBS to extract

S.*aureus* and *E. coli* and plated on Mannitol Salt Agar and MacConkey agar plates (BD Falcon, Franklin Lakes, NJ) respectively. A bioscaffold without SNP was also included in the dilution ladder as a control for each test organism to measure the efficacy of the coatings. The percentage reduction and colony forming unit (CFU) values were calculated similar to previously published work [22].

2.3.7 Bioscaffold Rheology

Compression analysis on the SNP-bioscaffolds was conducted using a 1kN load cell of Instron^{TM} 5582. Three cylindrical sections, 15 mm in height, of each concentration were compressed at a rate of 5mm/min until 90% strain was achieved. Stress-stain curves were plotted using the data collected from the BlueHill2 software (Instron, Norwood, MA).

2.3.8 *In vitro* Release of Silver from Bioscaffolds

SNP bioscaffolds, containing varying amount of SNP were exposed to 5 ml of PBS solution each for 5 days (n=3) at RT. Daily, 1 ml PBS solution was collected from each sample, without replacement for ICP-OES analysis. Prior to injection the solutions were incubated with 1 ml nitric acid, transferred to weighed ICP vials, agitated for 2.5 hrs and diluted to a final volume of 10 ml with acidified water. The final vials are weighed and the diluted samples were run on Varian Vista MPX (Palo Alto, CA). A no-SNP containing control sample was also included.

2.3.9 Cytotoxicity of Bioscaffold Extract on Human Adipose Stem Cells

Three 9 mm^3 cubes, cut from the middle of the bioscaffold, were placed in 2 ml Stromal culture media for 1, 5 and 20 days. On the respective day, the media (extract) was collected and tested against hASC using TACS^{TM} MTT Assay (Trevigen Inc, Gaithersburg, MD). A 100 ul cell solution ($1.5x10^5$ cell/ml) was added to each well of a 96-well plate (BD Falcon, Franklin Lakes, NJ) for 24 hrs. The media was then exchanged with 100 ul of the extract and incubated

with the adhered cells for 24 hrs. On the following day, 15 ul of the MTT Reagent was added to each well for 3 hrs followed by the addition of MTT Detergent for 3 hrs. The absorbance was measured with a Wallac VICTOR^2 V 1420-040 Multilabel Counter (PerkinElmer, Boston, MA) at 590 nm.

2.3.10 Growth of hASC on Bioscaffolds

The hASCs were grown on bioscaffolds to study the cytotoxicity of the SNPs and released silver ions when in direct contact with cells. The 1 mm thick bioscaffold discs, cut from 4 cm long bioscaffolds, were placed inside Plasma Cleaner 32PDC-23G (Harrick Plasma, Ithaca, NY) chamber and the internal pressure was lowered to 200 mTorr. The bioscaffolds were plasma treated for 10 sec to reduce the water contact angle for more facile hASC loading. This process does not impact the bulk properties of the bioscaffolds. The bioscaffolds were then incubated with 1 ml cell solution ($6x10^4$ cell/ml) in a 12-well plate (BD Falcon, Franklin Lakes, NJ) for 1, 5 and 20 days. The growth of hASC was qualitatively and quantitatively analyzed with SEM and a metabolic activity indicator, alamarBlue® (Invitrogen Carlsbad, CA) respectively.

To measure of metabolic activity, tissue cultured wells with no discs were seeded with an identical amount of cells as a positive control while wells with discs but no cells were employed as a negative control. On the respective days, the seeded discs were removed from the wells, washed with 1 ml of PBS and transferred to a fresh 12-well plate (to avoid the possibility of measuring cells seeded on to the initial well bottom during the seeding process). A 0.5 ml portion of the 10% (v/v) alamarBlue® in stromal media was added to each disc, positive and negative control wells for 4 hrs. Then 100 μl sample of the mixture was removed and the fluorescence (λ_{ex} =530 nm and λ_{em} =620 nm) was measured in a 96-well plate (BD Biosciences) using a Wallac VICTOR^2 V 1420-040 Multilabel Counter.

The discs seeded with hASC and cultured for 20 days were analyzed by SEM. The discs were removed from the cell media and fixed with 10% formaldehyde (Mallinckrodt Baker, NJ), 10% glutaraldehyde (EM Science, PA) and 80% D-PBS for 15 mins. They were then rinsed in PBS to remove any residual fixing solution and placed in clean 60 mm glass petri dishes containing 0.25% solution of OsO_4 in PBS for 30 mins at room temperature. The discs were washed with DI water and dehydrated with 50%, 70% and 100% ethanol for 15 mins each.

2.4 Results and Discussions

2.4.1 Characterization of Monolith Bioscaffolds

SEM micrographs of a PLLA/PEG 50:50 blend after unidirectional freezing and freeze-drying are shown in Figure 2.1. This cross-sectional view of the sample parallel to the direction of freezing (y-axis) provides an image of the honeycomb monolith structure, having 20 um inner diameter microtubes aligned along the freezing axis in the no SNP control (Fig. 2.1A). The uniform porosity of the bioscaffold was disturbed and the interconnected void space appeared more dendritic in structure with the addition of SNPs. The pores are oriented in the y-axis (Figure 2.1A) and with increasing concentration of SNPs (100 ppb – 200 ppm) the pores lose alignment along the y-axis and branch out in the y-x plane (Fig. 2.1 (B)-(I)). It is hypothesized that the inclusion of SNP reduces the long-range crystallinity of the freezing solvent and prevents the formation of large continuous solvent crystals reducing the orientation of the scaffold and resulting in more dendritic pores. The size of the pore is ideal for the growth of cells and holds promise for bioscaffolds to be used in regenerative therapies [24].

ICP-OES quantified the amount of Ag+ ions present in the bioscaffolds with varying concentration of SNP (Fig. 2.1G). The amount of SNP in the bioscaffolds does not correspond to

its theoretical values and this can be hypothesized as due to losses during freeze drying and nitric acid digestion processes.

2.4.2 Antimicrobial Activity of SNP in Bioscafffolds

The bioscaffold nanocomposite compounds were challenged with two microorganisms *E.coli* and *S.aureus.* These strains were chosen as they are the two most commonly occurring strains of bacteria in Healthcare Acquired Infections (HAI) and have demonstrated resistance to several antibiotics including amoxicillin and methicillin respectively [25]. A bioscaffold without SNP was also included in the dilution ladder as a control for each test organism to measure the antimicrobial activity of the bioscaffold polymers.

The percentage bacterial reduction across varying SNP concentration for *S.aureus* and *E.coli* on the monolithic bioscaffold is presented in Fig. 2.2. At every SNP concentration the *S.aureus* is more viable compared that of *E.coli.* The thick peptidoglycan layer *of S.aureus* is believed to be interacting with the silver ions reducing the cytotoxic activity compared to *E.coli*. The results are similar to chloramphenicol (Cm) doped PLGA nanofibers where the percentage of inhibition were also larger for *E.coli* compared to *S.aureus* [26].

At 2000 ppm SNP, the CFU/ml decreased from 1.01×10^9 to 4.20×10^6 and 2.16×10^7 to 2.48×10^5 for *E.coli* and *S.aureus* respectively. These reductions correspond to a 3 log reduction (99.9%) reduction for *E.coli* and 98.85% reduction for *S.aureus.* There is a clear shift in the antimicrobial efficacy as the concentration is increased from 1 ppm to 700 ppm. The average percentage reduction changed from 38.6% to 80.38% and 28% to 86.11% ($p < 0.05$) for *E.coli* and *S.aureus* (Fig. 2.2 (A and B)). These results are improvements compared to recent reports on antibiotics [6] and silver [27] injected bone cements or silver containing polymeric scaffolds [28].

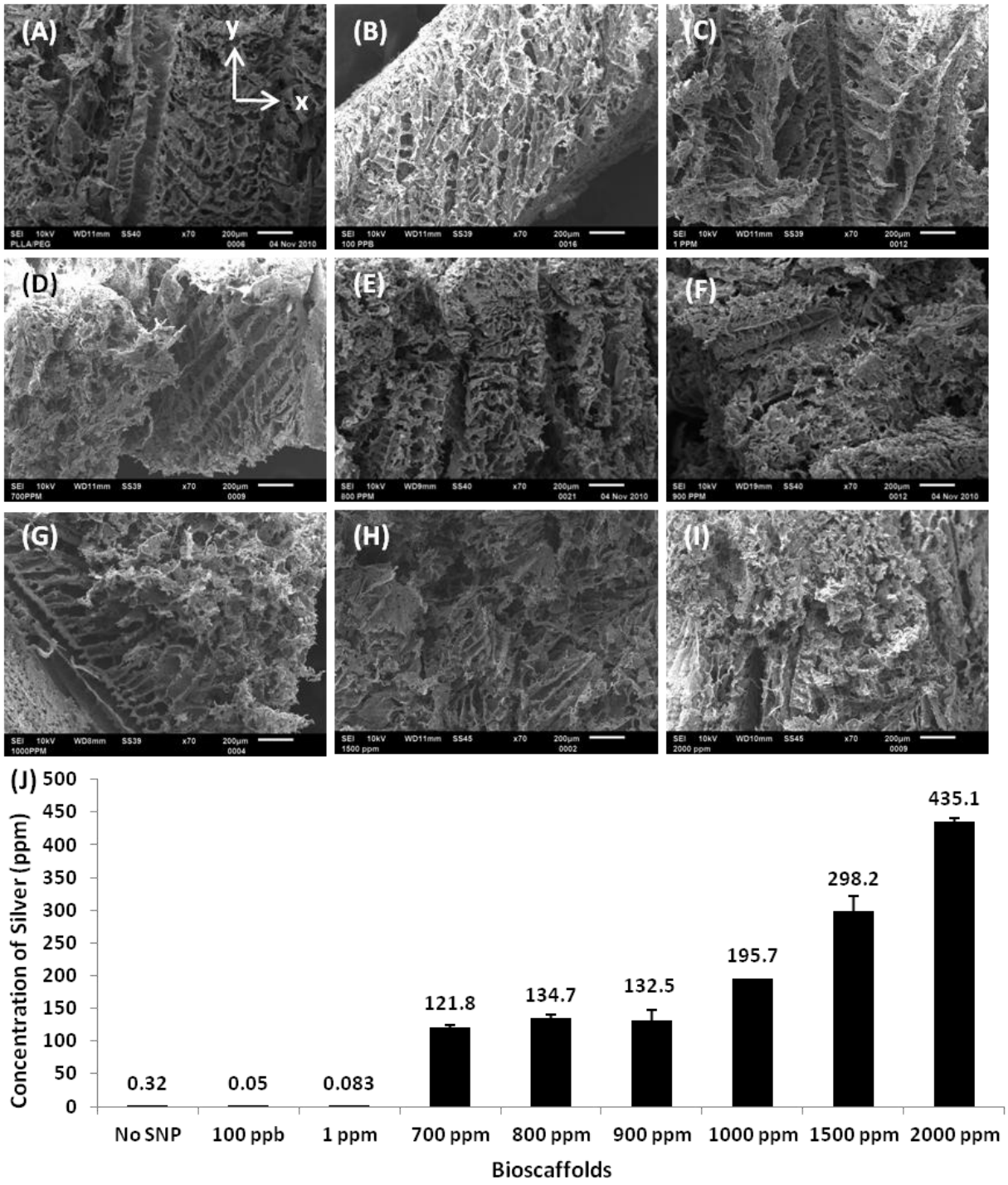

Figure 2.1. SEM images of PLLA/PEG 50:50 blend co-polymer monolith bioscaffolds containing varying amounts of SNP (A) No SNP, (B) 100 ppb, (C) 1 ppm, (D) 700 ppm, (E) 800 ppm, (F) 900 ppm, (G) 1000 ppm, (H) 1500 ppm and (I) 2000 ppm. (J) The amount of SNP in the bioscaffolds is quantified by ICPOES. The scale bar of SEM images are 200um.

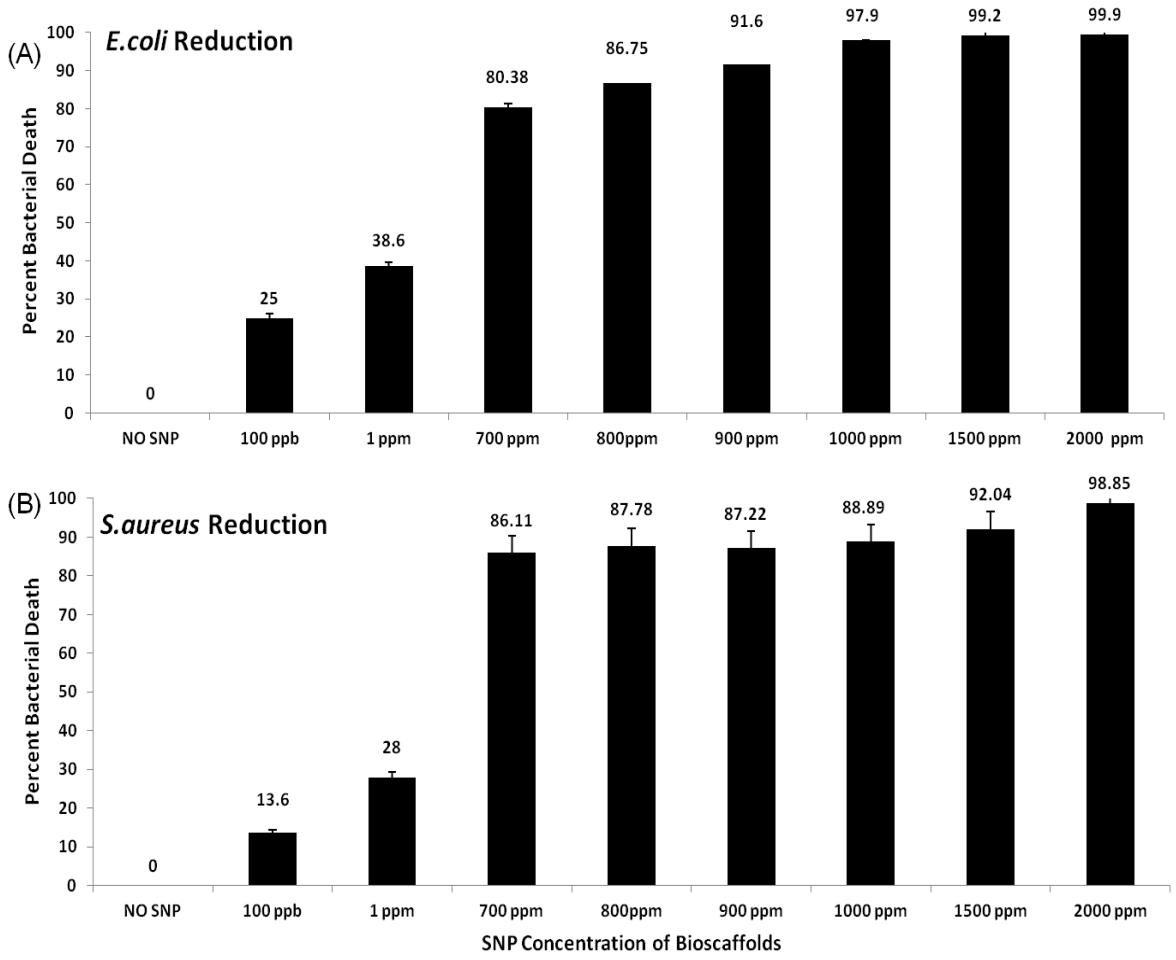

Figure 2.2. Percent reduction of (A) *E .coli* and (B) *S.aureus* when exposed to varying concentrations of SNP (n=3).

2.4.3 Mechanical Properties of Bioscaffold

The deformation of SNP-bioscaffolds when compressed in the direction of freezing follows a classical compressive stress–strain curve of samples with porous structures with distinct elastic and plastic regions. The compressive stress–strain curves of porous polymer scaffolds have three main characteristics: (a) linear elastic region at small strain (b) followed by a plateau region at larger stain and (c) a densified region with a very large increase in strain [29]. The rapid increase of the stress in the densified section occurred due to the collapse of the pore-walls of the scaffolds [30]. The elastic-plastic flexion of bioscaffold occurs at ~10% strain and

the stress in the plastic (densified) region exponentially increases around 60% strain. The compressive modulus ($E_{elastic}$), compressive stress at 10% strain (σ_{10}) which is a common indicator for the compressive properties of porous scaffolds are listed in Table 2.1 along with the ultimate compressive stress and average tangent modulus from 60-90% strain. The ultimate compressive stress decreases from 64.5 ± 26.5 kPa for no SNP control to 39.9 ± 1.4 kPa at 90% strain for 2000 ppm (Fig. 2.3). By increasing the amount of SNP, the ultimate stress of bioscaffolds decreases, which can be explained to the lack of any covalent linkage of SNP to the polymer. The SNPs are not used as reinforcing materials but as an antimicrobial agent to treat peri- and post-operative infection during wound healing. Thus the tradeoff in mechanical properties versus antimicrobial functionality is seen with inclusion of SNP. The $E_{elastic}$ value of no SNP bioscaffold (3.47 ± 1.6 MPa) can be compared to the previously published value of 5%wt PLLA scaffold fabricated with a similar technique [30].

Table 2.1: Ultimate compressive stress , Young's Modulus ($E_{elastic}$), compressive stress at 10% strain (σ_{10}) and average Tangent Modulus values of bioscaffolds. The vales are derived from the stress-strain curves of bioscaffolds compressed perpendicular to the axis of precipitation.

Sample	Compressive Stress (kPa)	$E_{elastic}$ (MPa)	σ_{10} (kPa)	Average Tangent Modulus (MPa)
No SNP	64.5 ± 26.5	3.47 ± 1.6	3.0 ± 0.8	0.14 ± 0.01
100 ppb	48.5 ± 8.98	1.2 ± 0.3	4.2 ± 1.5	0.17 ± 0.06
700 ppm	34.95 ± 4.1	0.79 ± 0.1	4.67 ± 0.9	0.16 ± 0.01
1000 ppm	61.7 ± 9.8	1.6 ± 0.36	4.4 ± 1.0	0.24 ± 0.03
2000 ppm	39.9 ± 1.4	0.95 ± 0.3	2.7 ± 1.0	0.35 ± 0.08

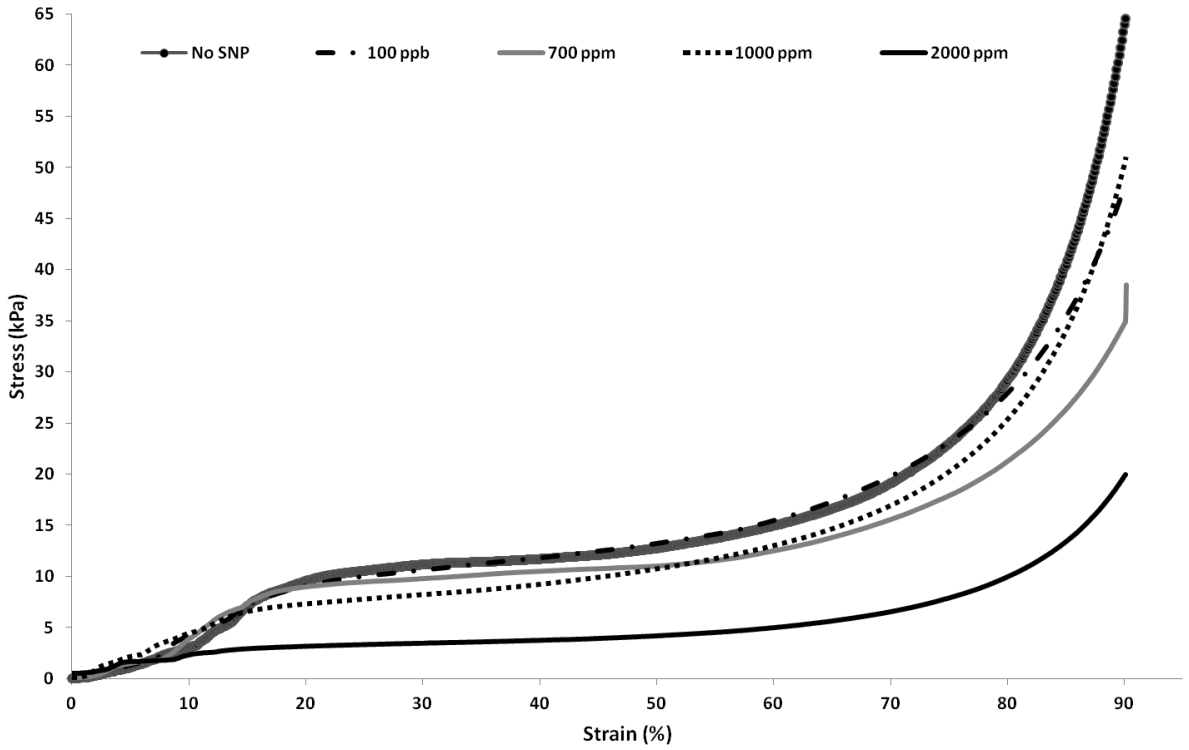

Figure 2.3. Stress-Strain graph of PLLA:PEG bioscafolds with varying concentrations of SNP. The average stress and strain values are plotted to compare the mechanical strengths of bioscaffolds by adding SNPs (n=3).

2.4.4 *In vitro* Release of Silver from Bioscaffolds

The antimicrobial and cytotoxic activity of the coatings is closely related to the rate of silver ion release from the bioscaffolds. The amount of released silver ions with respect to PBS is quantified by ICP-OES and the results are shown in Fig. 2.4. For 1000 ppm and 900 ppm bioscaffolds the concentration of silver in PBS increased from 156 ± 26 ppb to 269 ± 8.9 ppb and 82 ± 8.5 ppb to 190 ± 6 ppb respectively over the period of 5 days. The same trend was followed by a 700 ppm bioscaffold where the concentration increased from 114 ± 55 ppb to 143 ± 7 ppb while the concentration of silver ion released by the remaining bioscaffolds with lower silver concentration was nominal. The daily increment in the total amount of SNP released from No SNP, 900 ppm and 1000 ppm bioscaffold is statistically significant ($p < 0.05$; one sample t-test).

These results offer explanation to the bacterial reduction shown in Figure 2.2 (A) and (B) as silver ions released from the bioscaffolds act as an effective antimicrobial agent against *E.coli* and *S.aureus*. When compared to silver zeolites and silver containing bioglass containing scaffolds, the silver ions from the SNP in this formulation are more bio-available resulting in greater antimicrobial activity with lower concentrations of total silver.

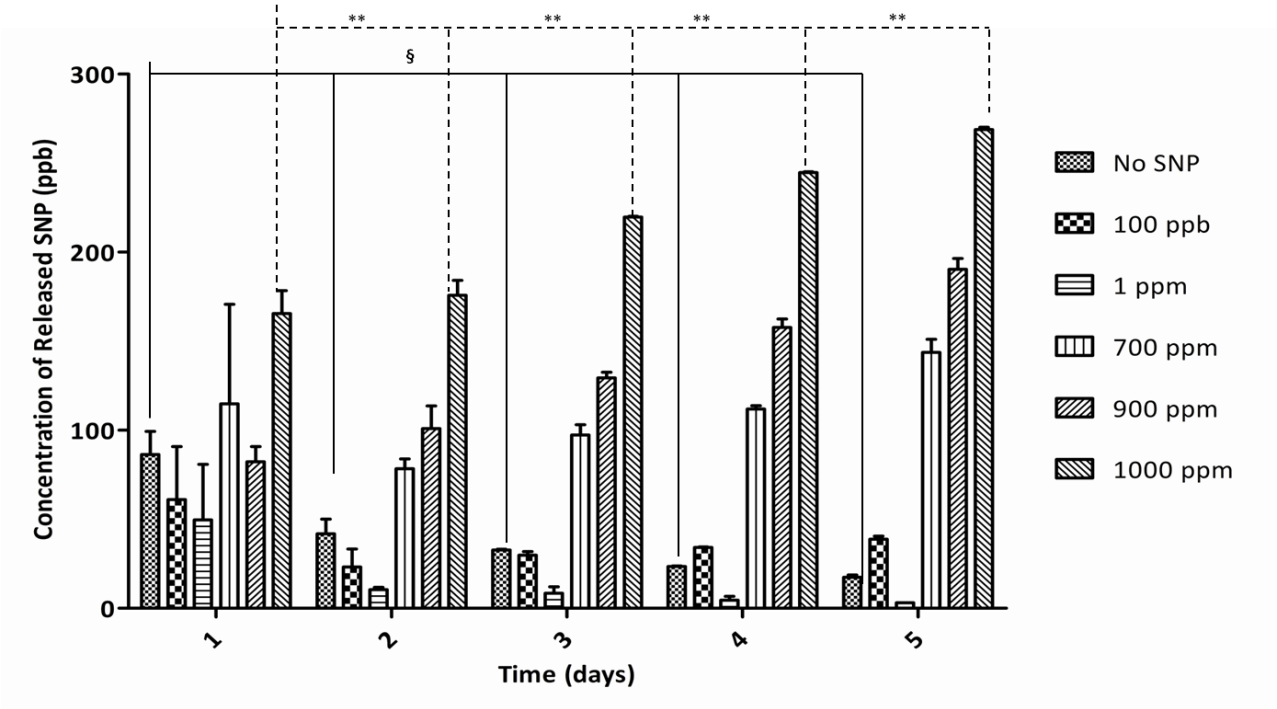

Figure 2.4. Silver release from the PLLA:PEG bioscaffolds over a period of 5 days as measured by ICP-OES. The average concentration of SNP from each bioscaffold is graphed above with bars representing the range of measured values. § and **The daily increment in the amount of SNP released from No SNP and 1000 ppm bioscaffolds respectively is statistically significant over a period of 5 days ($p < 0.05$; one sample t-test).

2.4.5 Cytotoxicity of Extracted Materials

The extract containing the released SNPs and the hydrolyzed products of PLLA were non-cytototoxic to hASC as evidenced by MTT results (Fig. 2.5). The absorbance of the stromal media is subtracted from each value as background for MTT analysis. The absorbance trends over 1, 5 and 20 days increase significantly over time for every sample ($p < 0.05$; one sample t-

test) indicating cell growth on all bioscaffolds and that the released products are below the cytotoxic thresholds for hASC. Also, the absorbance value of every bioscaffold is not statistically significant ($p > 0.05$; two-way ANOVA with Bonferroni post tests) from its respective no SNP control sample indicating that the growth of hASCs is comparatively maintained for that time point on the scaffold. With 2000 ppm bioscaffolds maintaining a comparable absorbance reading to no SNP sample, the results indicate that hydrolysis products of PLLA and the released SNP and ionic silver are largely non-cytotoxic to hASC over a range of therapeutically relevant concentrations.

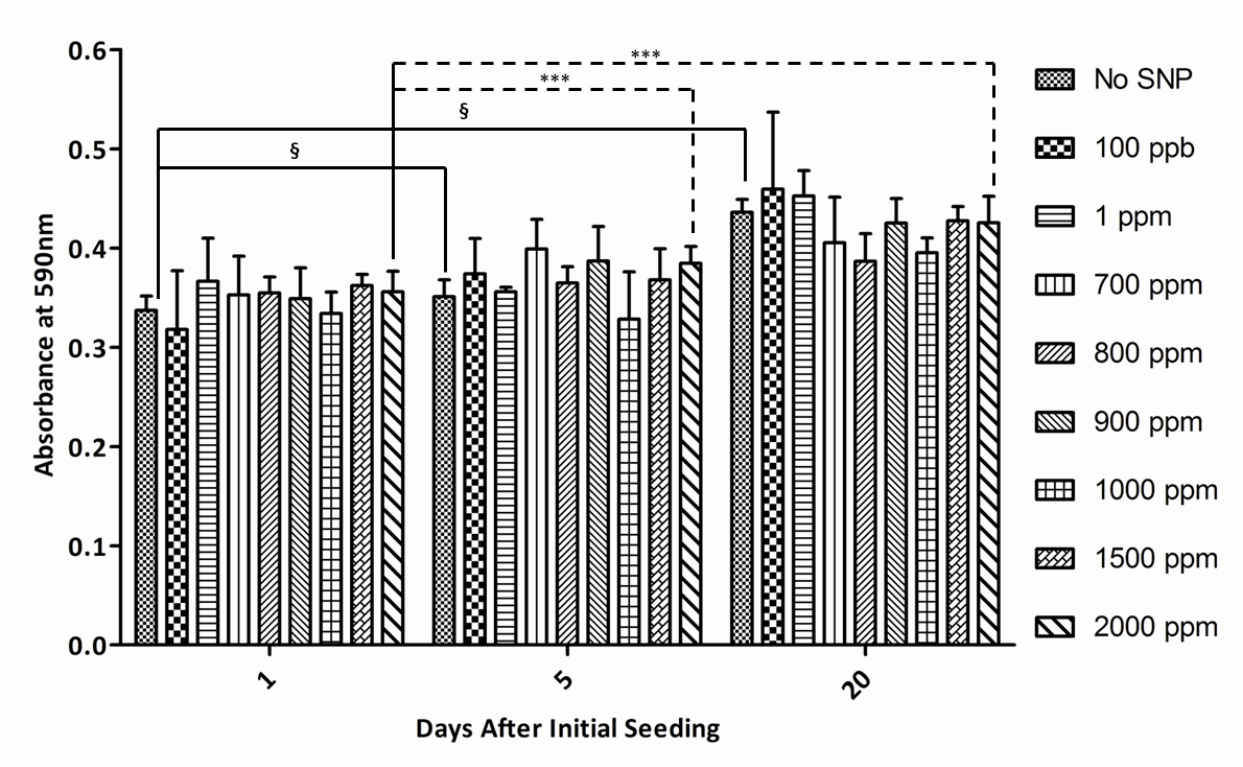

Figure 2.5. MTT absorbance measuring the viability of hASC when exposed to the media extract collected at 1, 5 and 20 days after initial cell seeding (n=3). The viability of hASCs from bioscaffold of every SNP concentration is not statistically insignificant difference from respective No SNP control samples ($p > 0.05$; two-way ANOVA with Bonferroni post tests). § The growth of hASC cell control is statistically significant difference over 20 days ($p< 0.05$; one sample t-test), *** The growth of hASC on 2000 ppm bioscaffold is statistically significant difference over 20 days ($p< 0.05$; one sample t-test).

2.4.6 Growth of hASC on Bioscaffolds

The growth of hASC was supported by PLLA:PEG SNP-bioscaffolds over a period of 20 days after initial seeding. The varying amount of SNP was not cytotoxic to hASC as growth of cells continued throughout the period of the experiment. The results were confirmed by alamarBlue® fluorescence and SEM images shown in Figure 2.6. SEM images of low (100 ppb and 1 ppm) and high (1000 ppm -2000 ppm) concentrations of SNP containing discs had extra cellular matrix on their surface 20 days after initial seeding, as seen in Figure 2.6 (A) - (F). This proves that the amount of SNP in the discs is non-cytotoxic to cells at all concentrations. These visual results were reinforced by the fluorescence data shown in Figure 2.6 (G). The fluorescence values were increased from day 5 to 20 days across all the concentrations of SNP ($p < 0.05$; one sample t-test) indicating the increment in the metabolic activity of the cells on the surface modified bioscaffold discs. Similar plasma treatments of scaffolds have also resulted in enhanced growth of stem cells [31]. The hASCs are maintained at every SNP doped bioscaffolds shown by statistically significant fluorescence value ($p > 0.05$; two-way ANOVA with Bonferroni post tests) compared to its respective cell only control sample. The inclusion of SNPs at these concentrations does not appear to have any adverse effects on the growth as shown by these results. These data also agree with similar reports where PLLA scaffolds were used to promote and aid the growth of stem cells [32, 33]. In summary, the 2000 ppm SNP-bioscaffolds achieved 99.9% and 98.85% bacterial reduction after 24 hrs of bacterial inoculation while supporting growth of hASC for 20 days. The *in vitro* released silver ions at the levels tested were non cytotoxic to hASC.

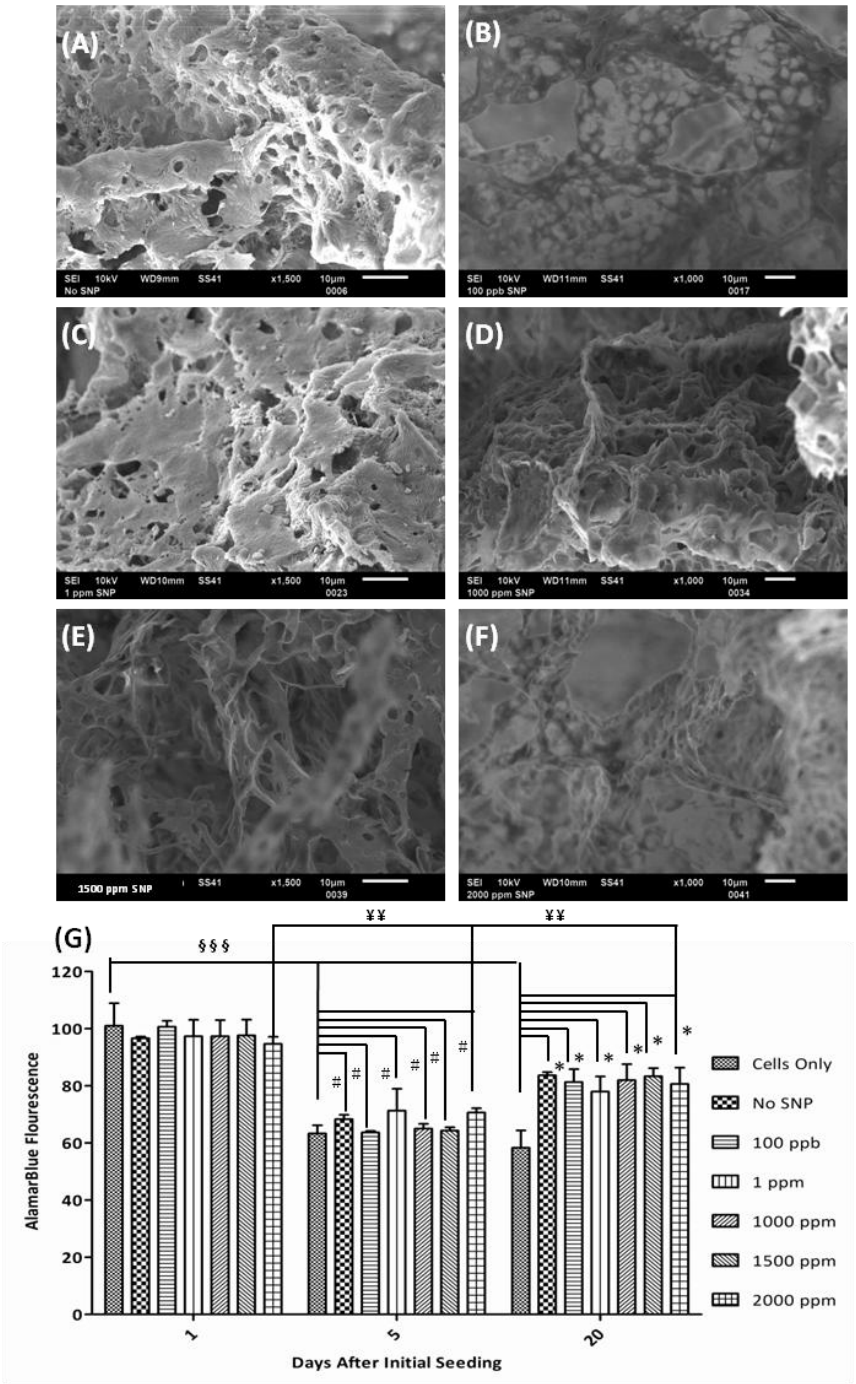

Figure 2.6. SEM images of hASC, 20 days after initial seeding, on bioscaffolds with varying concentrations of SNP; (A) No SNP, (B) 100 ppb, (C) 1 ppm , (D) 1000 ppm, (E) 1500 ppm and (F) 2000 ppm. The fluorescence measurement of alamarBlue are plotted in graph (G). * statistically significant difference compared to cells only at day 20 ($p < 0.01$; two-way ANOVA with Bonferroni post tests). # statistically insignificant difference compared to cells only at day 5. § § § The growth of hASC cell control is statistically significant difference over 20 days ($p< 0.05$; one sample t-test), ¥¥ The growth of hASC on 2000 ppm bioscaffold is statistically significant difference over 20 days ($p< 0.05$; one sample t-test).

2.5 Conclusions

Reducing or preventing antibiotic resistance of microorganisms is one of the prime objectives of researchers in trauma surgery to avoid infection and delayed wound healing. Herein, two main techniques have been discussed to synthesize SNP containing PLLA: PEG polymer scaffolds formed via a directional cryoprecipitation process, and the release of entrapped SNPs to onsite bacteria, while concomitantly supporting the growth of hASC. Either of these individual functionalities has significant biomedical applications, whereas their combination has implications for surgery, where all are desired. The results demonstrate that the SNP were uniformly distributed in the scaffolds, leading to silver ion release that inhibited the proliferation of *S.aureus* and *E.coli* by 98.85% and 99.9% respectively for the 2000 ppm case. The bioscaffolds and its extract were non cytotoxic to hASC *in vitro* and supported the growth of cells for 20 days after intial seeding. The bioscaffolds in this formulation have lower ultimate compressive stress compared to other commercially available antibiotics injected polymers but the improved antimicrobial efficacy makes them a promising candidate to be used as fillers for bone or soft tissue defects.

2.6 References

1. Khatod, M., et al., *Outcomes in Open Tibia Fractures: Relationship between Delay in Treatment and Infection.* The Journal of Trauma: Injury, Infection, and Critical Care, 2003. **55**(5): p. 949.

2. Yun, H.C., J.G. Branstetter, and C.K. Murray, *Osteomyelitis in military personnel wounded in Iraq and Afghanistan.* Journal of Trauma-Injury Infection and Critical Care, 2008. **64**(2): p. S163-S168.

3. Bhattacharyya, T., R. Iorio, and W. Healy, *Rate of and risk factors for acute inpatient mortality after orthopaedic surgery*, 2002, JBJS. p. 562-572.

4. Pederson, W.C. and D.W. Person, *Long bone reconstruction with vascularized bone grafts.* Orthopedic Clinics of North America, 2007. **38**(1): p. 23-+.

5. Punyani, S., S. Deb, and H. Singh, *Contact killing antimicrobial acrylic bone cements: preparation and characterization.* Journal of Biomaterials Science-Polymer Edition, 2007. **18**(2): p. 131-145.

6. Neut, D., et al., *Antimicrobial efficacy of gentamicin-loaded acrylic bone cements with fusidic acid or clindamycin added.* Journal of Orthopaedic Research, 2006. **24**(2): p. 291-299.

7. Borenstein, J.T., *Comprehensive Microsystem*, ed. O.T. Yogesh B Gianchandani, Hans Zappe. Vol. 2. 2008, Amsterdam: Elsevier.

8. Vacanti, J.P. and R. Langer, *Tissue engineering: the design and fabrication of living replacement devices for surgical reconstruction and transplantation.* Lancet, 1999. **354**: p. SI32-SI34.

9. Yang S, L.K.F., Du Z, Chua C K, *The design of scaffolds for use in tissue engineering. Part I. Traditional factors.* Tissue Engineering, 2001. **7**: p. 679–89.

10. Agrawal, C.M., K.A. Athanasiou, and J.D. Heckman, *Biodegradable PLA-PGA polymers for tissue engineering in orthopaedics*, in *Porous Materials for Tissue Engineering*1997, Transtec Publications Ltd: Zurich-Uetikon. p. 115-128.

11. McKnight, N.L. and J.A. Frangos, *Strain rate mechanotransduction in aligned human vascular smooth muscle cells.* Annals of Biomedical Engineering, 2003. **31**(3): p. 239-249.

12. Li M, G.J.D., Green H, Mills D K, McShane M J, Gale B K. *Effect of high-aspect-ratio microstructures on cell growth and attachment*. in *Proc.1st Annu. Int. IEEE-EMBS Spec. Top. Conf. Microtechnologies in Medicine and Biology*. 2000. Lyon, France.

13. Hollister, S., *Porous scaffold design for tissue engineering.* Nature Materials, 2005. **4**(7): p. 518-524.

14. Middleton, J. and A. Tipton, *Synthetic biodegradable polymers as orthopedic devices.* Biomaterials, 2000. **21**(23): p. 2335-2346.

15. da Cruz, A., et al., *Evaluation of physical–chemical properties and biocompatibility of a microrough and smooth bioactive glass particles.* Journal of Materials Science: Materials in Medicine, 2008. **19**(8): p. 2809-2817.

16. Bergsma, J., et al., *Biocompatibility of intraosseously implanted predegraded poly (lactide): an animal study.* Journal of Materials Science: Materials in Medicine, 1996. **7**(1): p. 1-7.

17. Schwach, G. and M. Vert, *In vitro and in vivo degradation of lactic acid-based interference screws used in cruciate ligament reconstruction.* International Journal of Biological Macromolecules, 1999. **25**(1-3): p. 283-291.

18. Suuronen, R., et al., *A 5-year in vitro and in vivo study of the biodegradation of polylactide plates.* Journal of Oral and Maxillofacial Surgery, 1998. **56**(5): p. 604-614.

19. Hall, J. and A. Sachdev, *Particle size, volume fraction and matrix strength effects on fatigue behavior and particle fracture in 2124 aluminum-SiCp composites.* 1994.

20. Silva, G.A., et al., *Materials in particulate form for tissue engineering. 2. Applications in bone.* Journal of Tissue Engineering and Regenerative Medicine, 2007. **1**(2): p. 97-109.

21. Yu, G., et al., *Yield and characterization of subcutaneous human adipose-derived stem cells by flow cytometric and adipogenic mRNA analyses.* Cytotherapy, 2010. **12**(4): p. 538-546.

22. Qureshi, A.T., et al., *Biocompatible/Bioabsorbable Silver Nanocomposite Coatings.* Journal of Applied Polymer Science. **120**(5): p. 3042-3053.

23. Zhang, H.F., et al., *Aligned two- and three-dimensional structures by directional freezing of polymers and nanoparticles.* Nature Materials, 2005. **4**(10): p. 787-793.

24. Pamula, E., et al., *The influence of pore size on colonization of poly(L-lactide-glycolide) scaffolds with human osteoblast-like MG 63 cells in vitro.* Journal of Materials Science-Materials in Medicine, 2008. **19**(1): p. 425-435.

25. Moumile, K., et al., *Descriptive study of bacteremia in a geriatric hospital.* Pathologie Biologie, 2004. **52**(10): p. 557-565.

26. Soscia, D.A., et al., *Antibiotic-Loaded PLGA Nanofibers for Wound Healing Applications.* Advanced Engineering Materials. **12**(4): p. B83-B88.

27. Moojen, D.J.F., et al., *No Efficacy of Silver Bone Cement in the Prevention of Methicillin-Sensitive Staphylococcal Infections in a Rabbit Contaminated Implant Red Model.* Journal of Orthopaedic Research, 2009. **27**(8): p. 1002-1007.

28. Olgun, U., K. Tunc, and V. Ozaslan, *Preparation of antimicrobial polycaprolactone-silica composite films with nanosilver rods and triclosan using roll-milling method.* Polymers for Advanced Technologies. **22**(2): p. 232-236.

29. Wan, Y., et al., *Preparation and mechanical properties of poly(chitosan-g-DL-lactic acid) fibrous mesh scaffolds.* Polymers for Advanced Technologies, 2008. **19**(2): p. 114-123.

30. Budyanto, L., Y.Q. Goh, and C.P. Ooi, *Fabrication of porous poly(L-lactide) (PLLA) scaffolds for tissue engineering using liquid-liquid phase separation and freeze extraction.* Journal of Materials Science-Materials in Medicine, 2009. **20**(1): p. 105-111.

31. Hanson, A.D., et al., *Effects of oxygen plasma treatment on adipose-derived human mesenchymal stem cell adherence to poly(L-lactic acid) scaffolds.* Journal of Biomaterials Science-Polymer Edition, 2007. **18**(11): p. 1387-1400.

32. McCullen, S.D., et al., *Electrospun composite poly(L-lactic acid)/tricalcium phosphate scaffolds induce proliferation and osteogenic differentiation of human adipose-derived stem cells.* Biomedical Materials, 2009. **4**(3): p. 9.

33. Mauney, J.R., et al., *Engineering adipose-like tissue in vitro and in vivo utilizing human bone marrow and adipose-derived mesenchymal stem cells with silk fibroin 3D scaffolds.* Biomaterials, 2007. **28**(35): p. 5280-5290.

Chapter 3. miR-148b-Nanoparticle Conjugates for Light Mediated Osteogenesis of Human Adipose Stem Cells[2]

3.1 Project Summary

Delivery systems providing spatial and temporal control have the potential to improve outcomes in surgical reconstruction and regenerative medicine by precise modulation of wound healing and tissue repair processes. In this study we describe a synthesis and oligonucleotide functionalization process of silver nanoparticle complexes for photo-activated microRNA (miRNA) delivery. The activity of the PC-miR-148b-SNP construct is demonstrated by light mediated delivery of miR-148b mimic resulting in differentiation of human autologous adipose derived mesenchymal stromal/stem cells (hASCs) into a osteogenic linage. The conjugate, upon photoactivation, increases alkaline phosphatase (ALP) activity in the cell membrane and calcification (mineralization) of hASCs on day 7 and 14 respectively. Additionally, the expression of mRNA for the early, middle and late stage osteogenic markers; ALP, RunX2 and osteocalcin (OCN) respectively, were also significantly upregulated at day 7 and 28, respectively after photoactivation of PC-miR-148b-SNP and release of miR-148b mimics. Additionally, PC-miR-148b-SNP conjugate is readily delivered to the intracellular compartment without the use of transfection vectors commonly required for free oligonucleotides. This technology demonstrates photo-controlled, spatial and temporal modulation of osteogenesis in hASCs.

3.2 Introduction

Modulation of gene expression with miRNA is a promising technique to improve control of wound healing and tissue repair processes.[1] These short, non-coding RNA's are involved in post-transcriptional regulation pathways and in their mature form are found as single strands often associated with RNA silencing complexes.[2] MicroRNAs with the potential to modulate

[2] Reprinted with the permission of Journal of Biomaterials. (Appendix B)

differentiation and wound healing, utilized in conjunction with autologous, adipose derived mesenchymal stromal/stem cells (ASCs) are an attractive therapeutic modality for regenerative medicine. Directing the osteogenic differentiation of ASCs is of particular interest in the design of therapies for critical size bone defects, spinal fusion and skeletal reconstruction. In a previous study, by Schoolmeester *et al*., miR-148b was shown to induce de novo increases in total ALP activity, an early biomarker of osteogenesis in bone marrow-derived mesenchymal stem cells.[3] Technology developments that provide spatial and temporal control of miRNA delivery and activity would improve the clinical relevance of miRNA therapies, but to date, this remains a challenge. Of particular interest is the development of delivery vehicles capable of activation by a non-invasive trigger such as light or ultrasound stimulation [4-6].

Studies on metallic nanoparticles (NPs) have emphasized the benefits of using noble metal nanoparticles in delivery applications including ease of bulk synthesis, readily tunable morphology, large surface area-to-volume ratios and robust functionalization chemistries. [7]. Clinically, SNPs have been used as effective antimicrobial solutions in wound care. Recent *in vivo* studies have provided positive safety assessments for systemic exposure thus encouraging its used in biomedical research [8-11]. A 2008 animal study revealed minimal induction of secondary markers of liver damage even in the presence of chronic oral SNP doses greater than 300 mg/kg/day for 28 days[12]. Reduced side-effects of administered SNPs at ‘moderate’ doses[13] may lend greater confidence in the suitability of SNPs for *in vivo* biomedical solutions considering studies that seek to lower the threshold of ‘effective’ SNP doses by harnessing their large drug payload capabilities and electromagnetic field amplifying characteristics. These advantageous properties have allowed NPs to be used in the delivery of various therapeutic agents including small molecules [14, 15], antisense oligonucleotides [16, 17], and siRNAs. [18-

20] Additionally, metal nanoparticles fulfill the core requirements as drug delivery vehicles by offering high-density surface ligand attachment, facile transmembrane delivery [17], reduced degradation of therapeutic payload nucleic acids [18, 21-25], and potentially controlled intracellular release.[25]

Several attempts have been made to release nucleic acids from surfaces (including nanoparticles) via thermal [5], pH [26], ionic strength, and chemical stimuli [27] but greater control of spatial selectivity can potentially be achieved with photo-activated delivery systems. Photocleavable groups, such as nitrophenylethyl (NPE), have been used to cage various biomolecules, including nucleotides, proteins, and nucleic acids [28-30] for in situ photo-activation. Based on these previous studies it is expected that photo-activation via irradiation will allow rapid spatially and temporally defined release of a miRNA within a specific intracellular compartment.

Silver nanoparticles (SNP) have unique optical properties including a localized surface plasmon field that is ~10 times greater to that of similarly sized gold nanoparticle.[31] These optical properties have increased interest in their use as sensors[32, 33], biological labels[31], substrates for surface-enhanced absorption, fluorescence[34], and photochemistry.[35, 36] SNP also offer higher extinction coefficients and blue-shifted plasmon resonant peaks compared to many other metallic nanomaterials[31, 37], taken together this indicates that SNPs may be an appropriate alternative for photo-controlled drug delivery using caged compounds such as nitrobenzyl derivatives.

Herein we describe the synthesis, characterization and *in vitro* function of a light activated, miRNA delivery particle that may serve as a potential solution for the repair of critical sized skeletal defects by providing greater temporal and spatial control over stem cell

differentiation. The light activated technology described in this study links a truncated single stranded microRNA148b mimic to silver nanoparticle surface via a photocleavable (PC) linker providing for the release and activation of miRNA from the particle by a discrete photo-trigger. The facile in-place exchange strategy for the synthesis of SNP based light activated miRNA delivery system is described and the resulting construct called PC-miR-148b-SNP is characterized by light scattering, electron microscopy, UV-Vis spectroscopy, optical emission spectroscopy and fluorometry. The osteogenic differentiation of human adipose derived mesenchymal stromal/stem cells by miR-148b is demonstrated and further characterized *in vitro*. Uptake and intracellular trafficking of the PC-miR-148b-SNP construct is observed and photo-triggered release of micro RNA is quantified. Finally photo-triggered restoration of miRNA activity from the PC-miR-148b construct is demonstrated by light modulated hASCs osteogenic differentiation *in vitro* and compared to standard cationic transfection agents.

3.3 Materials and Methods

3.3.1. Materials

HPC-SNPs were synthesized as described by Qureshi et al[9]. Silver surfaces were functionalized with custom thiol-modified oligonucleotides ordered from TriLink Bio Technologies (San Diego, CA). 2M Tris-NaCl buffer (pH 8.0) was made up from Biotechnology grade Tris (Amresco Inc, Solon, OH) and sodium chloride (Fischer Scientific, Pittsburgh, PA). Dithiothreitol (1M aqueous) and TRI Reagent were purchased from Sigma (St. Louis, MO).

3.3.2 Cell Culture

Liposuction aspirates from subcutaneous adipose tissue were obtained from three female (Age: 20- 45 yrs and BMI= <30) subjects undergoing elective procedures. All tissues were obtained with informed consent under a clinical protocol reviewed and approved by the Institutional

Review Board at the Pennington Biomedical Research Center (#23040). Isolation of hASC was performed as described elsewhere [38]. Human ASCs were maintained in 25cm^2 flasks (BD Falcon) in stromal culture medium (SM) at 37^{o}C and 5% CO_2 in a humidified atmosphere. SM is composed of Dulbecco's minimal essential medium (DMEM):Ham's F-12 (1:1), 2.5mm L-glutamine, 15mm HEPES supplemented with 10% fetal bovine serum (FBS) and 1% antibiotic solution (100x with penicillin, streptomycin, fungizone) until 80–90% confluent. Freshly isolated hASC were cyropreserved at Passage 0 abd thawed for subsequent use at Passage 2 for each individual donor used for all *in vitro* experiments.

3.3.3 Osteoinductive Induction

To evaluate the ability of miR-148b to modulate osteogenesis, approximately 1x10^5 hASCs were seeded in 48-well tissue culture plate (BD Falcon, Franklin Lakes, NJ). Cells were allowed to incubate for 24hr in SM at 37°C prior to PC-miR-148b-SNP construct treatment. 10 ul of 70 ppm HPC-SNPs and 10 ul of PC-miR148b-SNP construct (227.2 ± 1.7 ppm SNP and 40 nM PC-miR-148b) were added to cells for 16 hr before photo-release. For photo-release, the PC-miR148b-SNP treated cells were photo-activated for 5 min at 365nm (52.4 J/cm^2) by means of a GreenSpot system (American Ultraviolet, Lebanon, IN), which incorporates a 100–watt, pressurized mercury lamp with 5mm x 1000mm light guide, and produces a peak spectral output at 365nm (American Ultraviolet, Lebanon, IN). The lamp has a fluence of 206 mW/cm2 with the short bandpass (1.5mm thick, 2.4mm diameter SWP–2502U–400, Lambda Research Optics, CA) and IR filters (818–ST–UV detector, Newport Corporation, Irvine, CA) in place. The test groups included hASCs maintained in OM and cells transfected with single stranded 22 nt miR-148 by TurboFect (Table 1). The Control groups included hASCs maintained in SM, cells transfected with single stranded miSpike-21mer by TurboFect (universal control). The TurboFect

transfection was conducted according to manufacturer's protocol. Other controls include photo-exposed hASCs and cells transfected with PC-miR148b mimic. The initial media was exchange was performed 48 hr post photo release (64 hr post treatment) and the cells were maintained for either 7, 14 or 21 days while exchanging media every 3 days. Table 1 shows the sequence of miRNAs used in this study and the placement of 2'-O-methyl protection of nucleotides.

3.3.4 Silver Nanoparticle Functionalization

Silver nanoparticles were functionalized via a modified 'salt-aging' technique. Custom thiol and photo-cleavable group-modified, 6-TAMRA-labeled oligonucleotides (PC-miR-148b) were mixed with HPC-SNP (70pM) at a oligo-to-particle stoichiometry of 5000:1, and left to incubate at 37°C under gentle rocking conditions to favor initial oligonucleotide. Following a 24hr incubation period, a 48hr Tris-buffer based salt-aging process was commenced during which the SNP-oligo conjugate solution was first rapidly adjusted to 1% SDS and 25mM phosphate buffer, and subsequently slowly (1x 5ul aliquot additions of a 1M Tris-NaCl buffer per 24hrs) adjusted to 20mM NaCl and 10mM Tris buffer (pH 8.0) concentration. Functionalized nanoparticles were purified via centrifugation (3 x 7000 RPM) and resuspended in a modified buffer (1% SDS, 50mM Tris-NaCl) prior to experimental analysis.

3.3.5 SNP and Conjugate Characterization

For UV-Visible spectroscopic characterization, naked and PC-miR-148b functionalized SNPs were diluted to appropriate concentrations in DI water. Diluted samples were analyzed for absorption properties in a wavelength range scan (200-700nm). For TEM characterization, 5 ul of SNP solution and 5ul PC-miR-148b functionalized SNP) conjugate solution were pipetted on Carbon/Copper 20-30 nm grids (EMS, Hatfield, PA), air dried and visualized with JEOL 100CX.

The changes in electrical potential across the double layer were also measured with dynamic light scattering (DLS).

3.3.6 PC-miR-148b Coverage Quantification

PC-miR-148b coverage on functionalized SNP-conjugates was quantified via fluorescence-based measurements of particle-released oligonucleotide samples. Following PC-miR-148b-SNP functionalization and purification, the oligonucleotide was cleaved from the SNPs via two methods; 1) 1% dithiothreitol (DTT) was added to SNP-conjugate solutions and allowed to shake at 37 °C for 10-15min and 2) 1ml of prepared PC-miR-148b-SNP conjugates were loaded in a demountable quartz cuvette chamber (5mm path length, 49-Q-5, Starna Cells Inc, Atascadero, CA) and irradiated at 365nm by means of a GreenSpot. After treating the samples with either DTT or 365nm radiation, the samples were centrifuged (1 x 7000 RPM). The supernatant (PC-miR-148b) was quantified via fluorimetry with Wallac VICTOR2 V 1420-040 Multilabel Counter (Perkin-Elmer, Boston, MA, USA) at excitation/emission lines set at 531/572nm. A standard curve depicting the fluorescence of varying concentration of PC-miR-148b was plotted to calculate the amount of oligonucleotide on the particles. The silver content of HPC-SNPs pellet was quantified via inductively coupled plasma optical emission spectrometry (ICP-OES) (Varian, Palo Alto, CA, USA). Particle sizes estimated from TEM, in conjunction with silver content, were used to calculate total particle numbers according to the previously published method[39, 40].

3.3.7 Histochemical Staining

ALP histochemistry was performed on hASCs exposed to different treatments at day 7. The ALP up-regulation was qualitatively and quantitatively measured by Millipore kits, SCR 004 and SCR 066 respectively according to manufacturer's instructions. Briefly, hASCs were

fixed with 4% formaldehyde in Dulbecco's Phosphate-Buffered Saline (DPBS) for 1-2 min and then rinsed DPBS. The cells are then stained with Fast Red Violet solution and Napthol AS-BI phosphate solution before imaging the cells with color camera mounted on Olympus cell TIRF illuminator light microscope. For quantitative measurement, $2x10^4$ cells were isolated from each sample and reacted with p-nitrophenylphosphate (p-NPP) substrate provided in the kit. The absorbance of p-nitrophenol was measured at 405 nm with Wallac VICTOR2 V 1420-040 Multilabel Counter and normalized to number of hASCs, measured by PicoGreen (Life Technologies, Eugene, OR) at 7 days[41, 42].

For Alizarin Red histochemistry, the cultured cells were stained on day 14 for assessing the mineralized matrix. The media was removed, and the cell layers were rinsed with DPBS before staining with 2% Alizarin Red (2g/100mL DI water, pH adjusted to 4.1 by adding 10% ammonium hydroxide) for 10 min. The cells are then washed with DPBS six times before imaging on Olympus cell TIRF illuminator light microscope. To quantify the mineralization of hASCs with photoactivated PC-miR148b-SNP the cells were destained by the addition of 400 ml of 10% cetylpyridinium chloride monohydrate to each well followed by shaking for 10 min at room temperature. The calcium deposition expressed by the optical density of the aliquots was then measured at 540 nm with a plate reader and normalized to number of hASCs, measured by PicoGreen (Life Technologies, Eugene, OR) at 14 days [41, 42].

3.3.8 Quantitative Real Time Polymerase Chain Reaction (Q-PCR)

Total RNA was extracted from injected/transfected hASCs with Tri Reagent according to the manufacturer's instructions. The extracted RNA was then used to perform Q-PCR with iScript™ One-Step RT-PCR Kit with SYBR® Green using MiniOpticon™ Real-Time PCR Detection System (Bio-Rad Laboratories, Hercules, CA). The sequences of PCR primers

(forward and backward, 50 to 30) used to assess the osteogenic differentiation of hASCs with nanoparticles were as follows: ALPL, 5'- AATATGCCCTGGAGCTTCAGAA -3' and 5'-CCATCCCATCTCCCAGGAA -3'; osteocalcin (OCN), 5'- GCCCAGCGGTGCAGAGT -3' and 5'- TAGCGCCTGGGTCTCTTCAC -3'and Runx2; 5'-GCAAGGTTCAACGATCTGAGATT- 3' and 5'- AGACGGTTATGGTCAAGGTGAAA- 3'. Samples were normalized (ΔCt) against the house keeping gene 18SrRNA and -ΔΔCt value of ALPL, OCN and Runx2 in hASCs, relative to SM, was calculated using the ΔΔCt method[43].

3.3.9 *In vitro* Photo-release of PC-miR-148b

Confocal microscopy was used to monitor *in vitro* photo-release of PC-mir-148b from the conjugate. hASCs were seeded in 1.0 Borosilicate cover glass Lab-Tek™ 4-well chambered slides (Thermo Fisher Scientific, Rochester, NY) and treated with PC-miR-148b-SNP conjugates as described in section 2.3. To calculate the co-localization coefficient and better visualize the intracellular distribution of PC-mir-148b-SNP and activated constructs, 100 ul of 227.2 ± 1.7 ppm PC-miR-148b-SNP was injected to hASCs. Similarly cells were flashed for 5min at 365nm, 4hr prior to imaging (20hr post PC-miR-148b-SNP conjugate delivery). All samples were resuspended in OPTI-MEM® prior to imaging. The Leica TCS SP2 spectral confocal & multiphoton system used consists of a Leica DM IRE2 inverted microscope with a galvo-Z stage. Excitation lasers at 488 and 543nm were used in imaging experiments, concurrently with tuned emission wavelength windows. Reflectance mode images of SNPs (488/492 nm) and 6TAMRA labeled PC-miR-148b fluorescence (543nm/572 nm) were overlayed to visualize the co-localization difference between the radiated and non-radiated samples. Images were analyzed using Leica Confocal Software (LCS) Lite (Leica Microsystems Heidelberg GmbH).

3.3.10 Osteocalcin ELISA

To evaluate OCN levels in the hASCs treated with PC-miR-148-SNP (radiated and non-radiated) along with other controls mentioned in section 2.3 for 14 or 28 days. The cell media of last four days for each sample was collected and tested for OCN secretion using a commercially available kit (Life Technologies, Grand Island, NY). The media was incubated with microplate coated with osteocalcin antibody before introducing anti-osteocalcin horseradish peroxidase (HRP) conjugate. The plate was then washed, incubated with Chromogen (Tetramethylbenzidine) and stopping reagent respectively. The product was measured at 450 nm, and the amount of OCN was quantified with a standard curve and then normalized to number of hASCs measured by PicoGreen (Life Technoligies, Eugene, OR), at 14 and 28 days respectively [44].

3.3.11 Measuring Cytotoxicity of PC-miR148b-SNP with Flow Cytometry

A 1 ml cell hASCs solution ($1x10^5$ cell/ml), was plated on 48 well tssue culture plates for 24 hrs before as mentioned in section 2.3. After the photoactivation the samples were maintined in the plates for 28 days while exchanging the media every 3-4 days. For a necrotic control, hASCs were incubated for 4 hr in 75% ethanol. After treatment, adhered hASCs were harvested by trypsinization (0.25% Trypsin), washed with 1 ml D-PBS, pooled together with the detached hASCs and centrifuged at 1800 rpm to obtain cell pellet. Cells were re-suspended in 1 ml D-PBS and stained with 4 ul of 1.2 uM Sytox Red (Life Technologies, Eugene, OR) for 15 mins in the dark, then centrifuged and fixed in 250 ul of 1% paraformaldehyde (PFA) solution in PBS for flow cytometric analysis of viability with a BD FACSCalibur cytometer (Franklin Lakes, NJ). For each sample, scatter and fluorescent data was collected for 30,000 cell events

using Cellquest pro (BD Biosciences, San Jose, CA) and former analyzed using WinMDI 2.8 software (by Dr J. Trotter, Scripps Institute, La Jolla, CA).

3.3.12 Statistical Analysis

All results were expressed as mean ± % error. Data was analyzed with one way t-test. For all comparisons, a p-value < 0.05 was considered significant.

3.4 Results and Discussion

3.4.1 miR-148b and miR-148b* Osteogenic Properties of Free Oligonucleotides

In studies conducted by Schoolmeesters *et al*., the expression of miR-148b mimics were found to upregulate the activity of ALP in human, bone marrow derived MSC, de novo, without other osteogenic stimuli.[3] Initial experiments were conducted as part of this study to expand this work to hASCs and to include a late stage marker of differentiation, OCN, for a more thorough evaluation of miR-148b's osteogenic potential. Additionally, a dose response for the truncated miR-148b and miR-148b* mimic sequences was determined and the impact of strand hybridization on *ALP* and *OCN* expression was explored (Figures 3.1 and 3.2) using cationic transfection agents as a delivery vector. Post transfection ALP and Alizarin Red assays demonstrated upregulated ALP activity and greater Alizarin Red staining of hASCs transfected with miR-148b mimic compared to miR-148b* mimic (Figures 3.3 and 3.4). These results demonstrate that miR-148b and miR-148b* sub-sequences are both capable of driving the expression of common osteogenic markers hASCs.

Based on these results, a single stranded miR-148b mimic (Table 3.1) was selected for inclusion into the PC-miR-148b-SNP conjugates and used in all future experiments. Unlike mimics used by Schoolmeesters *et al*, the mimics in this study were single stranded to reduce the footprint and increase nucleic acid packing density on the particle. This has been shown to

reduce nuclease attack and oligo degradation in similar particle systems.[16, 45] A target miRNA mimic concentration of ~400nM was chosen for all experimental and control samples, and delivered concentrations are based on total oligo present on the particle rather than on estimations of released miRNA mimic. After purification 40 nM of PC-miR-148b was recovered from the SNPs irradiation.

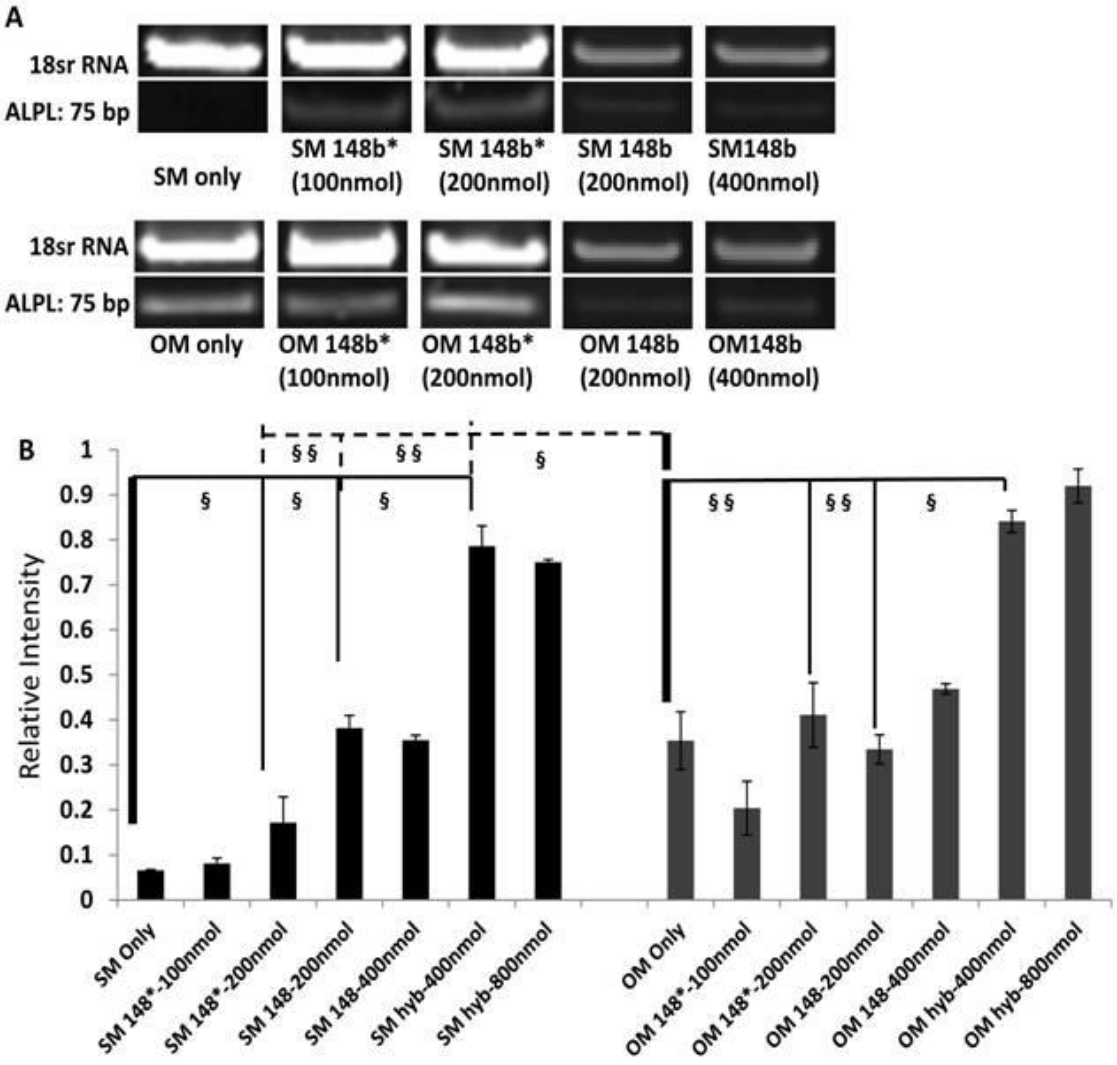

Figure 3.1: Semi-quantitative gel analysis of RT products with respect to its respective 18s rRNA band for ALPL. (A) Represents the ALPL and their 18srRNA bands while (B) show the relative ALPL intensity of each sample compared to 18srRNA internal control. § indicates difference from respective controls (SM or OM) ($p < 0.05$; two-way ANOVA with Bonferroni post tests). §§ indicates no difference from OM control ($p > 0.05$).

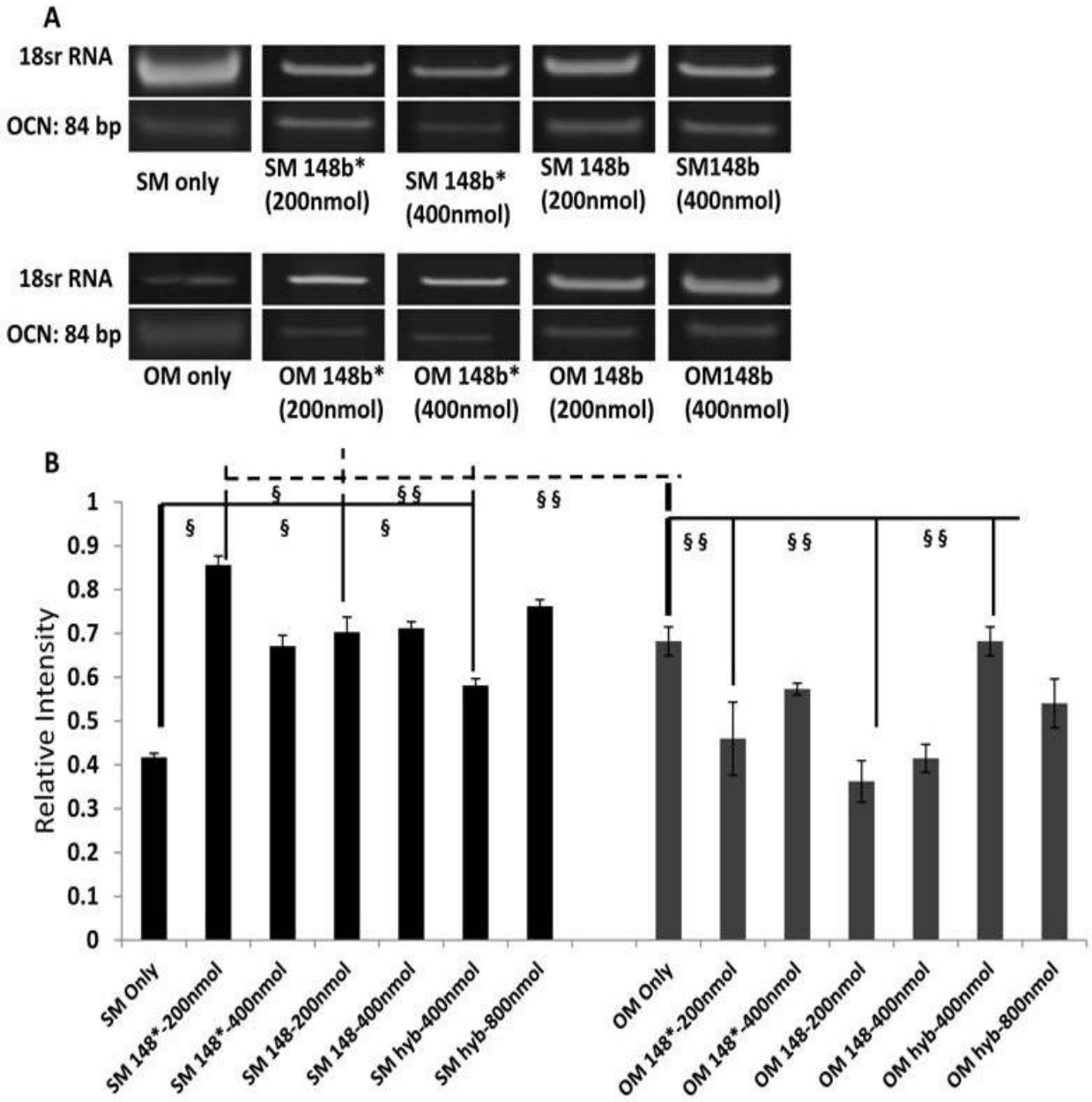

Figure 3.2. Semi-quantitative gel analysis of RT products with respect to its respective 18s rRNA band for OCN. (A) Represents the OCN and their 18srRNA bands while (B) show the relative OCN intensity of each sample compared to 18srRNA internal control. § indicates difference from respective controls (SM or OM) ($p < 0.05$; two-way ANOVA with Bonferroni post tests). §§ indicates no difference from OM control ($p > 0.05$).

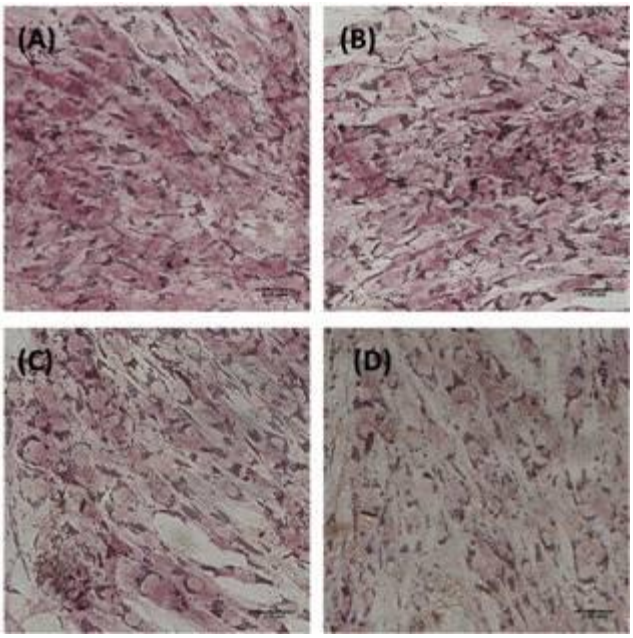

Figure 3.3: Alkaline Phosphatase (ALPL) up-regulation was qualitatively measured by Millipore kits, SCR 004 on hASCs transfected with (A) single-stranded miR-148b* in stromal media (SM), (B) hybridized miR-148b and miR-148b* in SM, (C) single-stranded miR-148b* in osteogenic media (OM) and (D) hybridized miR-148b and miR-148b* in OM. Magnification is 20x, and scale bar is 100um.

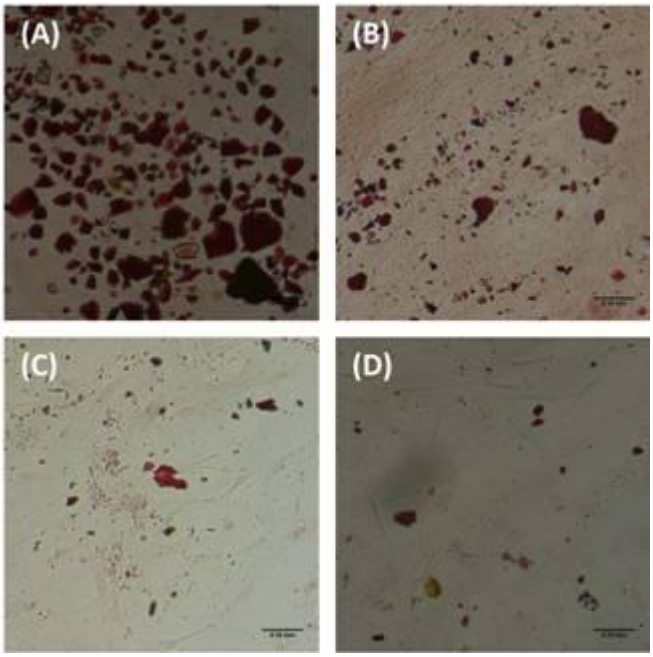

Figure 3.4: The mineralization of hASC treated with varying conditions was quantified by staining cells with Alizarin Red. The hASCs were transfected with (A) single-stranded miR-148b* in stromal media (SM), (B) hybridized miR-148b and miR-148b* in SM, (C) single-stranded miR-148b* in osteogenic media (OM) and (D) hybridized mir-148b and mir-148b* in OM. Magnification is 20x, and scale bar is 100um.

Table 3.1. Sequence of miRNA used in this study. The first three nucleotides of miSpike-21-mer, miR-148b and miR-148b* from each end the entire miRNA sequence of PC-miR148b are 2'-O-methylated.

	miRNA	Sequence
Negative Control	miSpike-21mer	5′- 2'OMe(CUC)AGGAUGGCGGAGCGG(UCU) 2'OMe -3′
miRNA tested in supplemental	miR-148b	5′-2'Ome(UCA)GUGCAUCACAGAACUU(UGU) 2'OMe-3′
Positive Control	miR-148b*	5′-2'Ome(AAG)UUCUGUUAUACACUCA(GGC) 2'OMe-3′
miRNA used in PC-miR-148b-SNP construct	PC-miR-148b	5′- (6-TAMRA) (C6-NH) 2'OMe (UCAGUGCAUCACAGAACUUUGU) (PC Spacer) T (C6-S-S-C6)-3′

3.4.2 Functionalizing HPC-SNP with PC-miR-148b

The photo-labile oligonucleotides for conjugation to SNPs surfaces were designed to optimize surface coverage, SNP-conjugate stability, and surface-enhancement of photochemical processes, including fluorescence detection and photolysis of the nitrophenylethyl (NPE) internal photocleavable linker (Figure 3.5A). Silver NPs were chosen as a platform as the optical properties and biocompatibility are well described in the literature; silver has distinct plasmon-related absorption spectra with maxima at ~420nm, which overlaps with the maxima of the NPE linker (365nm).[34, 46-49] The hydroxypropyl cellulose stabilized silver nanoparticles (HPC-SNPs) were prepared according to previously described methods and characterized via UV-Vis spectroscopy, TEM and DLS. [9]

Upon attaching PC-miR148b to silver particles to form the PC-miR-148b-SNP conjugate, a slight red-shifting of the SNPs resonance peak is observed by ~5 nm to 418 nm, (Figure 3.5B). This perturbation of the localized surface plasmon resonance (SPR) of nanoparticles is caused by changes in the dielectric environment associated with the addition of PC-miR-148b to the HPC-SNPs as predicted by Mie Theory.[50, 51] Salt aging functionalization techniques and absorption

of ligands to the SNP surface results in an increase in the dielectric constant of the local environment typically causing a red shift in the SPR absorption band.[52]

TEM analysis of HPC-SNPs and PC-miR148b functionalized SNPs (Figure 3.5 C and D) also indicates the attachment of PC-miR-148b to SNPs. PC-miR148b-SNP conjugates were observed to be partially surrounded with less dense regions attributed to adsorbed PC-miR-148b and associated salts (Figure 3.5D). These less dense regions may be affected by Joule heating from e-beam irradiation resulting in melting and deformation of crystallized salt and RNA on the particle surface. Based on the DLS measurements the size of the SNPs decreased from 85.57 ± 0.93 nm to 75.37 ± 0.83 nm with the attachment of PC-miR-148b to form PC-miR-148b-SNP conjugate, which is likely associated with the displacement of bulky HPC polymer (~80,000MW) with smaller miRNA mimic construct during the in-place exchange.

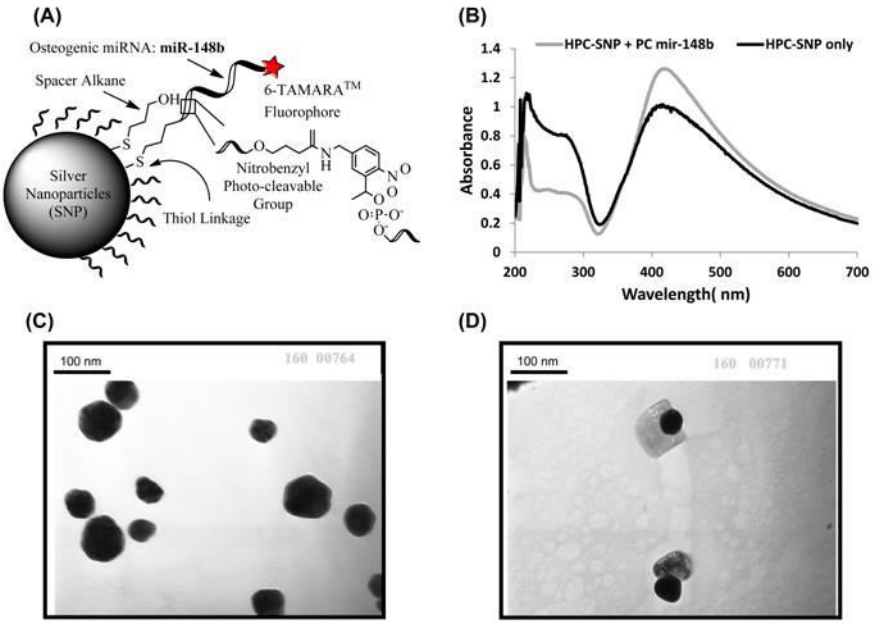

Figure 3.5. Concept and characterization of SNPs and PC-miR148b-SNP conjugates. (A) Schematic of caged oligonucleotide-functionalized SNPs (HPC-SNP+ PC-mir148b). (B) Absorbance spectra for SNPs and PC-mir148b-SNP. (C and D) TEM images of SNP and PC-mir148b-SNP respectively.

A change in zeta potential was also observed after functionalizing HPC with PC-miR-148b. The potential decreased from -6.11 ± 3.57 to -39.3 ± 6.63mV which can be attributed to displacing the HPC from the nanoparticles with negatively charged oligonucleotide (PC-miR-148b). This shift to a more negatively charged surface will likely result in greater colloidal stability in aqueous solution, as seen previously in nucleic acid functionalized particle systems.[53]

Oligonucleotide coverage on the conjugate is an important factor, as it plays a role not only in stabilizing the conjugate, but also in the efficiency of nucleic acid payload delivery, in this case, the osteogenic miR-148b mimic. The salt aging functionalization process was adapted from previously described gold functionalization methods and optimized for the protected RNA mimics used in this study.[54] In addition to determining the total miRNA-148b mimic attached to the particle, the efficiency of photo-release was determined in an effort to quantify the effective dose for hASCs differentiation. [55] The attached PC-miR-148b was removed from the conjugate either by photoactivation (365nm) or treatment with DTT. A fluorescence-based method, in conjunction with inductively coupled plasma optical emission spectroscopy, was used to calculate the coverage density and oligonucleotide footprint of PC-miR-148b. [56, 57] The miR-148b coverage density was 4.33 (±2) x 10^{16} oligos/cm^2 while the oligonucleotide footprint was 23.10 ± 20 nm^2 as determined using the concentration values derived from DTT treatment. These oligo ratio and footprint values are comparable to previously published values for similar sized gold and silver nanoparticles.[57, 58]

Photoactivation resulted in a release of oligonucleotide corresponding to 1.59 (±2) x 10^{16} oligos/cm^2, a significantly lower in value than determined by DTT treatment. These numbers correspond to PC-miR-148b/SNP ratio of 1361 ± 101.36 and 499.47 ± 47.0 oligonucleotide per

particle for DTT and UV radiation respectively. Due to the large variation in the amount of released PC-miR-148b from these two methods, we confirmed the oligonucleotide/particle ratio by treating the previously photoactivated sample with DTT to remove the remaining PC-miR-148b from SNPs, resulting in a value of 720.30 ± 69.9 oligos/particle. It appears the additional DTT treatment successfully removed the bulk of the remaining oligonucleotide from the conjugate, as the combined total of 499.47 ± 47.0 (photocleavage) and 720.30 ± 69.9 (post PC DTT treatment), is indeed close to ~1300 recovered by DTT treatment alone. From these results we can deduce that DTT released PC-miR-148b more efficiently than photoactivation, which is not unexpected based on previous studies of oligo photocleavage[58] and nanoparticle stability.[53]

3.4.3 Photomodulated Upregulation of ALPL

ALP is one of the early protein enzymes expressed during osteogenesis and is displayed on the extracellular portion of the plasma membrane, resulting in increased local concentration of inorganic phosphate, a mineralization promoter, and decreased concentration of extracellular pyrophosphate, an inhibitor of mineral formation.[59] hASCs ALP expression was evaluated both qualitatively and quantitatively as a function of light activation after treatment with PC-miR-148b-SNP conjugates. Control groups included; miSpike-21mer (universal control), stromal media (SM) control and photoexposed hASCs while test groups are osteogenic media (OM) control, SM with single stranded cationic agent transfected miR148b mimic and OM with single stranded miR148b mimic. Figure 3.6 demonstrates the degree of ALP enzyme activity when hASCs were treated under different conditions. The control groups (Figure 3.6A, B and C), exhibit minimal ALP activity on the hASCs, and are poorly stained as seen by the normalized absorbance/number of hASCs ratio in Figure 3.6K. hASCs treated with test group demonstrated

increased ALP enzyme activity based on the appearance of darker staining (Figure 3.6D, E and F). The PC-miR-148b mimic and PC-miR-148b mimic+flashed sample (Figure 3.6G and H) did not upregulate ALP production and their normalized absorbance was similar to the control group. The major and most prominent upregulation of ALP was seen in PC-mir148b-SNP+flashed sample. The difference in enzyme activity can be appreciated while comparing the flashed and unflashed pair in Figure 3.6I and 3.6J where the normalized absorbance increased from 0.64 ± 0.07 to 2.50 ± 0.06. The photoactivation facilitated the release of PC-miR-148b from the conjugate, initiating the osteogenic differentiation of hASCs. The absorbance value of PC-miR148b-SNP+flashed differs significantly from SM (value of 0.94 ± 0.05, $p < 0.05$; one-sample t-test) but insignificantly from OM (value of 2.62 ± 0.04, $p > 0.05$; one-sample t-test).

The *ALP* up-regulation was further quantified with Q-PCR and the -ΔΔCt value relative to SM, is plotted in Figure 3.7. The control group have a negative -ΔΔCt value while the test groups, OM and SM+miR-148b, have a -ΔΔCt value of 2.42 ± 0.06 and 5.64 ± 3.9 after 7 days of transfection respectively. More importantly, the *ALP* -ΔΔCt value significantly increased to 1.65 ± 0.29 when the PC-miR148b-SNP conjugate was photoactivated, compared to a value of -6.3 ± 0.10 for non-light exposed controls. While this value is significantly lower than the OM control ($p<0.05$; one-sample t-test), the hASCs treated with the conjugate up-regulated the *ALP* production after light exposure arguing for a release of PC-miR-148b from the particle surface. The plasma membrane of osteoblasts are rich in ALP [60] and detection of high levels of ALP in cells treated with active conjugates indicate the presence of maturing osteoblasts in culture. ALP, expressed early in process of calcification, declines later in the developmental program when other genes/proteins like osteocalcin (OCN) are up-regulated.[61]

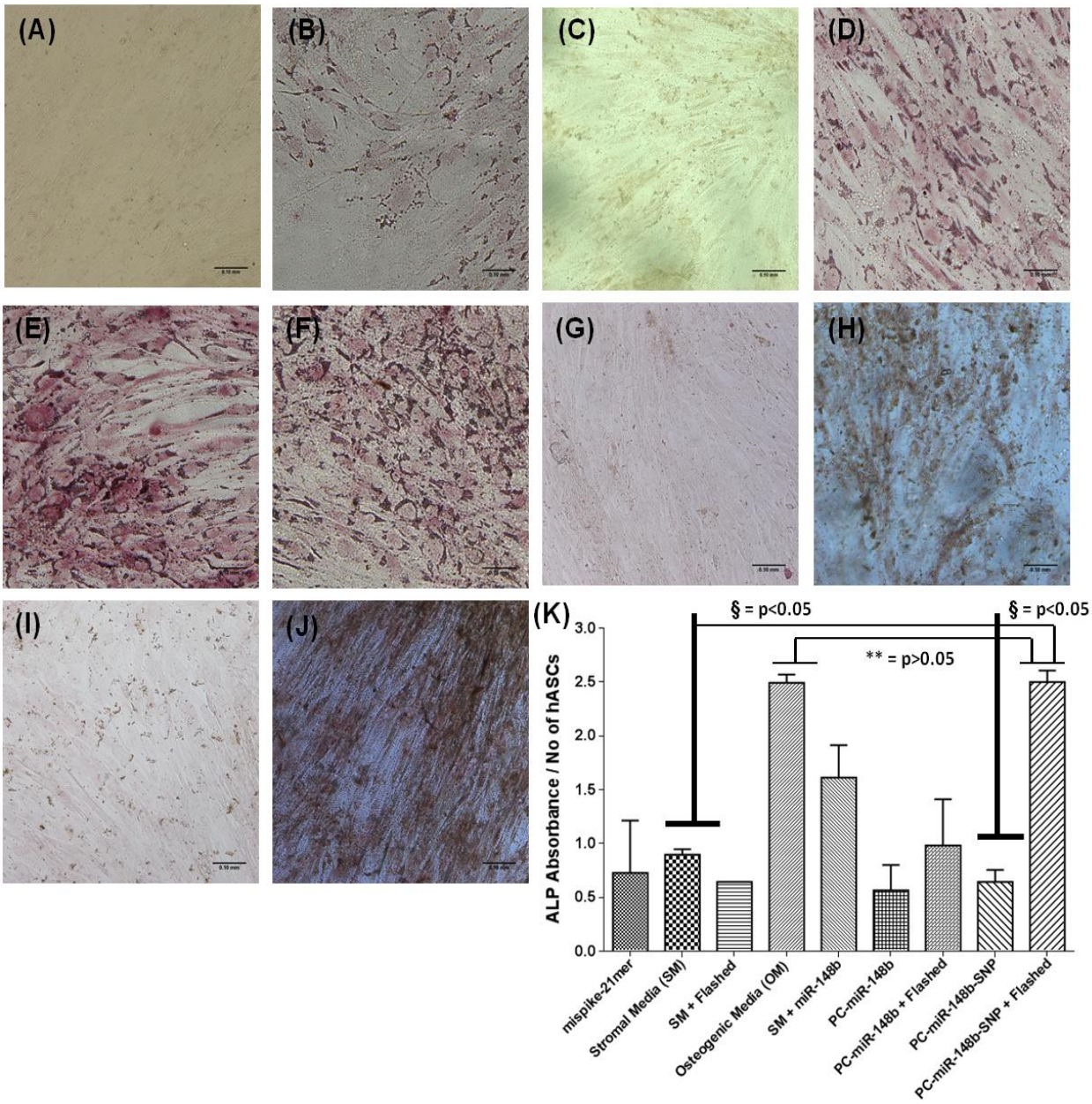

Figure 3.6 The hASCs treated were stained with ALP kit after treatment with (A) miSpike-21mer, (B) Stromal Media (SM), (C) SM and Flashed, (D) Osteogenic Media (OM), (E) SM+ miR148b, (F) OM+ miR148b, (G) PC-miR148b, (H) PC-miR148b + Flashed, (I) PC-miR148b-SNP and (J) PC-miR148b-SNP + Flashed. Magnification is 20x, and scale bar is 100um. (K) ALP produced by the cells after being treated with varying condition was then quantified by absorbance/Number of hASCs. § denotes significantly different ($p<0.05$; one-sample t-test). ** denotes statistically insignificant ($p>0.05$; one-sample t-test).

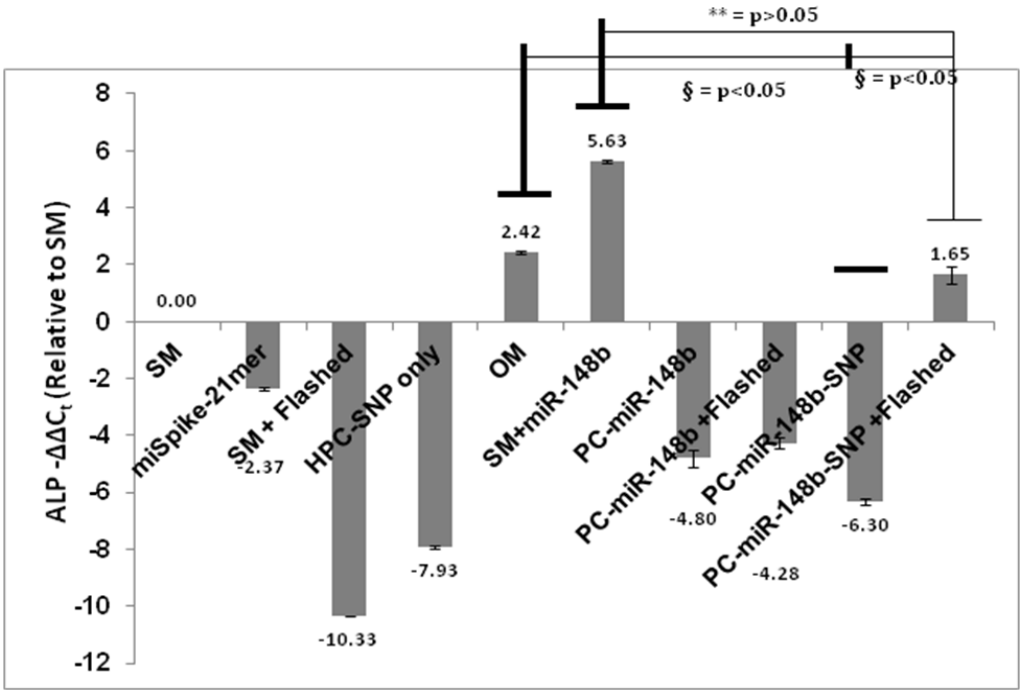

Figure 3.7. Alkaline Phosphatase, expression was quantified by qRT-PCR, ΔC_t value of each sample was calculated compared its human 18s rRNA control. The graph represents the - $\Delta \Delta C_t$ value of each sample calculated by the $\Delta\Delta C_t$ method, with comparison to SM sample. § denotes significantly different value ($p<0.05$; one-sample t-test) while ** denotes insignificantly different ($p>0.05$; one-sample t-test) values.

3.4.4 Mineralization of hASCs and Up-regulation of OCN and RUNX2

During mineralization, osteoblasts produce extracellular calcium deposits, which are an indication of bone formation. In this study calcium deposition was measured by Alizarin Red S staining and visualized on hASCs treated under different conditions at the 14 day time point (Figure 3.8). hASCs treated with miSpike-21mer, stromal media and photo-exposed hASCs served as control groups (Figure 3.8A, B and C), and showed minimal calcium deposition quantified in image 3.8K. hASCs treated with osteogenic media, SM with single stranded miR-148b mimic and OM with single stranded miR-148b mimic controls (Figure 3.8D, E and F) had increased red staining indicating calcium deposition confirmed by the increased normalized absorbance/number of hASCs ratio in image 3.8K. A clear increase in Alizarin Red S staining of

hASCs can be seen after photo-activating the conjugate to release PC-miR-148b from the SNPs (Figure 3.8I and 3.8J) where the normalized absorbance increased from $9.6 \times 10^{-6} \pm 9.6 \times 10^{-7}$ to $4.19 \times 10^{-5} \pm 7.11 \times 10^{-6}$. The absorbance value of PC-miR148b-SNP+flashed differs significantly from SM ($p < 0.05$; one-sample t-test) but insignificantly from OM ($p > 0.05$; one-sample t-test).

As can be seen from the no-light control the conjugate can remain inactive for a period of at least 14 days unless the payload is released by radiation. It is likely, that without photoclevage and release the miRNA payload is degraded after several days through hydrolysis and/or enzymatic degradation. The amount of PC-miR-148b released from the conjugate via photo-exposure is ~two fold less than the amount released by DTT but is sufficient initiate the osteogenic differentiation of hASCs. Similar to previously published studies, the progression of *in vitro* osteogenesis is characterized by decreased cellular proliferation followed by increased calcium deposition over time.[62]

To further characterize the differentiation of hASCs transfected with conjugate, the up-regulation of two well-documented middle and late stage osteogenic mRNA markers, *RunX2* and *OCN*, was measured by Q-PCR at day 28. Activated conjugate-treated hASCs show a 6.41 ± 1.14 *RunX2* $-\Delta\Delta Ct$ value compared to SM control, after 365nm photoexposure, which is not significantly different from OM, but is significantly different from SM+miR-148b controls. The $-\Delta\Delta Ct$ value increases from -4.24 ± 2.44 to 6.41 ± 1.14 with the light activation of the conjugate (Figure 3.9A). Similar trends are followed in the *OCN* upregulation where the $-\Delta\Delta Ct$ value of active conjugate (10.61 ± 3.53) is significantly different from its inactive form (-0.71 ± 2.4) and SM+miR-148b (4.41 ± 0.73) and significantly different from OM (7.97 ± 0.26) (Figure 3.9B). The mineralization of extracellular matrix correlates with the expression of *OCN*, osteopontin

(*OPN*), *RunX2* and bone morphogenetic proteins (*BMP*). [63, 64] BMPs initiate osteogenesis by activating the transcription of core binding factor a1 (*RunX2*), which then stimulate the osteoblast-specific genes such as *ALP* and *OCN* by binding to the osteoblast-specific cis-acting element 2 (OSE2) in the promoter region of these genes.[60] Marked increase in the levels of *ALP*, *OCN* and *RunX2* mRNA expression further indicates the osteogenic differentiation of hASCs with activated HPC-SNP + PC-miR148b.

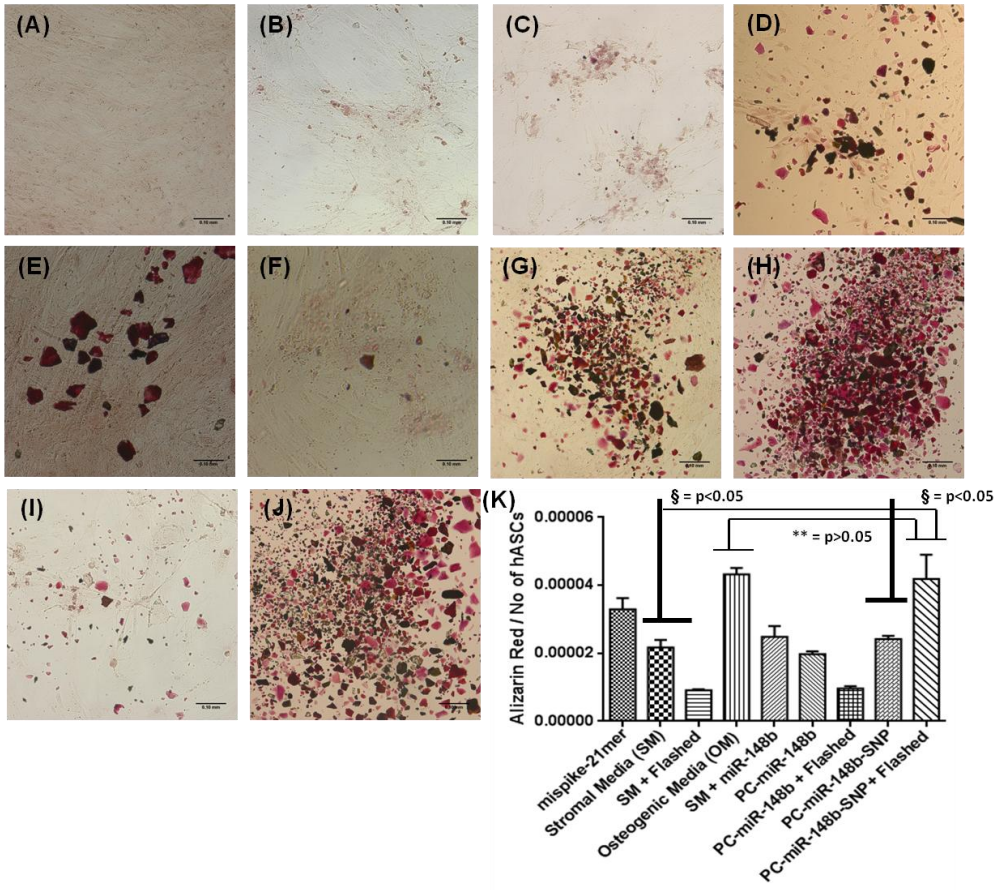

Figure 3.8. The mineralization of hASCs was quantified by staining cells with Alizarin Red. The conditions of treatment are (A) mispike-21mer, (B) Stromal Media (SM), (C) SM and Flashed, (D) Osteogenic Media (OM), (E) SM+ miR148b, (F) OM+ miR148b, (G) PC-miR148b, (H) PC-miR148b + Flashed, (I) PC-miR148b-SNP and (J) PC-miR148b-SNP+ Flashed. Magnification is 20x, and scale bar is 100um. (K) Mineralization of hASCs was quantifierd after being treated with varying condition was then quantified by absorbance/Number of hASCs. § denotes significantly different ($p<0.05$; one-sample t-test). ** denotes statistically insignificant ($p>0.05$; one-sample t-test).

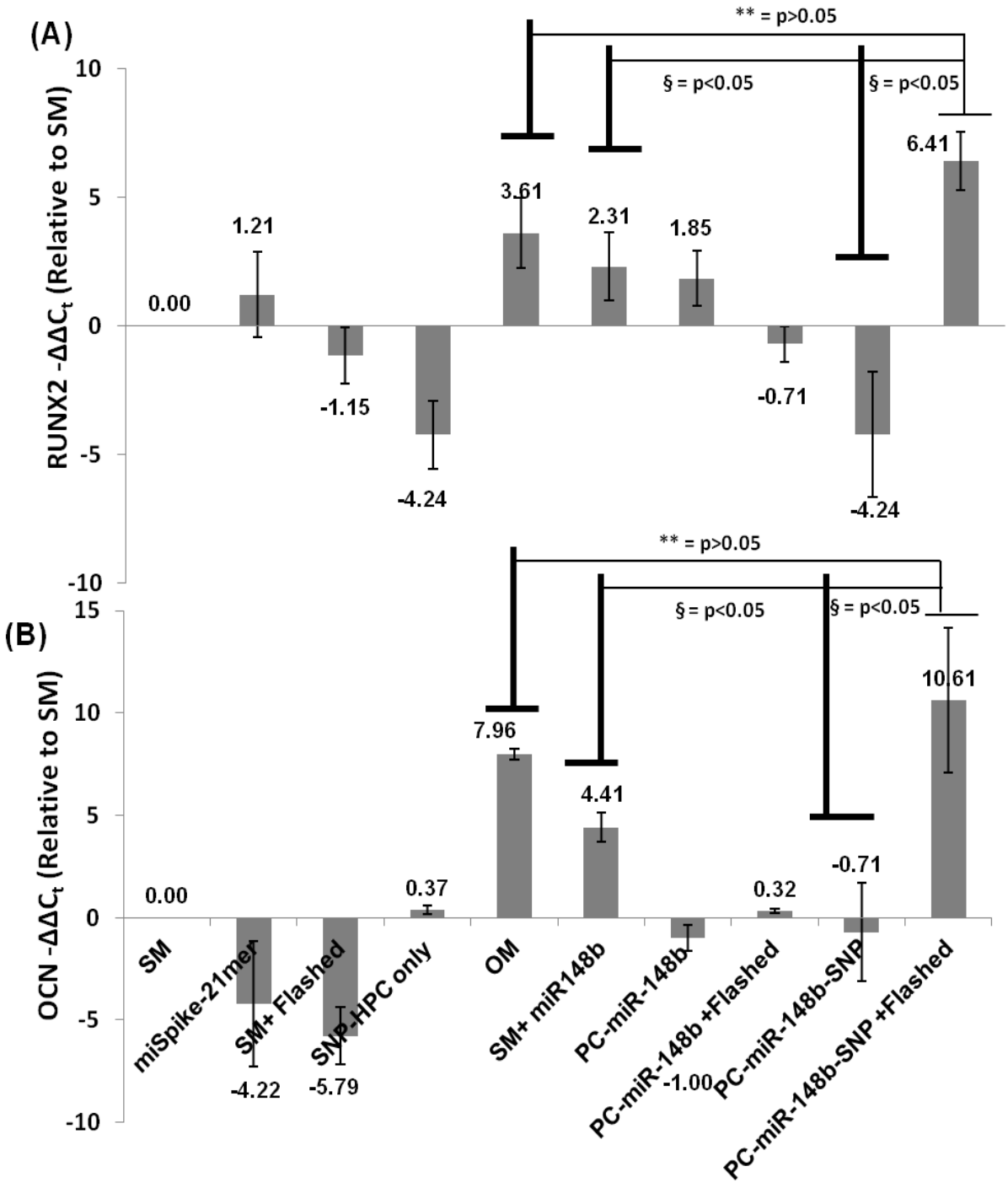

Figure 3.9. Up-regulation of late-stage osteogenic markers, osteocalcin (OCN) and RunX2 was quantified by qRT-PCR. ΔC_t value of each sample was calculated compared its human 18s rRNA control. The graph above represents the (A) RunX2 and (B) OCN - $\Delta \Delta C_t$ value of each sample calculated by the $\Delta\Delta C_t$ method, compared to SM sample. § denotes significantly different values ($p<0.05$; one-sample t-test) while ** denotes an insignificantly different values. ($p>0.05$; one-sample t-test)

3.4.5 Measuring *in vitro* Photo-release of PC-miR-148b with Confocal Microscopy

The release of PC-miR-148b was semi-quantitatively measured using confocal images of hASCs transfected miR-148b mimics using TurboFect or with the PC-miR148b-SNP conjugates (Figure 3.10). Panels b and c show the reflectance mode image of SNPs (488nm/498nm) and fluorescence of 6-TAMRA (531nm/572nm) respectively. Figure 3.10 (*1a-1d* and *2a-d*) show the results of PC-miR-148b transfection into hASCs with TurboFect. The photoexposure does not appear to have any impact on the spatial distribution of the 6-TAMRA fluorescence in TurboFect transfected cells (compare Panel *1c* and *2c*), indicating that no intracellular redistribution of the 6-TAMRA labeled microRNA occurs as a result of light exposure. In contrast, delivery of PC-miR-148b-SNP conjugates to the intracellular environment was achieved without the use of transfection vectors (Panel *3a-3d* and *4a-4d*). The resulting fluorescent distribution is similar to that seen with TurboFect delivered PC-miR-148b (Panel *1a-1d* and 2*a-2d*). Overlay of particle reflectance with TAMRA-labeled oligonucleotide fluorescence was used to calculate co-localization coefficients (Mander's Coefficient).[65] The images in Figure 3.10 (Panel 3d and 4d) indicate the change in co-localization of the SNPs reflectance and 6-TAMRA fluorescence as a result of photo exposure in PC-miR-148b-SNP. The Mander's Coefficient for images *3d* and *4d* are 1 and 0.73 respectively. The PC-miR-148b-SNP conjugate with no light expsoure had 100% co-localization while UV radiation treatment correlate with a decreased colocalization SNPs reflectance and 6-TAMRA fluorescence of 73%. Based on the photorelease quantification studies described above some PC-miR-148b is expected to remain tethered to the particle with this light exposure regimen, accounting for the observed incomplete co-localization in photo-exposed samples.

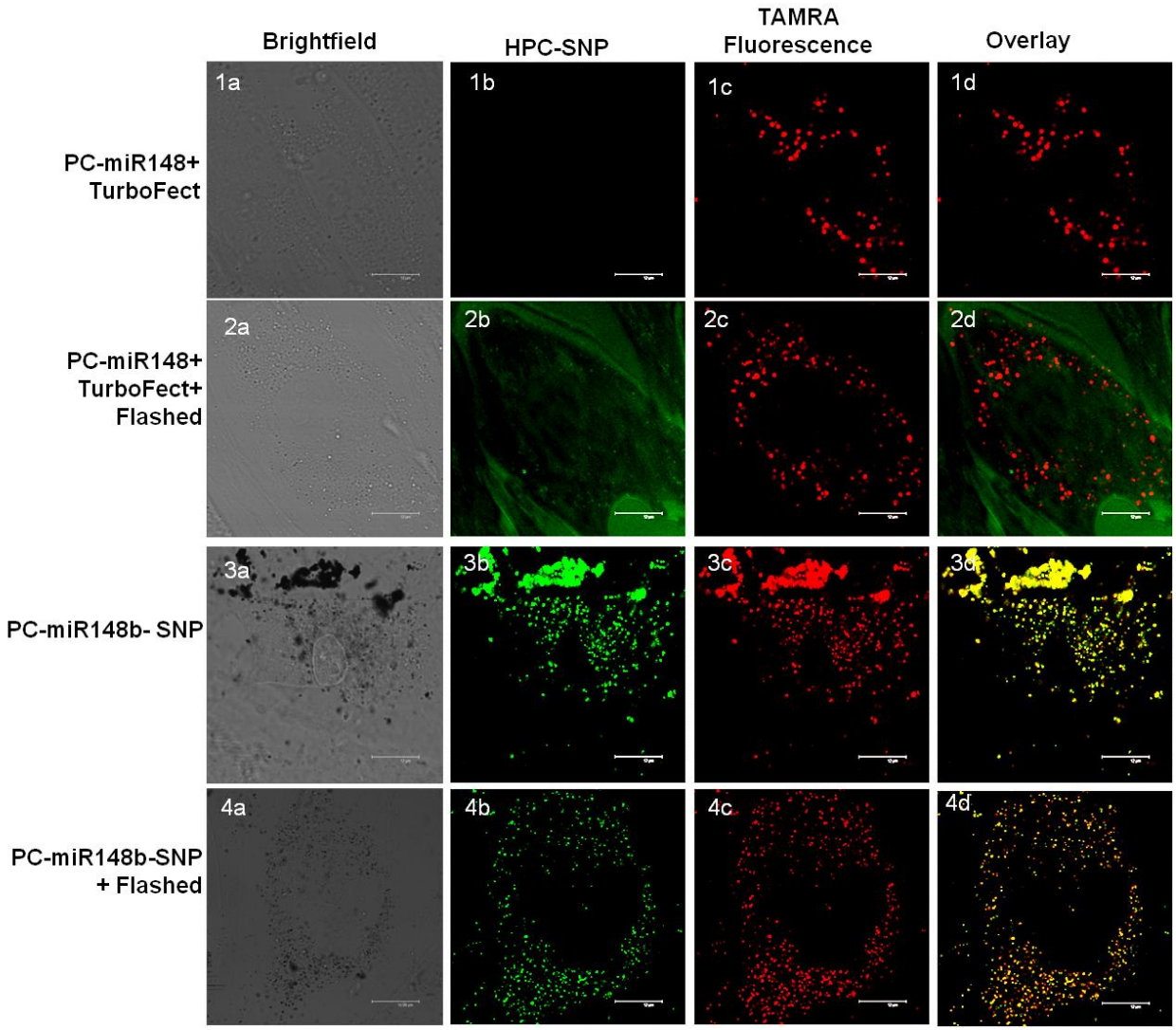

Figure 3.10 (1) PC-miR-148b, (2) PC-miR-148b+UV radiation, (3) PC-miR-148b-SNP and (4) PC-miR-148b-SNP+flashed delivery to hASCs to study the photo-release of oligonucleotide from the conjugate. Images depict (a) Brightfield views, (b) silver particle reflectance (488nm/598nm), (c) 6-TAMRA fluorescence (531/572nm) and (d) Reflectance + Fluorescence overlay. The Mander's Coefficient for images 3d and 4r are 1 and 0.73 respectively. Magnification is 63x, and scale bar is 12um.

3.4.6 OCN ELISA Expression

Osteocalcin is synthesized only by the osteoblast and although the majority of the synthesized osteocalcin is deposited into bone matrix at the time of bone mineralization, a small amount of OCN can be detected in serum[66, 67]. Therefore, it is expected that mature OCN protein can be detected in the conditioned culture media used for hASCs culture and

differentiation using an enzyme-linked immunosorbent assay (ELISA). The hASCs were treated with PC-miR148b-SNP and activated with UV radiation along with experimental and control groups detailed in section 2.3 for 14 and 28 days. The conditioned media from the final four days of culture were used for OCN protein expression determination. The concentration of OCN in ng/ml was normalized to the number of hASCs measured by PicoGreen. Light exposure of hASCs cultured with PC-miR-148b-SNP conjugates correlates with an increase in OCN protein expression (Figure 3.11) at 28days. The OCN levels detected from media of PC-miR148b-SNP treated hASCs increased from 0.004 ± 0.0007 to 0.0065 ± 0.003 with photoexposure. The value for SM + miR148b was 0.0065±0.001 which is not significantly different from non photoexposed PC-miR148b-SNP ($p>0.05$; one-sample t-test). In the OM media extract the OCN levels decreased from from 0.0059 ± 0.004 to 0.005 ± 0.0003 from 14 to 28 days respectively, indicating that induction of osteogenesis by OM and photoactivated PC-miR148b-SNP may result in differences in the time course of osteogenic marker expression. The OCN levels in the 14days OM was not significantly different from PC-miR148b-SNP ($p>0.05$; one-sample t-test). The control groups, SM and miSpike-21mer, had significantly lower values than from PC-miR148b-SNP value ($p<0.05$; one-sample t-test). This protein expression data is correlates with visual observation that mineralized nodules form in hASC cultured in OM as early as 14 days while this processes is temporally retarded in photoexposed PC-miR148b-SNP treated cells (data not shown). While this difference in timing of maximum OCN expression is interesting, the underlying cause is unclear. It is possible that this is miR148b mimic concentration related phenomena, i.e that increasing PC-miR148b-SNP dose will result in increased OCN concentration at day 14. Alternatively, osteogenic differentiation initiated by OM and miR148b

mimic may work through similar but not identical pathways. Future efforts will further explore this phenomenon.

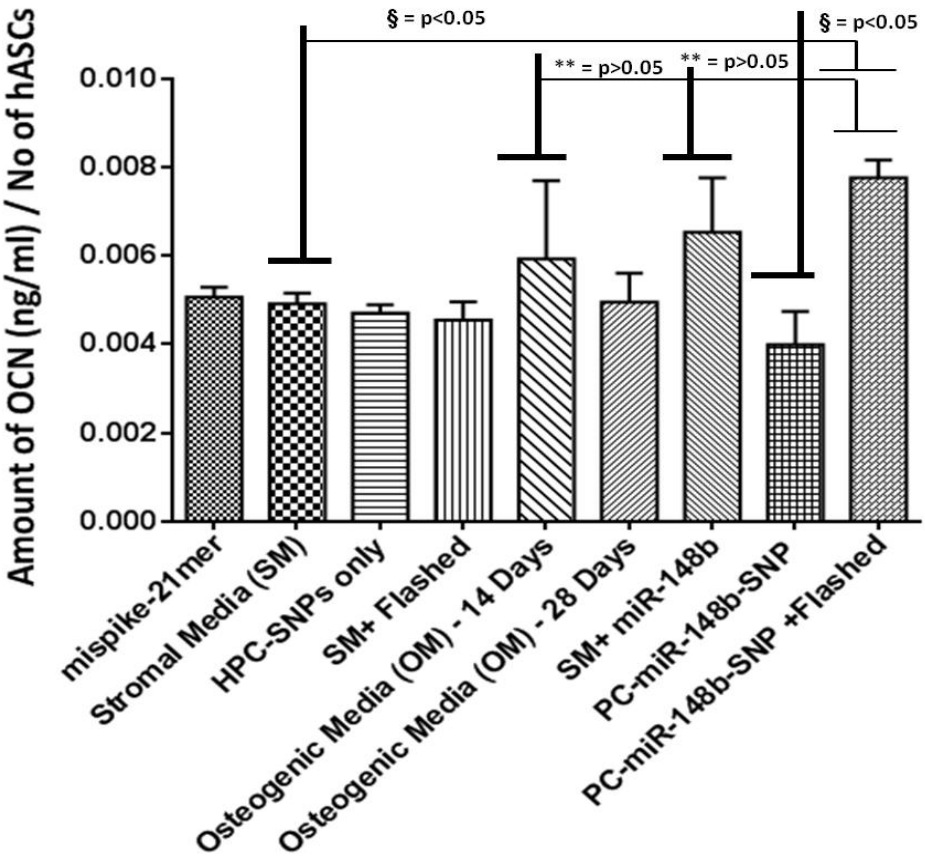

Figure 3.11. The cell media was collected and evaluated for OCN secretion by ELISA by measuring the 450 nm absorbance and quantifying with a standard curve. The amount of OCN (ng/ml) was then normalized to the numbe of hASCs measured by PicoGreen. § denotes significantly different ($p<0.05$; one-sample t-test) values while** denotes an insignificantly different values ($p>0.05$; one-sample t-test).

3.4.7 Cytotoxicity of PC-miR148b-SNP

The cytotoxicity of PC-miR148b-SNP was compared to appropriate controls via flow cytometry scatter and fluorescence analysis using Sytox Red exclusion as a live/dead reporter. Cells were analyzed after 28 days in culture and cells treated with the PC-miR148b-SNP construct showed little cytotoxic response in both light exposed and non exposed conditions (Figure 3.12). Light exposure and SNP treated hASC controls also demonstrated little reduction

in viable cell counts. The concentration of PC-miR148b and the SNPs, in the conjugates, was matched to the concentrations used in drive the osteogenic differentiation of hASCs in previous experiments. At these concentrations, 96.97 ± 1.5 % and 92.85 ± 5.24 % of hASCs were viable when exposed to PC-miR148b and HPC-SNPs respectively. Also the PC-miR148b-SNP conjugates showed minimal cytotoxicity regardless of light treatment as 90.68 ± 3.64% and 90.08 ± 2.12 % of hASC cells were viable in the non and photo-activated groups respectively. It should also be noted that the photo-activation via UV radiation had a non-significant effect of the viability of hASCs.

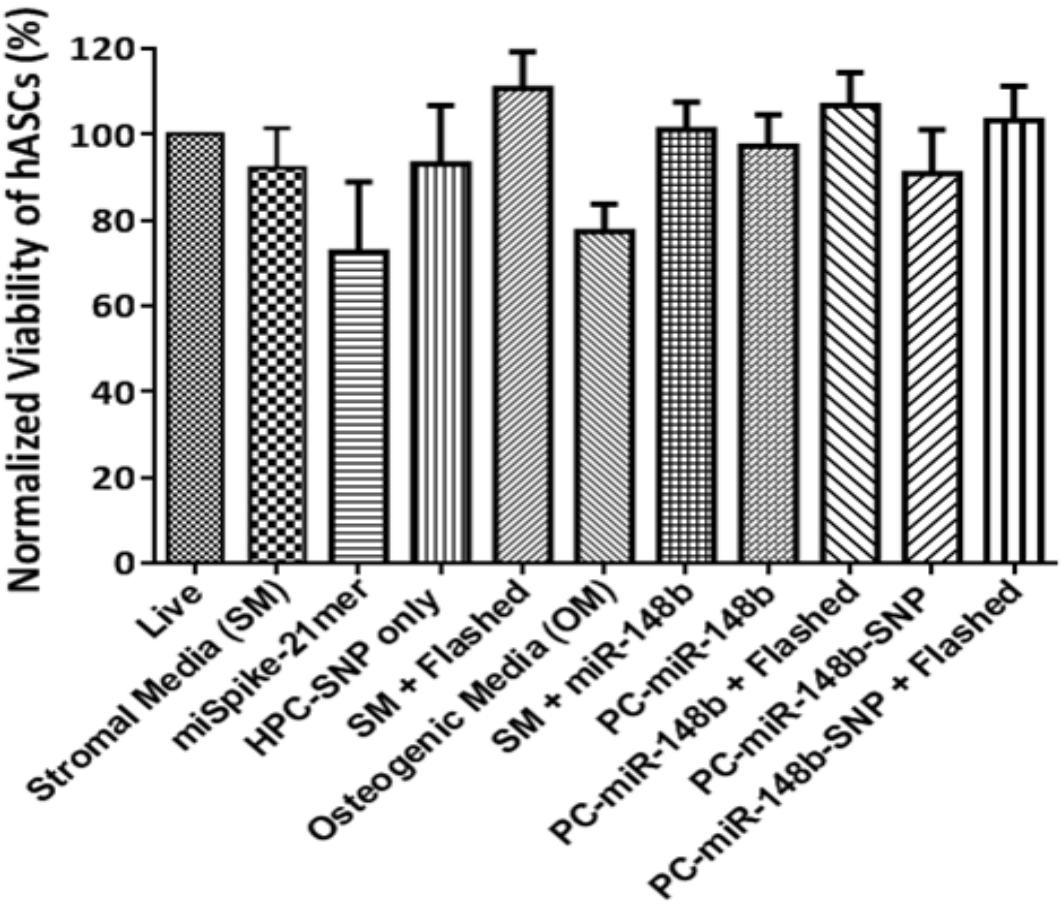

Figure 3.12. Normalized Viability of hASCs when exposed to different conditions. The percent viability of each sample was measured with Sytox Red and normalized to live control.

3.5 Discussion

Oligonucleotides caged with photocleavable compounds have been successfully used in the laboratory to modulate gene expression in zebrafish for developmental studies[68-71]_ precisely apply gradients of gene silencing [72] and better understand and create synthetic genetic circuits[73]. This technology can potentially one day be uniquely suited for optically-accessible clinical applications as it is recognized that this light activated miRNA delivery technology is generally limited to UV light accessible tissues such as the dermal, mucosal membrane, retinal, dental and maxillofacial tissues and pulmonary cases (reviewed in [74]). Without direct fiber delivery approaches, the penetration depth of photoactivating UV wavelengths into biological samples is very limited (as demonstrated in [75],) but doses can be optimized to achieve photoactivation *in vitro*[74] and *in vivo*[76] without significant biological damage. We suggest that additionally there is a potential orthopedic application in the surgical repair of trauma, joint replacement and wound beds where deep tissues are light accessible at the time of surgery. Consequently, the PC-miR-148b-SNP construct would permit fine spatial/temporal control of cell differentiation and tissue repair leading to improved clinical outcomes.

While the PC-miR-148b-SNP construct or cells transfected with these constructs may diffuse *in vivo*, they appear to remain inert until photoactivated, as demonstrated by differences between *ALP*, *RunX2* and *OCN* expression in light exposed and non-exposed PC-miR148b-SNP conjugate treated hASCs. Additionally, since miRNA are short lived and only transiently modulate mRNA expression, it is expected that there is little chance of permanent activity once an activated cell has begun differentiation. The miRNA associated with inactivated construct are expected to degrade slowly intracellularly or in the intercellular space through enzymatic action

or hydrolysis, reducing the potential spurious activtion resulting in heterotopic ossification of non-target tissues. The preliminary *in vitro* toxicity study demonstrated that at the osteogenic dose, PC-miR-148b-SNP show minimal cytotoxicity, comparable to controls, when transfected into hASCs. The normalized viability of all the samples was not significantly different from live control. Based on the current understanding of the systems' function and the data presented above, it is expected that PC-miR-148b-SNP construct may have advantages over current state of the art drug eluting bone-grafts and gene delivery vectors.

To translate this technology into a clinical setting, PC-miR148b-SNP conjugate containing hASCs will be loaded on a three dimensional (3D) natural or synthetic matrix and either photoactivated pre or post *in vivo* implantation. Our preliminary study demonstrated the UV penetration capability and photoactivation of PC-miR148b-SNP in a polycaprolactone (PCL) scaffold. The miR148b was released from the conjugate, driving hASC differentiation resulting in mineralization of the scaffolds.

Oligonucleotides caged with photocleavable compounds have been successfully used in the laboratory to modulate gene expression in zebrafish for developmental studies[68-71]_ precisely apply gradients of gene silencing [72] and better understand and create synthetic genetic circuits[73]. This technology can potentially one day be uniquely suited for optically-accessible clinical applications as it is recognized that this light activated miRNA delivery technology is generally limited to UV light accessible tissues such as the dermal, mucosal membrane, retinal, dental and maxillofacial tissues and pulmonary cases (reviewed in [74]). Without direct fiber delivery approaches, the penetration depth of photoactivating UV wavelengths into biological samples is very limited (as demonstrated in [75],) but doses can be optimized to achieve photoactivation *in vitro*[74] and *in vivo*[76] without significant biological

damage. We suggest that additionally there is a potential orthopedic application in the surgical repair of trauma, joint replacement and wound beds where deep tissues are light accessible at the time of surgery. Consequently, the PC-miR-148b-SNP construct would permit fine spatial/temporal control of cell differentiation and tissue repair leading to improved clinical outcomes.

While the PC-miR-148b-SNP construct or cells transfected with these constructs may diffuse *in vivo*, they appear to remain inert until photoactivated, as demonstrated by differences between *ALP*, *RunX2* and *OCN* expression in light exposed and non-exposed PC-miR148b-SNP conjugate treated hASCs. Additionally, since miRNA are short lived and only transiently modulate mRNA expression, it is expected that there is little chance of permanent activity once an activated cell has begun differentiation. The miRNA associated with inactivated construct are expected to degrade slowly intracellularly or in the intercellular space through enzymatic action or hydrolysis, reducing the potential spurious activtion resulting in heterotopic ossification of non-target tissues. The preliminary *in vitro* toxicity study demonstrated that at the osteogenic dose, PC-miR-148b-SNP show minimal cytotoxicity, comparable to controls, when transfected into hASCs. The normalized viability of all the samples was not significantly different from live control. Based on the current understanding of the systems' function and the data presented above, it is expected that PC-miR-148b-SNP construct may have advantages over current state of the art drug eluting bone-grafts and gene delivery vectors.

To translate this technology into a clinical setting, PC-miR148b-SNP conjugate containing hASCs will be loaded on a three dimensional (3D) natural or synthetic matrix and either photoactivated pre or post *in vivo* implantation. Our preliminary study demonstrated the UV penetration capability and photoactivation of PC-miR148b-SNP in a polycaprolactone (PCL)

scaffold. The miR148b was released from the conjugate, driving hASC differentiation resulting in mineralization of the scaffolds (Supplementary Figures: S5).

3.6 Conclusions

The findings herein concur with previous studies demonstrating the osteogenic potential of miR-148b mimic and further, it indicates that both miR-148b and miR-148b* mimic sub-sequences have discrete osteogenic properties. A facile in-place exchange method is described for the synthesis of PC-miR-148b-SNP conjugates for use as photo-activated miRNA particles. Light mediated spatial and temporal control of miR-148b mimic activation was demonstrated by driving hASCs osteogenic differentiation using the PC- miR-148b -SNP conjugate. The UV light was demonstrated to release PC-miR-148b from the conjugate and histological staining of cells showed the upregulation of alkaline phosphatase and the mineralization of hASCs when cultured with PC-miR148b-SNP conjugate and photoactivated. The up-regulation of *ALP, OCN* and *RunX2*, confirmed by Q-PCR, provides further support of osteogenic differentiation and indicates that miR-148b may drive osteogenesis through similar pathways modulated by OM. It was also shown that no-light control the conjugate remained inactive for a period of at least 14 days unless the payload was released by radiation. Changes in co-localization of the particle and miRNA payload occurred as function of light activation, indicating photoclevage and miRNA release from the particle intracellularly. This proof-of-concept study demonstrates the potential of the PC-miR-148b-SNP conjugates as a light activated miRNA delivery vehicle and the capability to modulate the osteogenic differentiation of hASCs using light as a non-invasive triggering modality.

3.7 References

1. Rhim, C., et al., *Effect of MicroRNA Modulation on Bioartificial Muscle Function.* Tissue Engineering Part A, 2010: p. 3589-3597.

2. Ambros, V., *The functions of animal microRNAs.* Nature, 2004. **431**(7006): p. 350-355.

3. Schoolmeesters, A., et al., *Functional Profiling Reveals Critical Role for miRNA in Differentiation of Human Mesenchymal Stem Cells.* Plos One, 2009. **4**(5): p. 9.

4. Li, Y.S., et al., *Optimising ultrasound-mediated gene transfer (sonoporation) in vitro and prolonged expression of a transgene in vivo: Potential applications for gene therapy of cancer.* Cancer Letters, 2009. **273**(1): p. 62-69.

5. Barhoumi, A., et al., *Light-induced release of DNA from plasmon-resonant nanoparticles: Towards light-controlled gene therapy.* Chemical Physics Letters, 2009. **482**(4-6): p. 171-179.

6. Braun, G.B., et al., *Laser-Activated Gene Silencing via Gold Nanoshell−siRNA Conjugates.* ACS Nano, 2009. **3**(7): p. 2007-2015.

7. Katz, E. and I. Willner, *Integrated nanoparticle-biomolecule hybrid systems: Synthesis, properties, and applications.* Angewandte Chemie-International Edition, 2004. **43**(45): p. 6042-6108.

8. Qureshi, A.T., et al., *Antimicrobial biocompatible bioscaffolds for orthopaedic implants.* Journal of Tissue Engineering and Regenerative Medicine, 2012.

9. Qureshi, A.T., et al., *Biocompatible/bioabsorbable silver nanocomposite coatings.* Journal of Applied Polymer Science, 2011. **120**(5): p. 3042-3053.

10. Percival, S.L., P. Bowler, and E.J. Woods, *Assessing the effect of an antimicrobial wound dressing on biofilms.* Wound Repair and Regeneration, 2008. **16**(1): p. 52-57.

11. Rai, M., A. Yadav, and A. Gade, *Silver nanoparticles as a new generation of antimicrobials.* Biotechnology Advances, 2009. **27**(1): p. 76-83.

12. Kim, Y.S., et al., *Twenty-eight-day oral toxicity, genotoxicity, and gender-related tissue distribution of silver nanoparticles in Sprague-Dawley rats.* Inhalation Toxicology, 2008. **20**(6): p. 575-583.

13. Tiwari, D.K., T. Jin, and J. Behari, *Dose-dependent in-vivo toxicity assessment of silver nanoparticle in Wistar rats.* Toxicology Mechanisms and Methods, 2011. **21**(1): p. 13-24.

14. Agasti, S.S., et al., *Photoregulated Release of Caged Anticancer Drugs from Gold Nanoparticles.* Journal of the American Chemical Society, 2009. **131**(16): p. 5728-5729.

15. Nakanishi, J., et al., *Light-Regulated Activation of Cellular Signaling by Gold Nanoparticles That Capture and Release Amines.* Journal of the American Chemical Society, 2009. **131**(11): p. 3822-3823.

16. Rosi, N.L., et al., *Oligonucleotide-Modified Gold Nanoparticles for Intracellular Gene Regulation.* Science, 2006. **312**(5776): p. 1027-1030.

17. Giljohann, D.A., et al., *Oligonucleotide loading determines cellular uptake of DNA-modified gold nanoparticles.* Nano Letters, 2007. **7**(12): p. 3818-3821.

18. Giljohann, D.A., et al., *Gene Regulation with Polyvalent siRNA-Nanoparticle Conjugates.* Journal of the American Chemical Society, 2009. **131**(6): p. 2072-+.

19. Oishi, M., et al., *Smart PEGylated gold nanoparticles for the cytoplasmic delivery of siRNA to induce enhanced gene silencing.* Chemistry Letters, 2006. **35**(9): p. 1046-1047.

20. Song, W.J., et al., *Gold Nanoparticles Capped with Polyethyleneimine for Enhanced siRNA Delivery.* Small, 2010. **6**(2): p. 239-246.

21. Ghosh, P., et al., *Gold nanoparticles in delivery applications.* Advanced Drug Delivery Reviews, 2008. **60**(11): p. 1307-1315.

22. Seferos, D.S., et al., *Polyvalent DNA Nanoparticle Conjugates Stabilize Nucleic Acids.* Nano Letters, 2009. **9**(1): p. 308-311.

23. Poliseno, L., et al., *MicroRNAs modulate the angiogenic properties of HUVECs.* Blood, 2006. **108**(13976096728479933779related:U6WLD-0R9cEJ): p. 3068.

24. Davis, B.N., et al., *Induction of microRNA-221 by platelet-derived growth factor signaling is critical for modulation of vascular smooth muscle phenotype.* Journal of Biological Chemistry, 2009. **284**(6): p. 3728.

25. Emerich, D.F. and C.G. Thanos, *The pinpoint promise of nanoparticle-based drug delivery and molecular diagnosis.* Biomolecular Engineering, 2006. **23**(4): p. 171-184.

26. Polizzi, M.A., N.A. Stasko, and M.H. Schoenfisch, *Water-soluble nitric oxide-releasing gold nanoparticles.* Langmuir, 2007. **23**(9): p. 4938-4943.

27. Hong, R., et al., *Glutathione-mediated delivery and release using monolayer protected nanoparticle carriers.* Journal of the American Chemical Society, 2006. **128**(4): p. 1078-1079.

28. Ellis-Davies, G.C.R., *Caged compounds: photorelease technology for control of cellular chemistry and physiology.* Nature Methods, 2007. **4**(8): p. 619-628.

29. Monroe, W.T., et al., *Targeting expression with light using caged DNA.* Journal of Biological Chemistry, 1999. **274**(30): p. 20895-20900.

30. Buff, M., T. Mack, and A. Heckel, *Light-Activatable Nucleic Acids 'Caged' at the Nucleobases.* Chimia, 2009. **63**(5): p. 261-264.

31. Yguerabide, J. and E.E. Yguerabide, *Light-scattering submicroscopic particles as highly fluorescent analogs and their use as tracer labels in clinical and biological applications - I. Theory.* Analytical Biochemistry, 1998. **262**(2): p. 137-156.

32. Thompson, D.G., et al., *Ultrasensitive DNA detection using oligonucleotide-silver nanoparticle conjugates.* Analytical Chemistry, 2008. **80**(8): p. 2805-2810.

33. Graham, D., et al., *Functionalized nanoparticles for bioanalysis by SERRS.* Biochemical Society Transactions, 2009. **37**: p. 697-701.

34. Fu, Y., J. Zhang, and J.R. Lakowicz, *Plasmonic enhancement of single-molecule fluorescence near a silver nanoparticle.* Journal of Fluorescence, 2007. **17**(6): p. 811-816.

35. Wolkow, R. and M. Moskovits, *Enhanced photochemistry on silver surfaces.* The Journal of chemical physics, 1987. **87**(10): p. 5858-5869.

36. Kamat, P.V., *Photophysical, photochemical and photocatalytic aspects of metal nanoparticles.* The Journal of Physical Chemistry B, 2002. **106**(32): p. 7729-7744.

37. Yguerabide, J. and E.E. Yguerabide, *Light-scattering submicroscopic particles as highly fluorescent analogs and their use as tracer labels in clinical and biological applications - II. Experimental characterization.* Analytical Biochemistry, 1998. **262**(2): p. 157-176.

38. Jeffrey M. Gimble, B.A.B., Farshid Guilak, Steven R. Smith, and Adam J. Katz, *Isolation and Growth of Stem Cells.* Tissue Engineering, 2011. **643**.

39. Christian, P. and M. Bromfield, *Preparation of small silver, gold and copper nanoparticles which disperse in both polar and non-polar solvents.* J. Mater. Chem., 2009. **20**(6): p. 1135-1139.

40. Demers, L.M., et al., *A fluorescence-based method for determining the surface coverage and hybridization efficiency of thiol-capped oligonucleotides bound to gold thin films and nanoparticles.* Analytical Chemistry, 2000. **72**(22): p. 5535-5541.

41. Eskildsen, T., et al., *MicroRNA-138 regulates osteogenic differentiation of human stromal (mesenchymal) stem cells in vivo.* Proceedings of the National Academy of Sciences of the United States of America, 2011. **108**(15): p. 6139-6144.

42. Idris, A.I., et al., *Small molecule inhibitors of IκB kinase signaling inhibit osteoclast formation in vitro and prevent ovariectomy-induced bone loss in vivo.* The FASEB Journal, 2010. **24**(11): p. 4545-4555.

43. Liu, Q.H., et al., *A comparative study of proliferation and osteogenic differentiation of adipose-derived stem cells on akermanite and beta-TCP ceramics.* Biomaterials, 2008. **29**(36): p. 4792-4799.

44. Hennessy, K.M., et al., *The effect of collagen I mimetic peptides on mesenchymal stem cell adhesion and differentiation, and on bone formation at hydroxyapatite surfaces.* Biomaterials, 2009. **30**(10): p. 1898-1909.

45. Brown, P.K., et al., *Silver Nanoscale Antisense Drug Delivery System For Photoactivated Gene Silencing.* ACS Nano, 2012 in press.

46. AshaRani, P.V., et al., *Cytotoxicity and Genotoxicity of Silver Nanoparticles in Human Cells.* ACS Nano, 2009. **3**(2): p. 279-290.

47. Boisselier, E. and D. Astruc, *Gold nanoparticles in nanomedicine: preparations, imaging, diagnostics, therapies and toxicity.* Chemical Society Reviews, 2009. **38**(6): p. 1759-1782.

48. Link, S. and M. El-Sayed, *Size and temperature dependence of the plasmon absorption of colloidal gold nanoparticles.* J. Phys. Chem. B, 1999. **103**(21): p. 4212-4217.

49. Zhang, L., et al., *Reducing Stress on Cells with Apoferritin-Encapsulated Platinum Nanoparticles.* Nano Letters, 2009. **10**(1): p. 219-223.

50. Mie, G., *Articles on the optical characteristics of turbid tubes, especially colloidal metal solutions.* Annalen Der Physik, 1908. **25**(3): p. 377-445.

51. Mulvaney, P., *Surface Plasmon Spectroscopy of Nanosized Metal Particles.* Langmuir, 1996. **12**(3): p. 788-800.

52. Jain, P.K., et al., *Review of some interesting surface plasmon resonance-enhanced properties of noble metal nanoparticles and their applications to biosystems.* Plasmonics, 2007. **2**(3): p. 107-118.

53. Li, Z., et al., *Multiple thiol-anchor capped DNA–gold nanoparticle conjugates.* Nucleic acids research, 2002. **30**(7): p. 1558-1562.

54. Hurst, S.J., A.K.R. Lytton-Jean, and C.A. Mirkin, *Maximizing DNA loading on a range of gold nanoparticle sizes.* Analytical Chemistry, 2006. **78**(24): p. 8313-8318.

55. Herne, T.M. and M.J. Tarlov, *Characterization of DNA probes immobilized on gold surfaces.* Journal of the American Chemical Society, 1997. **119**(38): p. 8916-8920.

56. Demers, L.M., et al., *A fluorescence-based method for determining the surface coverage and hybridization efficiency of thiol-capped oligonucleotides bound to gold thin films and nanoparticles.* Analytical Chemistry, 2000. **72**(22): p. 5535-5541.

57. Hill, H.D., et al., *The Role Radius of Curvature Plays in Thiolated Oligonucleotide Loading on Gold Nanoparticles.* Acs Nano, 2009. **3**(2): p. 418-424.

58. Brown, P.K., et al., *Silver Nanoscale Antisense Drug Delivery System for Photoactivated Gene Silencing.* ACS Nano, 2013. **7**(4): p. 2948-2959.

59. Ellis E. Golub, K.B.-B., *The role of alkaline phosphatase in mineralization.* Current Opinion in Orthopaedics, 2007. **18**: p. 444-448.

60. Milat, F. and K.W. Ng, *Is Wnt signalling the final common pathway leading to bone formation?* Molecular and Cellular Endocrinology, 2009. **310**(1-2): p. 52-62.

61. Zanetti, A., et al., *Characterization of novel akermanite:poly-epsilon-caprolactone scaffolds for human adipose-derived stem cells bone tissue engineering.* Journal of Tissue Engineering and Regenerative Medicine, 2012.

62. Bauer, T.W. and G.F. Muschler, *Bone graft materials - An overview of the basic science.* Clinical Orthopaedics and Related Research, 2000(371): p. 10-27.

63. Bunnell, B.A., et al., *Differentiation of adipose stem cells.* Methods in Molecular Biology-Clifton then Totowa, 2008. **456**: p. 155.

64. Pasarica, M., et al., *Adipogenic human adenovirus Ad-36 induces commitment, differentiation, and lipid accumulation in human adipose-derived stem cells.* Stem Cells, 2008. **26**(4): p. 969-978.

65. Zinchuk, V., O. Zinchuk, and T. Okada, *Quantitative colocalization analysis of multicolor confocal immunofluorescence microscopy images: Pushing pixels to explore biological phenomena.* Acta Histochemica Et Cytochemica, 2007. **40**(4): p. 101-111.

66. Birmingham, E., et al., *Osteogenic Differentiation of Mesenchymal stem sells is regulated by osteocyte and osteoblast cell in a simplified bone niche.* European Cells & Materials, 2012. **23**: p. 13-27.

67. Gundberg, C.M. and M.E. Clough, *The osteocalcin propeptide is not secreted in vivo or in vitro.* Journal of Bone and Mineral Research, 1992. **7**(1): p. 73-80.

68. Wang, Y., et al., *Manipulation of gene expression in zebrafish using caged circular morpholino oligomers.* Nucleic acids research, 2012.

69. Tang, X.J., et al., *Regulating gene expression in zebrafish embryos using light-activated, negatively charged peptide nucleic acids.* Journal of the American Chemical Society, 2007. **129**(36): p. 11000-11001.

70. Blidner, R.A., et al., *Photoinduced RNA interference using DMNPE-caged 2'-deoxy-2'-fluoro substituted nucleic acids in vitro and in vivo.* Molecular BioSystems, 2008. **4**(5): p. 431-440.

71. Ando, H., et al., *Photo-mediated gene activation using caged RNA/DNA in zebrafish embryos.* Nature genetics, 2001. **28**(4): p. 317-326.

72. Jain, P.K., S. Shah, and S.H. Friedman, *Patterning of Gene Expression Using New Photolabile Groups Applied to Light Activated RNAi.* Journal of the American Chemical Society, 2010. **133**(3): p. 440-446.

73. Gardner, L. and A. Deiters, *Light-controlled synthetic gene circuits.* Current Opinion in Chemical Biology, 2012.

74. Forman, J., M. Dietrich, and W.T. Monroe, *Photobiological and thermal effects of photoactivating UVA light doses on cell cultures.* Photochem. Photobiol. Sci., 2007. **6**(6): p. 649-658.

75. Parpura, V. and P. Haydon, *" Uncaging" using optical fibers to deliver UV light directly to the sample.* Croatian medical journal, 1999. **40**(3): p. 340.

76. Dong, Q., et al., *Photobiological effects of UVA and UVB light in zebrafish embryos: Evidence for a competent photorepair system.* Journal of Photochemistry and Photobiology B: Biology, 2007. **88**(2): p. 137-146.

Chapter 4. Light Activated miR-148b-Nanoparticle Conjugates Heal Critical Size Mouse Calvarial Defects

4.1 Project Summary

Targeted delivery and controlled release of oligonucleotide therapeutics *in vivo* are essential aspects of an ideal gene delivery vehicle. Delivery systems providing spatial and temporal control have the potential to improve outcomes in surgical reconstruction and regenerative medicine by precise modulation of wound healing and tissue repair processes. We combined this technique with human autologous progenitor cells and used microRNA (miRNA) to modulate gene expression for improved closure of a critical size defect drilled on the left parietal bone of the male CD-1 nude homozygous mice. The hASCs loaded scaffold were incubated with PC-miR-148b-SNP conjugates and activated prior to implantation. After 4 and 12 weeks, the 3D u-CT reconstructed images showed the percent bone headlining increased from 3.83 ± 1.19 to 6.54 ± 4.28 and 10.91 ± 5.45 to 22.30 ± 4.93 for non-photoactivated and photoactivated conjugates respectively. The osteogenic differentiation of hASCs, with photo-released miR-148b, supported by the scaffold assisted in the closure of the defect. The results were confirmed with H&E and Masson's Trichrome stains in the transverse sections of photoactivated conjugates, the collagen fiber lining thickened the most at 12 weeks and was of the same density and thicknesses as the pre-existing calvarium. Mineralization of the new bone could also be visualized with colonies of dark purple bone marrow present in the tick collagen lining.

4.2 Introduction

Skeletal homeostasis is an active process that involves the balancing function of multiple factors affecting the metabolic activity of pre-osteoblasts. Growth factors like IGFs or TGFβs are released during resorption and initiate local bone formation[1, 2] while other factors deposited on

the bone surface by osteoclasts at the end of bone resorption initiate the following phase of bone formation.[3] Other factors like parathyroid hormone and prostaglandin E can act complementary to each other and stimulate both bone resorption and bone formation. Apart from these factors, other cytokines and hormones mediate the receptors on the osteoblast-lineage cells leading to maintenance of bone turnover by an effective osteoblast–osteoclast interaction.[4] Skeletal cells synthesize several growth factors including bone morphogenetic proteins (BMPs) that induce osteogenic differentiation of mesenchymal cells. On the molecular level, exposure of appropriate microRNAs (miRNA), non-coding RNAs involved in post-transcriptional regulation pathways and often associated with RNA silencing complexes, can be used to modulate the osteogenic differentiation of human adipose derived stem cells (hASCs)[5-7]. This technique could serve as an attractive therapeutic modality for regenerative medicine and is of particular interest in the design of therapies for critical size bone defects, spinal fusion and skeletal reconstruction.

Currently, allogenic or autogenic graft materials are widely and successfully used for the repair of skeletal bone defects but this technique has disadvantages including rejection, infection, limited supply and donor site morbidity due to operation respectively.[8] Adipose tissue is an abundant and accessible source of stromal/stem cells that is isolated from patients commonly through liposuction surgeries. The lipoaspirate is digested by collagenase and multiple centrifugation steps. The derived multipotent hASCs have the potential to differentiate along the adipocyte, chondrocyte, myocyte, neuronal, and osteoblast lineages. These hASCs have potential applications for the repair and regeneration of acute and chronically damaged tissues if activated with appropriate inductive factors.[9]

Our previously described light activated miRNA delivery system, with demonstrated capability, *in vitro,* to upregulate *alkaline phosphatase (ALP) and osteocalcin (OCN)* and mineralization of hASCs[10], will provide greater temporal and spatial control over the activation of differentiation and potentially improve healing of critical size defects. The hASCs transfected with light activated-miR-148b delivery conjugates will remain inert until activated with light. Additionally, since miRNA are short lived and only transiently modulate mRNA expression, it is expected that there is little chance of permanent activity once an activated cell has begun differentiation.

To study the bone formation due to osteogenic factors *in vivo* many rodent models have been used. On a molecular level, cells homogeneously expressing green fluorescent protein (GFP) can labeled and tracked [11, 12] while the physical models range from axial loading of tibia[13] to closure of critical size defects (CSD)[14, 15]. Previously, CSD models have been used for both the evaluation of normal healing, and the use of ASCs for the healing of critical sized (or non-healing) defects.[15] Here we have adapted this previously described CSD model for the evaluation healing in conjunction with hASCs transfected with light activated miRNA-148b-SNP conjugates.

Researchers have widely reported the therapeutic advantages of delivering stem cells with appropriate growth and inductive factors in biodegradable scaffolds providing appropriate physiological environments.[16-18] To evaluate the potential of this light activated miRNA delivery system to modulate CSD healing, we loaded hASC transfected with miRNA-148b-SNP conjugates on to scaffolds composed of polycaprolactone (PCL) as it has been previously demonstrated to have little impact on hASC differentiation. The *in vivo* osteogenic capability of

hASCs and bone formation once induced by our light activated miRNA-148b-SNP conjugates was histologically tested and through microCT analysis.[19]

4.3 Materials and Methods

4.3.1 Dosage Dependence Mineralization

Varying concentrations of PC-miR-148b-SNP conjugates (10-100ul of 227.2 ±1.7 ppm SNP or 0.120-1.20nM) were added to hASCs and ALPL upregulation and mineralization of hASCs was tested at day 7 and 14 respectively. The ALPL up-regulation was qualitatively and quantitatively measured by Millipore kits, SCR 004 and SCR 066 while the mineralization of the cells was quantified with Alizarin Red S stain

4.3.2. Calvarial Size Mouse Defects

All animal studies were purchased from Jackson Laboratory and housed in the LSU Life Sciences Vivarium on the Louisiana State University campus. The Animal Facility was accessed only by the authorized personnel that follow PPE protocols and its temperature, ventilation and illumination was controlled. The animal study was approved by LSU IACUC, protocol # 13-004. *In vivo* studies were conducted on adult (42 day –old) male CD-1 nude homozygous mice 20-40g (Jakckson Laboratory J:NU Stock Number: 007850). Surgery and all peri-operative procedures were conducted at LSU Veterinary School and transported to the LSU Life Science Vivarium where the mice were maintained and evaluated periodically till euthanized after 12 weeks. The guidelines for Transportation of animals from Louisiana State University were thoroughly followed.

To avoid incompatibility of xenografted human tissue, an athymic mouse served as the model organism. Briefly, non-healing, critical-sized calvarial defects (4 mm) were created in the left parietal bone of adult male CD-1 nude mice using a high-speed 4.6 OD Trephine Bur (ACE

Surgical, Brockton, MA) and saline irrigation. Animals were anesthetized with inhalant isoflurane. After disinfection, an incision was made just off the sagittal midline to expose the left parietal bone. Unilateral full-thickness critical-size calvarial defects were created in the non-suture associated left parietal bone, while the dura mater is left undisturbed. The surgical sites were stapled and the animals were monitored per established post-operative animal care protocols.

In preparation for implantation, Polycaprolactone (PCL) (4mm dia and 1mm thick) scaffolds were synthesized as previously described by Qureshi et al [20] and seeded with hASCs. 1.0-1.5 x 10^5 cells were resuspended in 20 ul of stromal media (DMEM, 10% FBS, 1% penicillin/streptomycin) and seeded on the PCL scaffolds by pipetting 10 ul of cells on top of each side. The scaffolds were then incubated at 5% CO2 and 37°C for 2 hrs before submerging it in 300 ul of stromal media for 24 hrs prior to PC-miR-148b-SNP construct treatment. 10 ul of PC-miR148b-SNP construct (227.2 ± 1.7 ppm SNP and 40 nM PC-miR-148b) was added to scaffolds for 16 hr before photo-release. For photo-release, the PC-miR148b-SNP treated scaffolds were photo-activated for 5 min at 365nm (52.4 J/cm^2) by means of a GreenSpot system (Figure 4.1). Animals were split into two experimental groups, two positive and three negative controls and were tested for closure of the defect at 4 and 12 weeks. The experimental groups included 1) PCmiR-148b-SNP and 2) PCmiR-148b-SNP + UV (n= 6 each) while negative controls included 1) PCL scaffold only, 2) empty defect only and 3) scaffold with miSpike-21mer (n=2 each). The positive controls included 1) scaffold with hASCs and 2) defect with osteogenic scaffold (n=6 each) (Table 4.1). Before implantation, cell-seeded scaffolds were rinsed in sterile PBS to prevent transfer of medium derived growth factors or immunogens. After implantation, animals were allowed to recover under heating pads for one hour before being

returned to the animal facility. Thereafter, animals were observed once daily for three days and weekly thereafter to ensure postoperative recovery (Figure 4.2).

Table 4.1. The experimental set up of the CSD model.

Assays	Experimental Groups	Animals per group
•Histological (H&E stain, Trichome Masson's and Lizarin Red S) • microCT evaluation for bone formation of the defect site.	Scaffold Control	2
	Empty Calvarial Defect Control	2
	Saccold + miSpike-21mer	2
	Scaffold+ hASCs	6
	Scaffold+ hASCs (OM)	6
	PC-miR-148b-SNP	6
	PC-miR-148b-SNP + UV Radiation	6
		30 animals

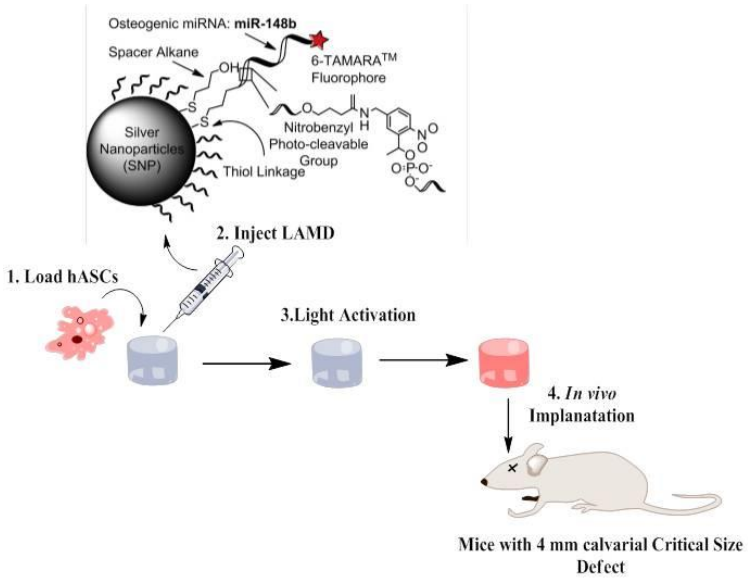

Figure 4.1. Procedure for calvarial size defect surgery preparation. The hASCs are loaded on PCL scaffolds and after 24 hrs the PC-miR148b-SNP conjugates are added on the scaffolds. The scaffolds are activated with UV and implanted on the CD-nude mice.

4.3.3. *In Vivo* Imaging

The animals were sacrificed by CO_2 asphyxiation and cervical dislocation was conducted to study the growth of skeletal bone with the light activated miR-148b-SNp conjugates. Micro

computed tomography was performed, using SkyScan 1074 tomography imaging system (Micro Photonics, Allentown, PA, USA). The following settings were used: 40 kVp polychromatic x-ray beam; field of view of 28 mm in diameter and 19 mm in height, current of 1000uA and an exposure time of 420 milliseconds for each of the 360 rotational steps. The 2D projection images were used to reconstruct tomograms with a commercial package (Avizo 8, Mercury Computer Systems, Berlin, Germany). Percentage healing in the region of the defect was evaluated using Image J (NIH, Bethesda, MD).

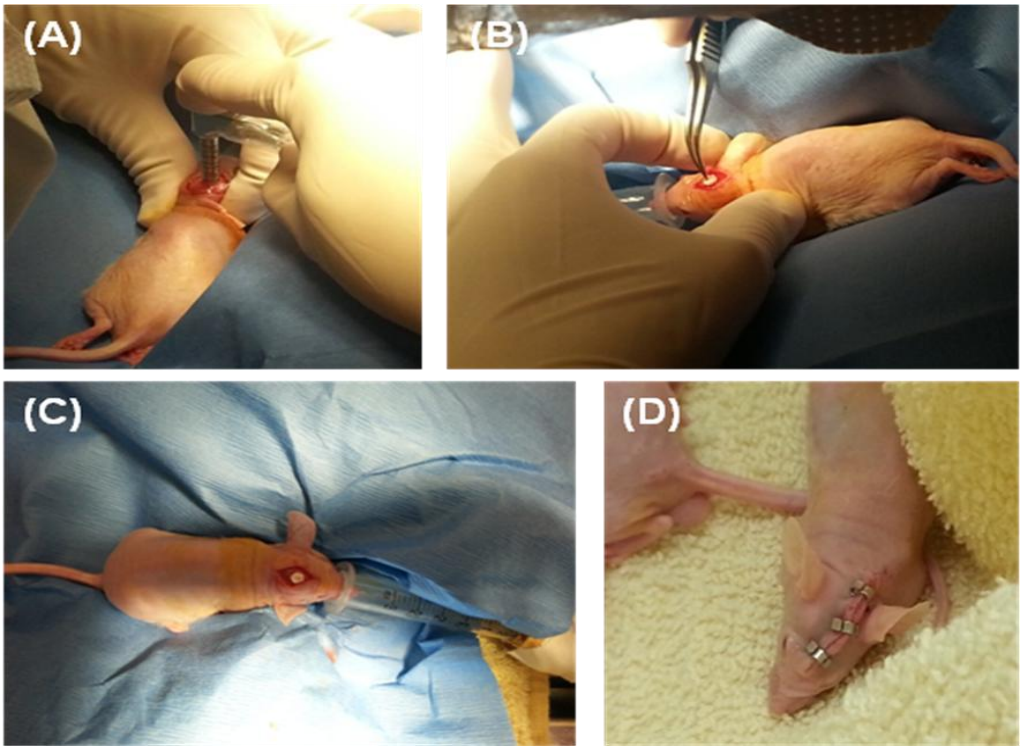

Figure 4.2. Calvarial size defect surgery was conducted under LSU IACUC-13-004 protocol. (A) 4mm defects were drilled into the parietal bone of adult male nude mice using high speed drill for LAMD implantation, (B) The PCL scaffold was implanted in the defect (C) the mice were anesthetized using isoflurane and (D) the surgical site was stapled with Michel clips.

4.3.4 Histological Staining

Following radiographic imaging calvaria were processed and stained as described previously.[14, 15] Briefly, the calvaria were harvested, fixed in 10% formalin for 24 hr,

decalcified in with 10% Ethylenediaminetetraacetic acid (EDTA) for three days and embedded into paraffin wax for sectioning. To evaluate bone regeneration, 10um sections were cut and stained with H&E and Masson's Tirchome (American MasterTech, Lodi- CA, Item # KTTRBPT) according to manufacturer's protocols (collagen appears pink and blue under H&E and Masson's Tirchome stains respectively). The sections were imaged using Olympus BX46 microscope.

4.3.5 *Ex vivo* Mineralization of Scaffolds

To confirm the *in vivo* mineralization of PCL scaffolds with the PC-miR-148b-SNP in the mice, the scaffolds were prepared as previously described in section 4.3.1. Instead, the scaffolds were submerged in stromal media for 4 or 12 weeks while exchanging the media every 3-4 days. The mineralization was quantified with Alizarin Red S stain as previously described by Qureshi et. al[10].

4.3.6 Statistical Analysis

All results were expressed as mean ± error. Data was analyzed with one way t-test. For all comparisons, a p-value < 0.05 was considered significant.

4.4 Results

4.4.1 Osteogenic Differentiation with Varying Concentrations of PC-miR-148b-SNP Conjugates

Prior to implantation of scaffolds with PC-miR-148b-SNP conjugates in mice, the optimal concentration of conjugates that is non-cytotoxic to hASCs and has the maximum differentiation potential was tested by exposing varying concentrations of conjugates to cells for 7 and 14 days.

ALPL is one of the early protein enzymes expressed during osteogenesis and is displayed on the extracellular portion of the plasma membrane, resulting in increased local concentration of

inorganic phosphate. The negative controls, Stromal media (SM) and SM+Flashed, exhibited minimal ALPL activity on the hASCs (Figure 4.3 A and E) while a trend, quantified in Figure 4.3 (I), was observed with increasing concentration of conjugates. The most significantly different ALPL production was seen between the 10ul photo and non-photoactivated conjugate (Figure 4.3 B and F). The normalized absorbance/No of hASCs ratio increased from $7.01 \times 10^5 \pm 7.20 \times 10^5$ to $2.3 \times 10^4 \pm 2.4 \times 10^5$ when activated with UV radiation ($p<0.05$; one-sample t-test). The ALPL absorbance of UV activated 0.60 nM and 1.20 nM of conjugate samples were not significantly different from each other ($p>0.05$; one-sample t-test) and lower than activated 0.12 nM conjugate sample due to a decrease in the number of viable cells. The higher concentrated samples (0.60 nM-1.20 nM) were more cytotoxic to the cells seen by the visible differences in the morphology (Figure 4.3 C, D, G and H) and decrease in the number of hASCs after 7 days.

A late stage of bone formation is the accretion of extracellular calcium deposits on ECM deposited by the osteoblasts. For this dosage dependence study, the calcium deposition was quantitatively and qualitatively measured by Alizarin Red S stain as hASCs were treated with varying concentrations of conjugates (Figure 4.4). The negative controls, Stromal media (SM) and SM+Flashed, had the least calcium deposition on hASCs (Figure 4.4 A and E). The calcification of hASCs increased sharply for the UV photoactivated 0.12 nM and 0.60 nM conjugate samples as the normalized absorbance/ No of hASCs ratio increased to $9.88 \times 10^6 \pm 1.26 \times 10^6$ and $9.80 \times 10^4 \pm 4.3 \times 10^7$ respectively. The 1.20 nM conjugate sample was cytotoxic to the cells and the lower number of hASCs resulted in the lower normalized absorbance/hASCs ratio. This was confirmed with the visual difference in the morphology of the hASCs with 1.20 nM conjugate sample (Figure 4.4 D and H). It can be concluded that up to 0.60 nM SNP can be used for the differentiation of hASCs as higher concentrations can have a deteriorating affect on

the morphology and the viability of cells. The recommended and optimum concentration of conjugates was 0.60 nM as it is noncytotoxic and has the maximum osteogenic differentiation potential.

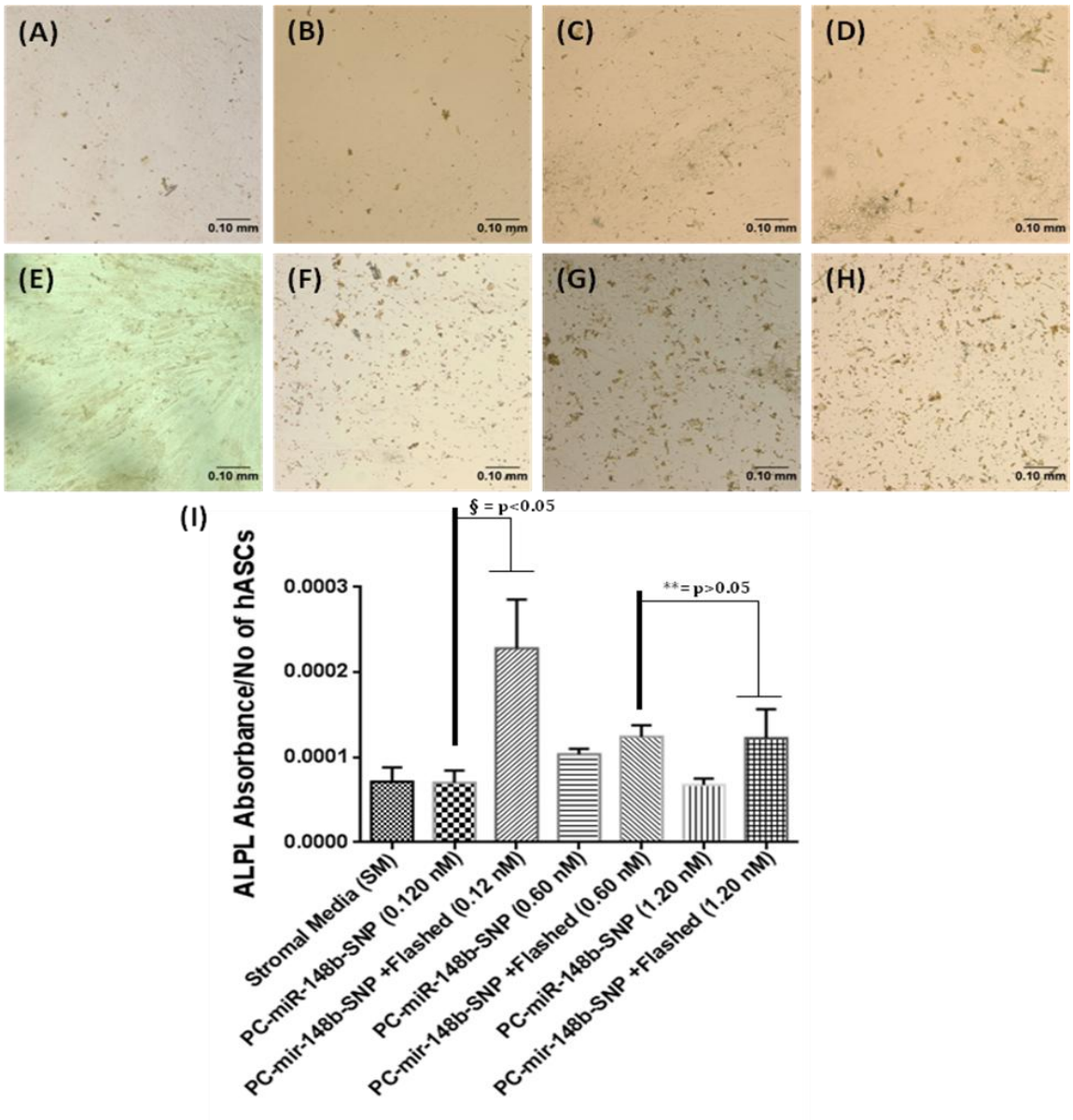

Figure 4.3. Alkaline phosphatase (ALPL) upregulation of hASC exposed to varying concentrations of Pc-miR-148b-SNP conjugates. (A) Stromal Media (B) 0.120nM, (C) 0.60 nM, (D) 1.20 nM, (E) hASCs+ Flashed, (F) 0.120 nM + Flashed, (G) 0.60 nM + Flashed, (H) 1.20 nM + Flashed and (I) Quantification of ALPL absorbance after 7 days. § denotes significantly different values ($p<0.05$; one-sample t-test) while ** denotes insignificantly different values ($p>0.05$; one-sample t-test).

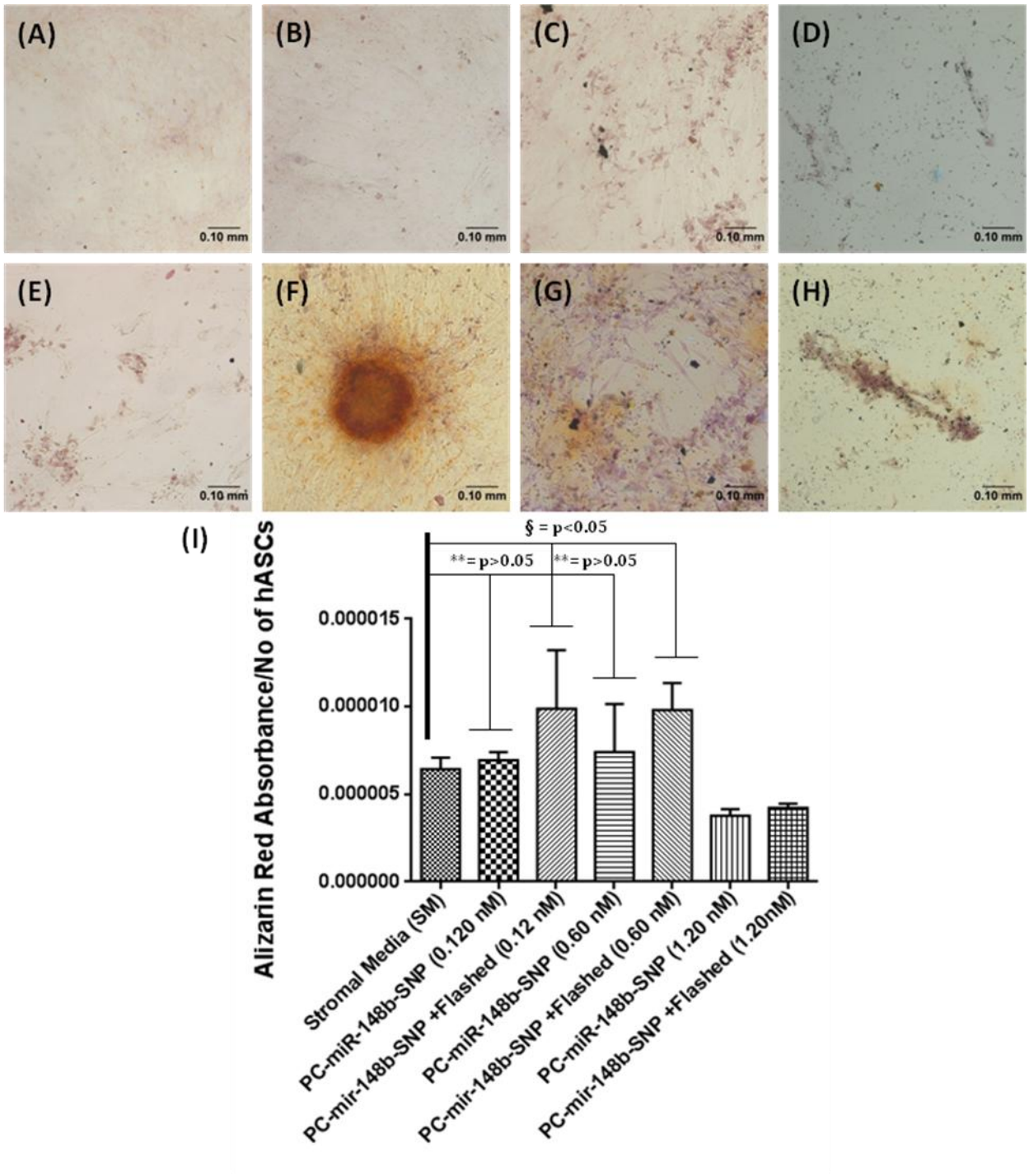

Figure 4.4. Mineralization of hASCs with Alizarin Red S stain. hASC exposed to varying concentrations of Pc-miR-148b-SNP conjugates. (A) stromal media control (B) 0.120nM, (C) 0.60 nM, (D) 1.20 nM, (E) stromal+ Flashed, (F) 0.120 nM + Flashed, (G) 0.60 nM + Flashed, (H) 1.20 nM + Flashed and (I) Quantification of Alizarin Red absorbance after 14 days. § denotes significantly different values ($p<0.05$; one-sample t-test) while ** denotes insignificantly different values ($p>0.05$; one-sample t-test)

4.4.2 μ-CT Imaging

The 2D and 3D reconstruction of images taken of mice heads by μ-CT showed closure of the defect after 4 and 12 weeks for the experimental and test control groups (Figure 4.5- A). As expected, in the negative controls the bone regeneration and hence the defect closure was minimal even after 12 weeks post implantation; corresponding to the percent healing values of 5.97%, 4.76% and 1.52 % for scaffold only, empty defect and scaffold+ miSpike-21mer respectively after 12 weeks. The positive controls with scaffold loaded with hASCs and maintained in stromal and osteogenic media for seven days prior to implantation had some bone regrowth. For scaffold+ hASCs, the percent closure of the defect was not significantly different between 4 to 12 weeks (the values changed from 4.5 ± 3.65 6.5 ± 0.80) while the *in vitro* osteogenic induction of the scaffolds in osteogenic media (DMEM, 10% FBS, 0.1 μM dexamethasone, 50 μM ascorbate-2-phosphate, 10 mM β-glycerophosphate, and 1% antibiotic) for 7 days prior to implantation increased the bone growth from 3.43 ± 1.22 to 13.7 ± 7.31 from 4 to 12 weeks. The percent bone regeneration increased for both the experimental groups between 4 to 12 weeks; the PC-miR-148b-SNP conjugate percentage increased from 3.83 ± 1.19 to 10.91 ± 5.45 while the percentage values for PC-miR-148b-SNP+UV increased from 6.54 ± 4.28 to 22.30 ± 4.93. The UV activation of the PC-miR148b-SNP conjugate released the miR-148b and differentiated the hASCs in the scaffolds but the percentage healing of the defect with photoactivated conjugates is lower than expected and can be further optimized to achieve higher closure of the defect. Also, the 12 weeks healing percentages of the experimental groups were not significantly different from each other. These *in vivo* results demonstrate a trend in the osteogenic differentiation of hASCs and formation of bone in the defect with the conjugates but the *in vivo* process of inducing osteogenic differentiation with these conjugates need to be

optimized to achieve higher percent closure of the defect. This will be achieved by increasing the number hASCs loaded to the scaffolds to 1.5 x 10^5 cells/scaffold, increasing the conjugate dosage and increasing the number of mice for each experimental group to improve the significance of the values.

We also observed the defect treated with non-photoactivated PC-miR148b-SNP conjugates to close to 10.91 ± 5.45% after 12 weeks and this can be reduced by proper handling of the scaffolds pre-implantation. For future surgeries, special care will be taken to minimize the light exposure during transporting the scaffold to surgery room and during the surgery to inhibit the release of miR-148b from the conjugates. As excess miRNA is added during the particle functionalization process, additional purification, to remove unbound PC-miR-148b, will very likely increase the differences in defect closure between photoactivated PC-miR-148b conjugates and non activated conjugates.

4.4.3 Histological Analysis

The mouse calvarium sections were decalcified with EDTA and the presence of collagen was studied with H&E and Masson's Trichrome stains. The images in Figure 4.6 track the changes in collagen lining across the defect between 4 and 12 weeks. Comparing the 4 and 12 weeks images, the pink stained collagen lining remained consistently thin and minimal in the negative controls; scaffold only, empty defect samples and scaffold+hASCs (Figure 4.6 1a-3a and 1b-3b). For positive controls, scaffold+ hASCs (OM), the collagen lining appeared visibly thicker and mineralized with purple stained bone marrow present in the new bone (Figure 4.6-4b). The greatest difference was seen between the photo and non-photoactivated PC-miR-148b-SNP conjugate samples. In the non-photoactivated sample, few strands of collagen fiber lining stretched across the defect site between the pre-existing calvarium but the mineralization is very

nominal (Figure 4.6-5a and 5b). For photoactivated PC-miR-148b-SNP conjugates, the collagen fiber lining can be seen thickening between 4 to 12 weeks (Figure 4.6-6a and 6b). The collagen lining thickened the most at 12 weeks and was of the same density and thicknesses as the pre-existing calvarium and the positive controls.

Similar trends were seen when the sections were stained with Masson's Trichrome. The intercellular fiber and collagen appear red and blue respectively. The negative control samples; scaffold only and empty defect samples, demonstrated the absence of collagen at the defect site (Figure 4.6-1c and 2c). Small blue stained collagen colonies were seen as the interface between the pre-existing bone and the defect site. Scaffold+hASCs samples show an increased presence of collagen at the interface but the lining does not span across the defect site. It was encouraging to see minimal closure/healing of the defect in these negative controls. The positive control group, scaffold+ hASCs (OM), showed an increased ossification greater than the pre-existing bone. After 12 weeks, the hASCs scaffolds mineralized completely due to osteogenic induction prior to implantation. The mineralized and ossified scaffolds had similar staining to the calvarium (Figure 4.6-4c). Differences in the amount of collagen and the mineralization of hASCs can be appreciated by comparing the stained sections of non-photoactivated and photoactivated PC-miR-148b-SNP conjugates (Figure 4.6-5c and 6c). The collagen strands thicken as the scaffolds mineralize with the photoactivation of conjugates.

The osteogenic differentiation of hASCs, with photo-released miR-148b, occurred in the scaffold and assisted in the closure of the defect. These transverse sections of the new bone with photoactivated PC-miR-148b-SNP conjugate show abundant amount of collagen present at the defect site . Mineralization of the new bone can also be appreciated with few colonies of dark purple bone marrow present in the thick collagen lining.

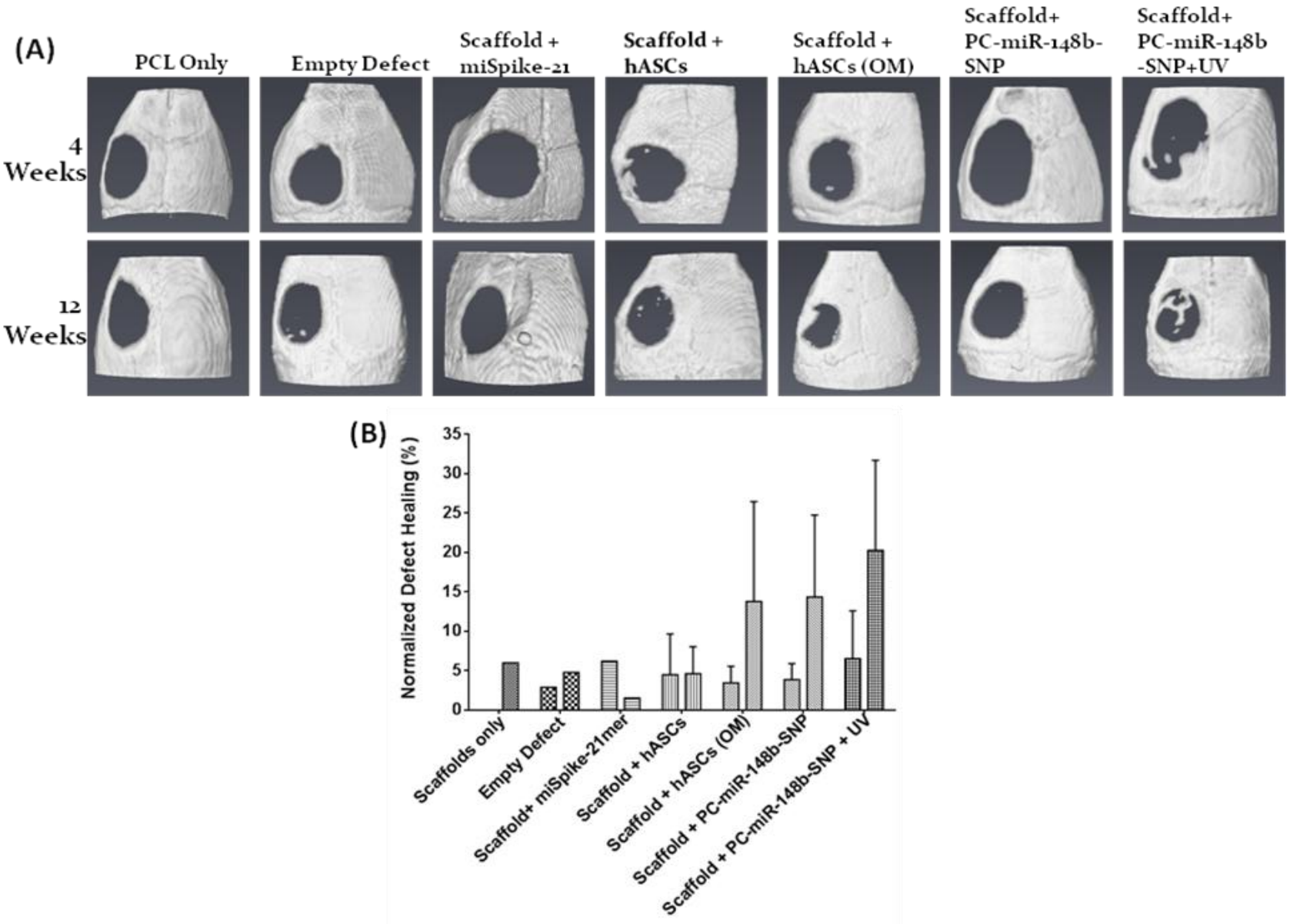

Figure 4.5. (A) 3D reconstructed images of 4mm calvarial size defects. The defect was imaged with μ-CT after sacrificing the mice 4 and 12 weeks post implantation of the scaffold with photo and non photo activated PC-miR-148b-SNP conjugates. (B) The healing/closure of the defect were quantified using Image J.

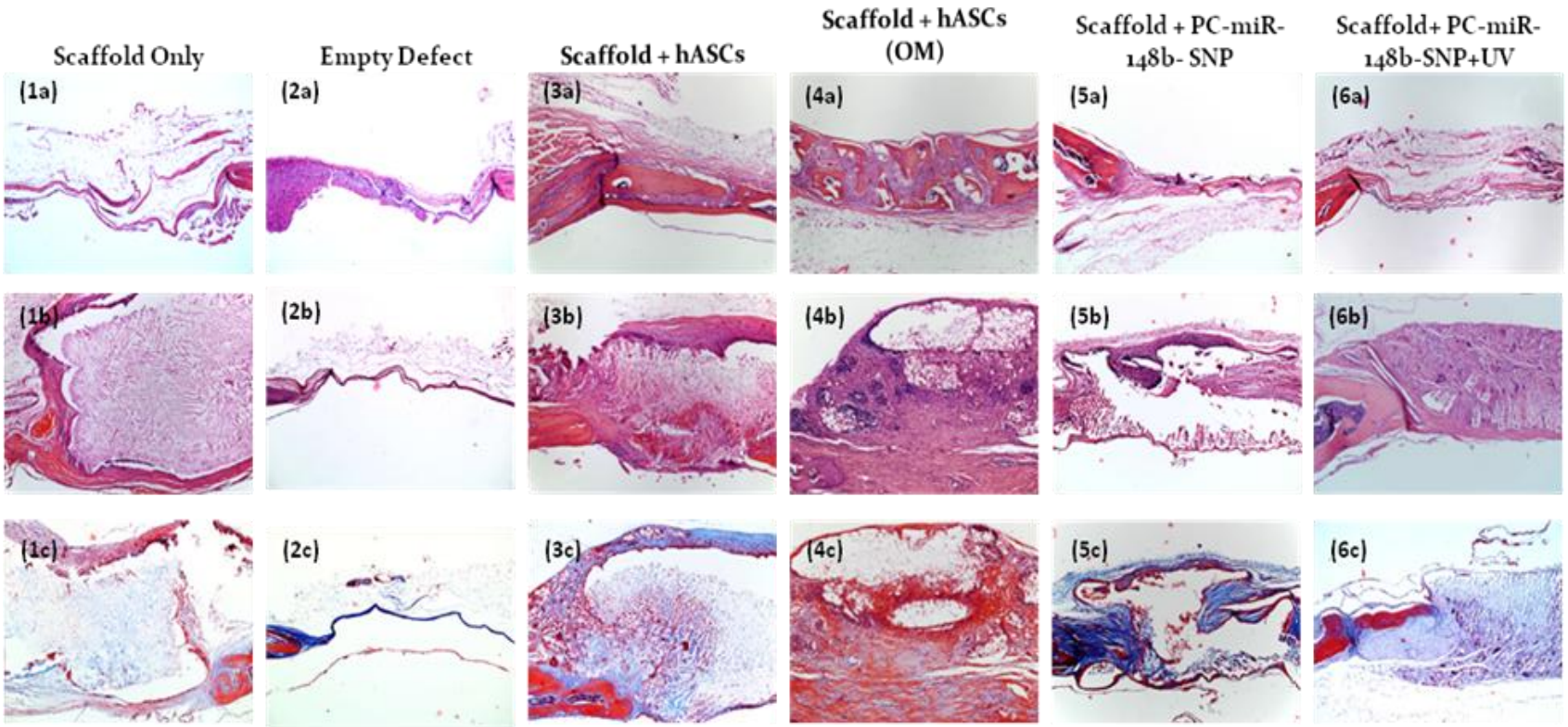

Figure 4.6. The mouse calvaria were decalcified, paraffin-embedded, sectioned and stained with (a) HE stain-4 weeks, (b) HE stain-12 weeks and (c) Masson's Trichrome- 12 weeks to study the presence of collagen. The collagen appears pink and blue with HE and Trichrome stain respectively. The images were taken with Olympus BX46 and magnification is 10x.

4.4.4 *Ex vivo* Mineralization of Scaffolds

The mineralization of scaffolds loaded with hASCs and conjugates was quantified with Alizarin Red stain after 4 weeks (Figure 4.7). During mineralization, osteoblasts produce extracellular calcium deposits, which are an indication of bone formation. The negative controls (scaffolds with hASCs and scaffolds with miSpike-21mer) induced minimal mineralization of the scaffolds but the positive control, scaffolds with hASCs in OM, showed a significantly higher mineralization (0.21 ± 0.008). The difference in the mineralization values between the non-photoactivated 0.12 nM and 0.60 nM of conjugate samples are not significantly different from each other. It was encouraging to observe that even with the addition of conjugate at a higher concentration, the conjugate remained inert and caged and prevented the mineralization of hASCs in the scaffolds. The mineralization of scaffolds increased to 0.14 ± 0.08 and 0.12 ± 0.003 for 0.60 nM and 0.12 nM conjugate samples respectively and the difference is statistically different from each other ($p<0.05$; one-sample t-test). The increase in mineralization was a result of increasing the conjugate concentration and the number of hASC to 1.5×10^5/scaffold. The statistically significant increase in mineralization of hASCs, with the addition of 0.60 nM of conjugate and higher cells, can potentially result in higher closure of the defect *in vivo.* We achieved 22.30 ± 4.93 percent closure of the CSD with 0.12 nM of activated conjugate but this percentage can potentially increase as higher concentration of conjugate and greater numbers of cells will mineralize the scaffold at a greater rate leading to an extended differentiation of hASCs to osteoblasts. Additionally, we can correlate these results to the scaffolds implanted *in vivo* providing further evidence for the mineralization of the scaffolds implanted in the defects of mouse calvarium.

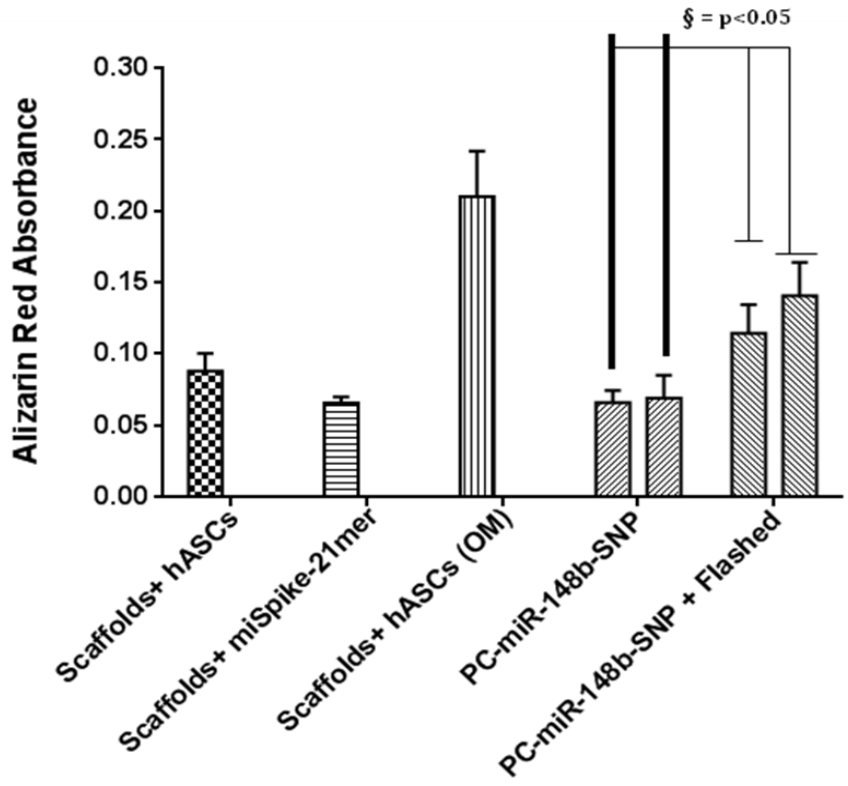

Figure 4.7. The mineralization of hASCs was quantified by staining cells with Alizarin Red. § denotes significantly different values ($p<0.05$; one-sample t-test)

4.5 Discussion

Targeted delivery and controlled release of oligonucleotide therapeutics *in vivo* are essential aspects of an ideal gene delivery vehicle.[21] Delivery systems providing spatial and temporal control have the potential to improve outcomes in surgical reconstruction and regenerative medicine by precise modulation of wound healing and tissue repair processes. This photoactivated technique, particularly when combined with human autologous progenitor cells, may result in a new regenerative medicine paradigm. Modulation of gene expression with miRNA is a promising technique for improving control of wound healing and tissue repair processes. Recent efforts to modulate the osteogenic differentiation of human adipose derived MSC (ASC) were conducted *in vitro* and demonstrated the upregulation of early and late stage

osteogenic markers, alkaline phosphatase, osteocalcin, RUNX2 and Alizarin red staining when photoactivated. In this *in vivo* study we analyzed the healing of the critical size defect on the mouse calvarium with a particle system for delivery of a truncated miR-148b mimic[10]. We tested this technology on a well described critical size defect model[14] and observed interesting results. The 4 mm defect was drilled just off the sagittal midline to expose the left parietal bone and was healed with PCL scaffolds loaded with hASCs that were transfected with PC-miR-148b-SNP conjugates. PCL was chosen for this application as it has previously been demonstrated to have little impact on hASC differentiation.[22] The defect healed with the photoactivated conjugates while the control groups had minimal healing and remained opened even after 12 weeks, further verifying the model and the size of the non-healing defect. A progression was observed in the percent closure of the defect between 4 and 12 in all the samples but the sample size needs to be increased to conduct statistical analysis on the photoavtivated and non photoavtivated samples. The histological analysis on the decalcified calvarium sections also demonstrated the thickening of the collagen fiber lining, across the defect, when the photoavtivated conjugates were use. The collagen stained with HE and Masson's Trichome was on the same thickness as the pre-existing calvarium and the new bone was infused with older bone in the photoavtivated conjugates samples after 12 weeks.

At 12 weeks, the percentage closure of the photoavtivated samples was not statistically different from the non photoavtivated samples and measures can be taken to improve the healing percentages. The combination of increasing the cell number and adding higher dosage of more purified conjugate samples can very likely increase the percent healing for photoactivated PC-miR-148b conjugates while decreasing the percentages for non activated conjugates. This is hypothesized based on the results of *ex vivo* mineralization of scaffolds experiment. The Alizarin

Red absorbance increased from 0.12 ± 0.003 to 0.14 ± 0.08 ($p<0.05$; one-sample t-test) with the addition of higher dosage of conjugates. We believe that these improvements will also translate in our *in vivo* model and increase the closure of the defect to higher percentages to ones we achieved with 10 ul of conjugate and 1 x 10^5 cells.

To translate this technology into a clinical setting, better matrices or scaffolding materials need to be analyzed that have better activation of PC-miR- 148-SNP conjugate. The penetration depth of light across the scaffold is of major concern as it plays a critical role photoactivation of conjugates for the differentiation of hASCs.

4.6 References

1. Pfeilschifter, J. and G.R. Mundy, *Modulation of type beta transforming growth factor activity in bone cultures by osteotropic hormones.* Proceedings of the National Academy of Sciences, 1987. **84**(7): p. 2024-2028.

2. Mohan S, B.D.J., *Modern Concepts of Insulin-Like Growth Factors*1991, New York: Elsevier. 169–184.

3. Baron R, V.A., Horowitz M., *In: Bone and Mineral Research.*, ed. e. Peck W A1984, New York: Elsevier. 175–243.

4. Rodan, G.A. and T.J. Martin, *Role of osteoblasts in hormonal control of bone resorption—a hypothesis.* Calcified Tissue International, 1981. **33**(1): p. 349-351.

5. Schoolmeesters, A., et al., *Functional Profiling Reveals Critical Role for miRNA in Differentiation of Human Mesenchymal Stem Cells.* Plos One, 2009. **4**(5): p. 9.

6. Luzi, E., et al., *Osteogenic differentiation of human adipose tissue-derived stem cells is modulated by the miR-26a targeting of the SMAD1 transcription factor.* Journal of Bone and Mineral Research, 2008. **23**(2): p. 287-295.

7. Mizuno, Y., et al., *miR-125b inhibits osteoblastic differentiation by down-regulation of cell proliferation.* Biochemical and Biophysical Research Communications, 2008. **368**(2): p. 267-272.

8. Fang, T.D., et al., *Guided tissue regeneration enhances bone formation in a rat model of failed osteogenesis.* Plastic and reconstructive surgery, 2006. **117**(4): p. 1177-1185.

9. Gimble, J. and F. Guilak, *Adipose-derived adult stem cells: isolation, characterization, and differentiation potential.* Cytotherapy, 2003. **5**(5): p. 362-369.

10. Qureshi, A.T., et al., *miR-148b–Nanoparticle conjugates for light mediated osteogenesis of human adipose stromal/stem cells.* Biomaterials, 2013.

11. Ogawa, R., et al., *Osteogenic and chondrogenic differentiation by adipose-derived stem cells harvested from GFP transgenic mice.* Biochemical and Biophysical Research Communications, 2004. **313**(4): p. 871-877.

12. Stemberger, S., et al., *Mesenchymal Stem Cells in a Transgenic Mouse Model of Multiple System Atrophy: Immunomodulation and Neuroprotection.* PLoS One, 2011. **6**(5).

13. De Souza, R.L., et al., *Non-invasive axial loading of mouse tibiae increases cortical bone fori-nation and modifies trabecular organization: A new model to study cortical and cancellous compartments in a single loaded element.* Bone, 2005. **37**(6): p. 810-818.

14. Levi, B., et al., *Human adipose derived stromal cells heal critical size mouse calvarial defects.* PLoS One, 2010. **5**(6): p. e11177.

15. Wan, D.C., et al., *Noggin suppression enhances in vitro osteogenesis and accelerates in vivo bone formation.* Journal of Biological Chemistry, 2007. **282**(36): p. 26450-26459.

16. Mendes, S., et al., *Bone tissue-engineered implants using human bone marrow stromal cells: effect of culture conditions and donor age.* Tissue Engineering, 2002. **8**(6): p. 911-920.

17. Harris, S., et al., *Effects of transforming growth factor β on bone nodule formation and expression of bone morphogenetic protein 2, osteocalcin, osteopontin, alkaline phosphatase, and type I collagen mRNA in long-term cultures of fetal rat calvarial osteoblasts.* Journal of Bone and Mineral Research, 2009. **9**(6): p. 855-863.

18. Shea, L.D., et al., *Engineered bone development from a pre-osteoblast cell line on three-dimensional scaffolds.* Tissue Engineering, 2000. **6**(6): p. 605-617.

19. Levi, B., et al., *Dura Mater Stimulates Human Adipose-Derived Stromal Cells to Undergo Bone Formation in Mouse Calvarial Defects.* Stem Cells, 2011. **29**(8): p. 1241-1255.

20. Qureshi, A.T., et al., *Antimicrobial biocompatible bioscaffolds for orthopaedic implants.* Journal of Tissue Engineering and Regenerative Medicine, 2012.

21. Roth, C.M., *Molecular and cellular barriers limiting the effectiveness of antisense oligonucleotides.* Biophysical Journal, 2005. **89**(4): p. 2286-2295.

22. Zanetti, A., et al., *Characterization of novel akermanite: poly-ε-caprolactone scaffolds for human adipose-derived stem cells bone tissue engineering.* Journal of Tissue Engineering and Regenerative Medicine, 2012.

Chapter 5. Conclusions and Future Work

Targeted delivery and controlled release of oligonucleotide therapeutics *in vivo* are essential aspects of an ideal gene delivery vehicle.[1] Delivery systems providing spatial and temporal control have the potential to improve outcomes in surgical reconstruction and regenerative medicine by precise modulation of wound healing and tissue repair processes. This technique, particularly when combined with human autologous progenitor cells can result in a new regenerative medicine paradigm. Modulation of gene expression with microRNA (miRNA) is a promising technique for improving control of wound healing and tissue repair processes.[2] miRNAs are short, non-coding RNA's involved in post-transcriptional gene regulation. MicroRNA's utilized in modulating the differentiation of autologous, mesenchymal stromal/stem cells (MSC) are attractive as therapeutic modalities for regenerative medicine. Directing the osteogenic differentiation of these progenitors is of particular interest in the design of therapies for critical size bone defects, spinal fusion and skeletal reconstruction.

5.1 Red-shifting the Photoactivation of Conjugates

In future, nanoplasmonic particles as light activated gene delivery vehicles to provide improved spatial and temporal modulation of wound repair can be explored. The results in Chapter 2 and Chapter 3 demonstrate the modulation of osteogenic differentiation of human adipose derived MSC (ASC) both *in vitro* and *in vivo* using a murine critical sized defect model. A particle system for delivery of a truncated miR-148b mimic was developed, and demonstrated to be capable of upregulating the early and late stage osteogenic markers, alkaline phosphatase, osteocalcin, RUNX2 and Alizarin red staining when photoactivated.[3] While these studies demonstrate the potential of light-regulated gene delivery for improving the spatial and temporal modulation of cell behavior, the application of this technology is limited by the narrow excitation

window in the UV region (~365nm). The visible and nIR activated nanoplasmonic miRNA delivery (vNAMD) system proposed herein is an improved gene delivery vector providing greater temporal and spatial control over the activation of miRNA based differentiation (Figure 5.1). This photo-activated gene delivery system is composed of a metallic nanoparticle core or shell with a photo-absorbing element and a photocleavable miRNA payload. The potential benefits of noble metal nanoparticles (NP) in delivery applications include readily tunable morphology, ease of bulk synthesis, large surface area-to-volume ratios and robust functionalization chemistries. Additionally, metal nanoparticles fulfill the core requirements as drug delivery vehicles by offering high-density surface ligand attachment and facile transmembrane delivery.[4]

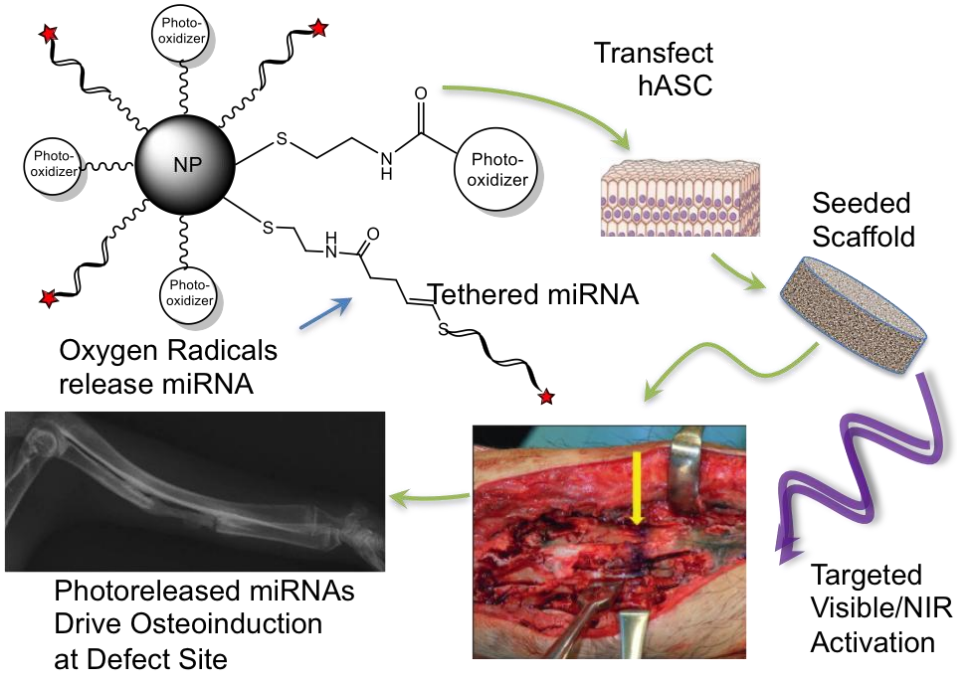

Figure 5.1 Overview of potential clinical implementation of visible and nIR activated nanoplasmonic miRNA delivery (vNAMD) system. Injection of LAMD in critical bone defects, followed by targeted photoactivation induces differentiation at select sites, with minimal side effects such as heterotopic ossification.

The particle morphology and composition can be tuned such that the localized surface plasmon resonance (LSPR) peak overlaps with the excitation maxima of the photo-responsive moiety in the payload resulting in photon energy specificity and high quantum efficiency for initiating cleavage. Previous studies have described both thermal and non-thermal components of plasmon mediated catalysis which can increase reaction rates by 2-3 orders of magnitude [5]. The non-thermal component is likely related to intense electrical fields in the oscillating surface plasmon region interacting with ionic molecules thus reducing the activation energy of the reaction.[5] Metal enhanced fluorescence has been described with silver nanostructures, wherein a resonance state or coupled photon is shared between a photoactive molecule and the metal nanomaterial resulting in more efficient photoconversion.[6] In the case of the vNAMD these quantum mechanical surface plasmon events could result in significantly lowering the required photon flux and red-shifting the activation spectra, providing better tissue penetration, and reducing the photo-damage by transiting photons.

A new photocleavable linking strategy for nucleic acids exploiting singlet oxygen cleavage of carbon-carbon bonds can be evaluated for visible and nIR range photomodulated payload release. In the proposed strategy commercially available photooxidizing compounds (used in PDT) with narrow excitation spectra, in the visible and nIR range, will be coupled to the nanoplasmonic metal particle via simple EDC chemistry with cysteamine self-assembled functional groups on the particle surface. The particle will be back filled with a thiolated miRNA payload containing an olefin functionality (Figure 5.2). This electron rich carbon–carbon double bond is amenable to attack from the singlet oxygen produced via photooxidizer excitation.[7, 8] Using photooxidizing compounds, with discrete visible or nIR range activation energies, as the cleavage initiator allows multiple vNAMD to be developed with non-

overlapping excitation spectra. These vNAMD would allow clinicians to deliver several sequences of miRNA at the same time and activate them independently, both temporally and spatially, via narrow band or coherent light sources. This would allow progenitor cells in the same tissue volume to be directed into multiple lineages, allowing the development of complex tissues.

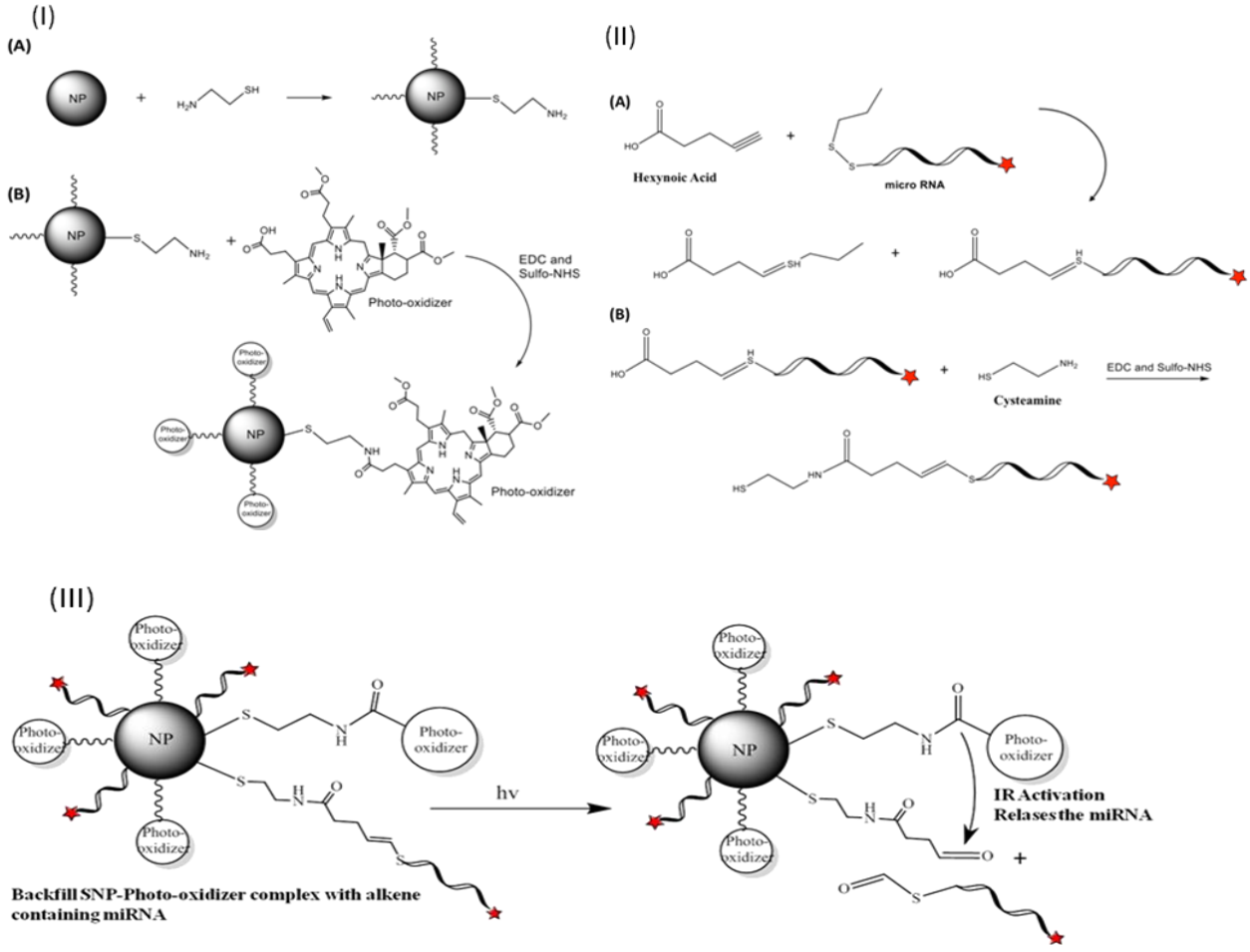

Figure 5.2. (I) Scheme for the functionalization of nanoparticles with porphyrin (Verteporfin). (II) The internal olefin cleavage site will be introduced via a base catalyzed Michael addition reaction between the 3' disulphide and hexynoic acid. The miRNA mimic construct with olefin group will then be coupled to the particle via EDC/NHS linkage with a self-assembled cystamine layer. (III) Diagram of vNAMD with red-shifted photoactivation (690nm) mechanism using singlet oxygen produced from a photosensitizer to cleave an electron rich alkene bond on the miRNA payload.

The vNAMD platform possesses several unique advantages compared to the few previously described photoresponsive oligonucleotide delivery systems: 1) the miRNA payload can be activated with focused laser precision allowing activity only in the area of the tissue defect, and 2) because miRNA are labile, activity is transient resulting in pathway regulation only in the critical early stages of cell differentiation, 3) the vNAMD is photoresponsive in the visible and nIR range. This provides greater tissue penetration and reduced photon induced tissue damage compared to caging strategies utilizing UV photons. Additionally, as the miRNA will only be transfected efficiently when bound to the particle, miRNA from vNAMD activated in the intercellular space will have little impact on surrounding tissue. This represents a paradigm shift from current methods of delivering osteogenic compounds such as diffusible BMP or BMP gene delivery where there is little spatial or temporal control of expression.

5.2 Scaffold Alternates to PCL

PCL served as the matrix to hold the hASCs endocytosed with the PC-miR-48b-SNP conjugates during the *in vivo* study highlighted in Chapter 4. The penetration depth of light across the scaffold is of major concern as it plays a critical role photoactivation of conjugates for the differentiation of hASCs. PCL is a very dense material and the even at 1 mm thickness the light penetration is minimal. To achieve the best photo cleavage of the conjugates and allow this technology to transfer into clinical trials, a better matrix needs to be selected that can be loaded with hASCs, injected with conjugates and photoactivated with UV or NIR radiation.

We are working on few hydrogel based polymer systems that show better penetration depth comparatively. Matrigel, a BD Biosciences marketed product is a gelatinous protein mixture secreted by Engelbreth-Holm-Swarm (EHS) mouse sarcoma cells. Chilled Matrigel (4 °C) exist as liquid and when incubated at 37 °C (body temperature) the Matrigel proteins self-

assembles and gels into hydrogel. Traditionally it has been used as a screen drug molecule and is added to cells, morphological changes are observed.

We stained the Matrigel with CMNB-caged carboxyfluorescein (5-carboxyfluorescein-bis-(5-carboxymethoxy-2-nitrobenzyl) ether, alanine-carboxamide, succinimidyl ester) and uncaged with UV for 5 minutes (206nm). Figure 5.3 shows the ability of Matrigel to incubate a caged molecule that can be completely excited with UV radiation. The light penetration of Matrigel is also solved as the activated Matrigel appeared green (uncaged) while the uncaged Matrigel appeared blue (the color of the excited light). Studies are underway to analyze the ability of Matrigel to activate the PC-miR-148b-SNP conjugates and drive differentiation of hASCs by upregulating osteogenic markers *(ALPL, OCN and RunX2*). Also PC-miR-148b-SNP conjugates have been implanted on the mice using the CSD model as described in Chapter 4.

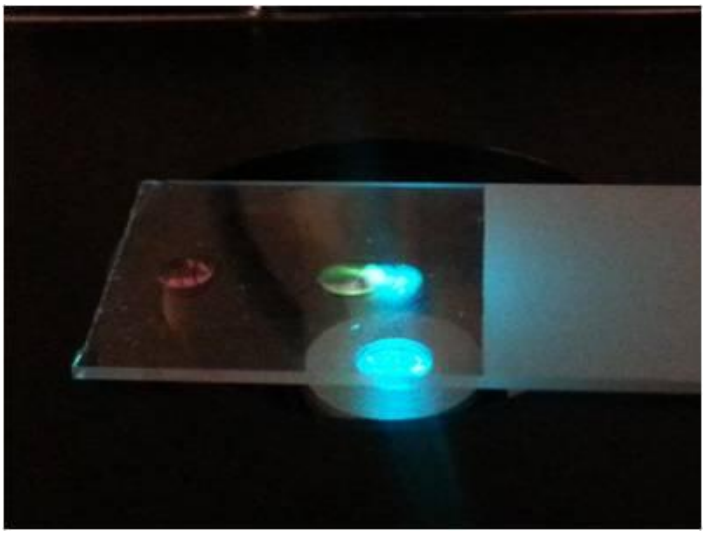

Figure 5.3. Caged-FITC labeled Matrigel, when activated, completely turns green when imaged under a microscope.

5.3 Improve *in vivo* Results to Improve Healing of CSD

In Chapter 4, the UV activation of the PC-miR148b-SNP conjugate released the miR-148b and differentiated the hASCs in the scaffolds but the percentage healing of the defect with

photoactivated conjugates is lower than expected and can be further optimized to achieve higher closure of the defect. Also, the 12 weeks healing percentages of the experimental groups were not significantly different from each other. These *in vivo* results demonstrate a trend in the osteogenic differentiation of hASCs and formation of bone in the defect with the conjugates but the *in vivo* process of inducing osteogenic differentiation with these conjugates need to be optimized to achieve higher percent closure of the defect with the photoactivated conjugates. This will be achieved by increasing the number hASCs loaded to the scaffolds to 1.5×10^5 cells/scaffold and increasing the number of mice for each experimental group to calculate the significant values.

We also observed the defect treated with non photoactivated PC-miR148b-SNP conjugates to close to $10.91 \pm 5.45\%$ after 12 weeks and this can be reduced by proper handling of the scaffolds pre-implantation. For the next round of surgeries, special care was taken to minimize the light exposure during transporting the scaffold to surgery room and during the surgery to inhibit the release of miR-148b from the conjugates. The combination of increasing the cell number and additional purification, to remove the floating PC-miR-148b during the functionlization step, will very likely increase the percent healing for photoactivated PC-miR-148b conjugates while decreasing the percentages for non activated conjugates.

5.4 References

1. Roth, C.M., *Molecular and cellular barriers limiting the effectiveness of antisense oligonucleotides.* Biophysical Journal, 2005. **89**(4): p. 2286-2295.

2. Rhim, C., et al., *Effect of MicroRNA Modulation on Bioartificial Muscle Function.* Tissue Engineering Part A, 2010: p. 3589-3597.

3. Qureshi, A.T., et al., *miR-148b–Nanoparticle conjugates for light mediated osteogenesis of human adipose stromal/stem cells.* Biomaterials, 2013. **34**(31): p. 7799-7810.

4. Brown, P.K., et al., *Silver nanoscale antisense drug delivery system for photoactivated gene silencing.* ACS Nano, 2013. **7**(4): p. 2948-59.

5. Hung, W.H., et al., *Plasmon Resonant Enhancement of Carbon Monoxide Catalysis.* Nano Letters, 2010. **10**(4): p. 1314-1318.

6. Chowdhury, M.H., et al., *Metal-enhanced chemiluminescence: Radiating plasmons generated from chemically induced electronic excited states.* Applied Physics Letters, 2006. **88**: p. 173104.

7. Ruebner, A., et al., *A cyclodextrin dimer with a photocleavable linker as a possible carrier for the photosensitizer in photodynamic tumor therapy.* Proceedings of the National Academy of Sciences, 1999. **96**(26): p. 14692-14693.

8. Bio, M., et al., *Site-specific and far-red-light-activatable prodrug of combretastatin a-4 using photo-unclick chemistry.* J Med Chem, 2013. **56**(10): p. 3936-42.

Appendix A: Approval from Journal of Tissue Engineering and Regenerative Medicne

JOHN WILEY AND SONS LICENSE
TERMS AND CONDITIONS

Oct 23, 2013

This is a License Agreement between Ammar T Qureshi ("You") and John Wiley and Sons ("John Wiley and Sons") provided by Copyright Clearance Center ("CCC"). The license consists of your order details, the terms and conditions provided by John Wiley and Sons, and the payment terms and conditions.

All payments must be made in full to CCC. For payment instructions, please see information listed at the bottom of this form.

License Number	3254580376512
License date	Oct 23, 2013
Licensed content publisher	John Wiley and Sons
Licensed content publication	Journal of Tissue Engineering and Regenerative Medicine
Licensed content title	Antimicrobial biocompatible bioscaffolds for orthopaedic implants
Licensed copyright line	Copyright © 2012 John Wiley & Sons, Ltd.
Licensed content author	Ammar T. Qureshi,Lekeith Terrell,W. Todd Monroe,Vinod Dasa,Marlene E. Janes,Jeffrey M. Gimble,Daniel J. Hayes
Licensed content date	Jun 15, 2012
Start page	n/a
End page	n/a
Type of use	I don't see my intended use
Special requirements	I want to use my publication as a chapter in my PhD dissertation. Thanks Ammar Qureshi
Total	0.00 USD
Terms and Conditions	

TERMS AND CONDITIONS

This copyrighted material is owned by or exclusively licensed to John Wiley & Sons, Inc. or one of its group companies (each a "Wiley Company") or a society for whom a Wiley Company has exclusive publishing rights in relation to a particular journal (collectively "WILEY"). By clicking "accept" in connection with completing this licensing transaction, you agree that the following terms and conditions apply to this transaction (along with the billing and payment terms and conditions established by the Copyright Clearance Center Inc., ("CCC's Billing and Payment terms and conditions"), at the time that you opened your RightsLink account (these are available at any time at http://myaccount.copyright.com).

Terms and Conditions

1. The materials you have requested permission to reproduce (the "Materials") are protected by copyright.

2.You are hereby granted a personal, non-exclusive, non-sublicensable, non-transferable, worldwide, limited license to reproduce the Materials for the purpose specified in the licensing process. This license is for a one-time use only with a maximum distribution equal to the number that you identified in the licensing process. Any form of republication granted by this license must be completed within two years of the date of the grant of this license (although copies prepared before may be distributed thereafter). The Materials shall not be used in any other manner or for any other purpose. Permission is granted subject to an appropriate acknowledgement given to the author, title of the material/book/journal and the publisher. You shall also duplicate the copyright notice that appears in the Wiley publication in your use of the Material. Permission is also granted on the understanding that nowhere in the text is a previously published source acknowledged for all or part of this Material. Any third party material is expressly excluded from this permission.

3. With respect to the Materials, all rights are reserved. Except as expressly granted by the terms of the license, no part of the Materials may be copied, modified, adapted (except for minor reformatting required by the new Publication), translated, reproduced, transferred or distributed, in any form or by any means, and no derivative works may be made based on the Materials without the prior permission of the respective copyright owner. You may not alter, remove or suppress in any manner any copyright, trademark or other notices displayed by the Materials. You may not license, rent, sell, loan, lease, pledge, offer as security, transfer or assign the Materials, or any of the rights granted to you hereunder to any other person.

4. The Materials and all of the intellectual property rights therein shall at all times remain the exclusive property of John Wiley & Sons Inc or one of its related companies (WILEY) or their respective licensors, and your interest therein is only that of having possession of and the right to reproduce the Materials pursuant to Section 2 herein during the continuance of this Agreement. You agree that you own no right, title or interest in or to the Materials or any of the intellectual property rights therein. You shall have no rights hereunder other than the license as provided for above in Section 2. No right, license or interest to any trademark, trade name, service mark or other branding ("Marks") of WILEY or its licensors is granted hereunder, and you agree that you shall not assert any such right, license or interest with respect thereto.

5. NEITHER WILEY NOR ITS LICENSORS MAKES ANY WARRANTY OR REPRESENTATION OF ANY KIND TO YOU OR ANY THIRD PARTY, EXPRESS, IMPLIED OR STATUTORY, WITH RESPECT TO THE MATERIALS OR THE ACCURACY OF ANY INFORMATION CONTAINED IN THE MATERIALS, INCLUDING, WITHOUT LIMITATION, ANY IMPLIED WARRANTY OF MERCHANTABILITY, ACCURACY, SATISFACTORY QUALITY, FITNESS FOR A PARTICULAR PURPOSE, USABILITY, INTEGRATION OR NON-INFRINGEMENT AND ALL SUCH WARRANTIES ARE HEREBY EXCLUDED BY WILEY AND ITS LICENSORS AND WAIVED BY YOU.

6. WILEY shall have the right to terminate this Agreement immediately upon breach of this Agreement by you.

7. You shall indemnify, defend and hold harmless WILEY, its Licensors and their respective directors, officers, agents and employees, from and against any actual or threatened claims, demands, causes of action or proceedings arising from any breach of this Agreement by you.

8. IN NO EVENT SHALL WILEY OR ITS LICENSORS BE LIABLE TO YOU OR ANY OTHER PARTY OR ANY OTHER PERSON OR ENTITY FOR ANY SPECIAL, CONSEQUENTIAL, INCIDENTAL, INDIRECT, EXEMPLARY OR PUNITIVE DAMAGES, HOWEVER CAUSED, ARISING OUT OF OR IN CONNECTION WITH THE DOWNLOADING, PROVISIONING, VIEWING OR USE OF THE MATERIALS REGARDLESS OF THE FORM OF ACTION, WHETHER FOR BREACH OF CONTRACT, BREACH OF WARRANTY, TORT, NEGLIGENCE, INFRINGEMENT OR OTHERWISE (INCLUDING, WITHOUT LIMITATION, DAMAGES BASED ON LOSS OF PROFITS, DATA, FILES, USE, BUSINESS OPPORTUNITY OR CLAIMS OF THIRD PARTIES), AND WHETHER OR NOT THE PARTY HAS BEEN ADVISED OF THE POSSIBILITY OF SUCH DAMAGES. THIS LIMITATION SHALL APPLY NOTWITHSTANDING ANY FAILURE OF ESSENTIAL PURPOSE OF ANY LIMITED REMEDY PROVIDED HEREIN.

9. Should any provision of this Agreement be held by a court of competent jurisdiction to be illegal, invalid, or unenforceable, that provision shall be deemed amended to achieve as nearly as possible the same economic effect as the original provision, and the legality, validity and enforceability of the remaining provisions of this Agreement shall not be affected or impaired thereby.

10. The failure of either party to enforce any term or condition of this Agreement shall not constitute a waiver of either party's right to enforce each and every term and condition of this Agreement. No breach under this agreement shall be deemed waived or excused by either party unless such waiver or consent is in writing signed by the party granting such waiver or consent. The waiver by or consent of a party to a breach of any provision of this Agreement shall not operate or be construed as a waiver of or consent to any other or subsequent breach by such other party.

11. This Agreement may not be assigned (including by operation of law or otherwise) by you without WILEY's prior written consent.

12. Any fee required for this permission shall be non-refundable after thirty (30) days from receipt

13. These terms and conditions together with CCC's Billing and Payment terms and conditions (which are incorporated herein) form the entire agreement between you and WILEY concerning this licensing transaction and (in the absence of fraud) supersedes all prior agreements and representations of the parties, oral or written. This Agreement may not be amended except in writing signed by both parties. This Agreement shall be binding upon and inure to the benefit of the parties' successors, legal representatives, and authorized assigns.

14. In the event of any conflict between your obligations established by these terms and conditions and those established by CCC's Billing and Payment terms and conditions, these terms and conditions shall prevail.

15. WILEY expressly reserves all rights not specifically granted in the combination of (i) the license details provided by you and accepted in the course of this licensing transaction, (ii) these terms and conditions and (iii) CCC's Billing and Payment terms and conditions.

16. This Agreement will be void if the Type of Use, Format, Circulation, or Requestor Type was misrepresented during the licensing process.

17. This Agreement shall be governed by and construed in accordance with the laws of the State of New York, USA, without regards to such state's conflict of law rules. Any legal action, suit or proceeding arising out of or relating to these Terms and Conditions or the breach thereof shall be instituted in a court of competent jurisdiction in New York County in the State of New York in the United States of America and each party hereby consents and submits to the personal jurisdiction of such court, waives any objection to venue in such court and consents to service of process by registered or certified mail, return receipt requested, at the last known address of such party.

Wiley Open Access Terms and Conditions

Wiley publishes Open Access articles in both its Wiley Open Access Journals program [http://www.wileyopenaccess.com/view/index.html] and as Online Open articles in its subscription journals. The majority of Wiley Open Access Journals have adopted the Creative Commons Attribution License (CC BY) which permits the unrestricted use, distribution, reproduction, adaptation and commercial exploitation of the article in any medium. No permission is required to use the article in this way provided that the article is properly cited and other license terms are observed. A small number of Wiley Open Access journals have retained the Creative Commons Attribution Non Commercial License (CC BY-NC), which permits use, distribution and reproduction in any medium, provided the original work is properly cited and is not used for commercial purposes.

Online Open articles - Authors selecting Online Open are, unless particular exceptions apply, offered a choice of Creative Commons licenses. They may therefore select from the CC BY, the CC BY-NC and the Attribution-NoDerivatives (CC BY-NC-ND). The CC BY-NC-ND is more restrictive than the CC BY-NC as it does not permit adaptations or modifications without rights holder consent.

Wiley Open Access articles are protected by copyright and are posted to repositories and websites in accordance with the terms of the applicable Creative Commons license referenced on the article. At the time of deposit, Wiley Open Access articles include all changes made during peer review, copyediting, and publishing. Repositories and websites that host the article are responsible for incorporating any publisher-supplied amendments or retractions issued subsequently.
Wiley Open Access articles are also available without charge on Wiley's publishing platform, **Wiley Online Library** or any successor sites.

Appendix B: Approval from Journal of Biomaterials

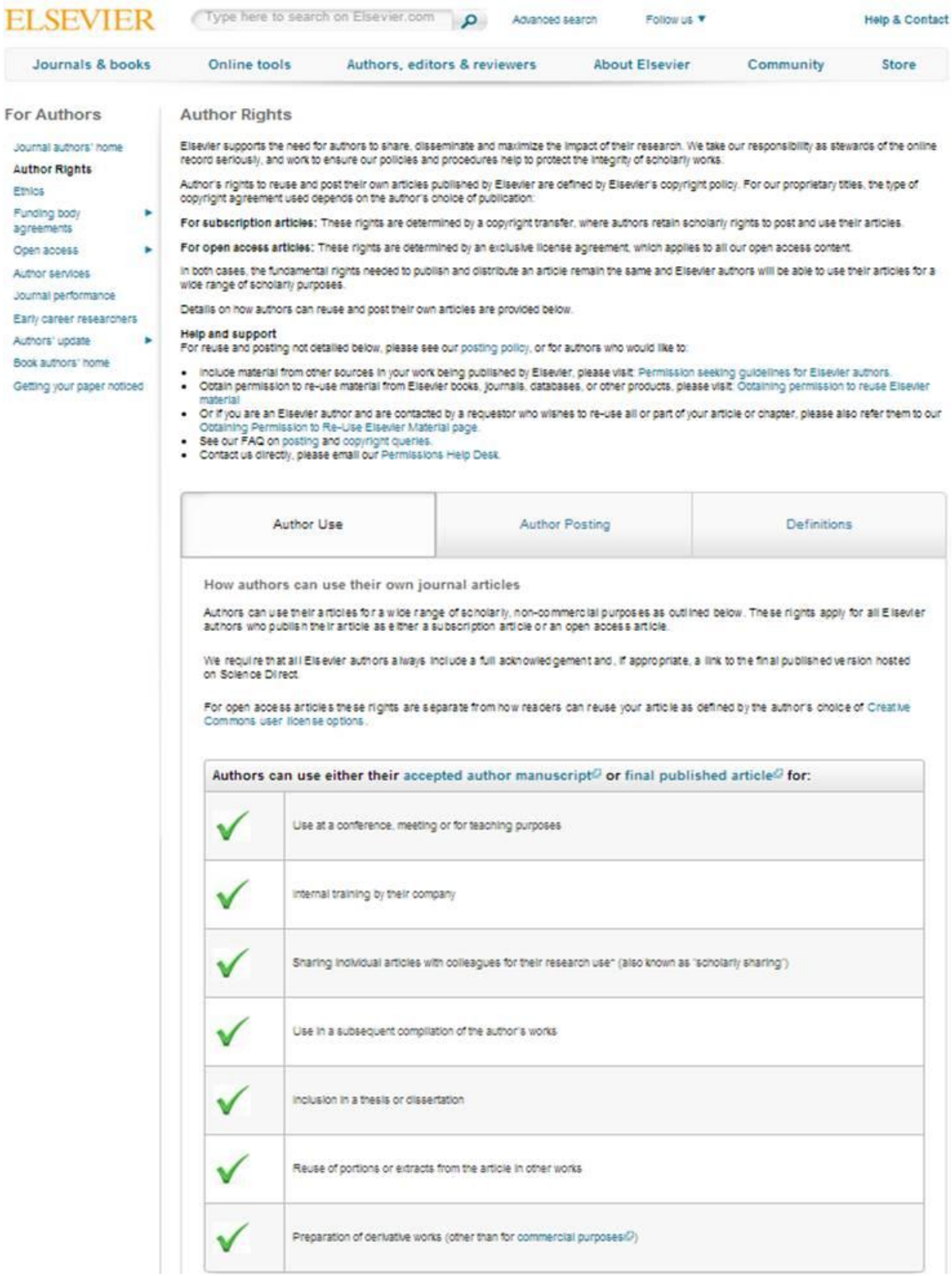

ELSEVIER

Type here to search on Elsevier.com

Advanced search Follow us ▼ Help & Contact

Journals & books | Online tools | Authors, editors & reviewers | About Elsevier | Community | Store

For Authors

- Journal authors' home
- **Author Rights**
- Ethics
- Funding body agreements ▸
- Open access ▸
- Author services
- Journal performance
- Early career researchers
- Authors' update ▸
- Book authors' home
- Getting your paper noticed

Author Rights

Elsevier supports the need for authors to share, disseminate and maximize the impact of their research. We take our responsibility as stewards of the online record seriously, and work to ensure our policies and procedures help to protect the integrity of scholarly works.

Author's rights to reuse and post their own articles published by Elsevier are defined by Elsevier's copyright policy. For our proprietary titles, the type of copyright agreement used depends on the author's choice of publication:

For subscription articles: These rights are determined by a copyright transfer, where authors retain scholarly rights to post and use their articles.

For open access articles: These rights are determined by an exclusive license agreement, which applies to all our open access content.

In both cases, the fundamental rights needed to publish and distribute an article remain the same and Elsevier authors will be able to use their articles for a wide range of scholarly purposes.

Details on how authors can reuse and post their own articles are provided below.

Help and support
For reuse and posting not detailed below, please see our posting policy, or for authors who would like to:

- Include material from other sources in your work being published by Elsevier, please visit: Permission seeking guidelines for Elsevier authors.
- Obtain permission to re-use material from Elsevier books, journals, databases, or other products, please visit: Obtaining permission to reuse Elsevier material
- Or if you are an Elsevier author and are contacted by a requestor who wishes to re-use all or part of your article or chapter, please also refer them to our Obtaining Permission to Re-Use Elsevier Material page.
- See our FAQ on posting and copyright queries.
- Contact us directly, please email our Permissions Help Desk.

Author Use | Author Posting | Definitions

How authors can use their own journal articles

Authors can use their articles for a wide range of scholarly, non-commercial purposes as outlined below. These rights apply for all Elsevier authors who publish their article as either a subscription article or an open access article.

We require that all Elsevier authors always include a full acknowledgement and, if appropriate, a link to the final published version hosted on Science Direct.

For open access articles these rights are separate from how readers can reuse your article as defined by the author's choice of Creative Commons user license options.

Authors can use either their accepted author manuscript or final published article for:	
✓	Use at a conference, meeting or for teaching purposes
✓	Internal training by their company
✓	Sharing individual articles with colleagues for their research use* (also known as "scholarly sharing")
✓	Use in a subsequent compilation of the author's works
✓	Inclusion in a thesis or dissertation
✓	Reuse of portions or extracts from the article in other works
✓	Preparation of derivative works (other than for commercial purposes)

Vita

Ammar Qureshi was born in Karachi, Pakistan in May, 1986. His father works in Jeddah, Saudi Arabia so he moved there with his family and lived in Jeddah till the age of eighteen. At the age of six he went to an Islamic School to memorize the Holy Qura'n and started elementary school at the age of nine. He graduated from Hala International School in May, 2004 with an Ordinary Level (O-Levels) degree and from Al-Wadi International School with an Advanced Level (A-Levels) degree, both credited by the University of Cambridge, London. He accepted an Honor Merit Scholarship at Louisiana State University in 2005 for his bachelor's degree which he completed in May 2008 while majoring in bioengineering. In May 2010, Ammar graduated with MSc in Bioengineering from LSU under Dr Daniel Hayes and his thesis was titled " Biocompatible/ Bioresorbable polymer based silver nanomaterial coating for chronic indwelling medical devices and bioscaffolds for tissue regrowth". Ammar accepted a Research Associate position at LSU AgCenter in Dr Hayes' lab in 2010 and is also currently pursuing a doctor's degree in bioengineering under Dr. Daniel Hayes which he will complete by December 2013.